

4

RADC-TR-88-199  
Final Technical Report  
April 1989



AD-A215 034 **REACTIVE ATMOSPHERE  
PROCESSING OF  $\text{BaTiO}_3$  AND  
ORIGINS OF ITS PHOTOREFRACTIVE  
EFFECT**

Hughes Research Laboratories

M. B. Klein and B. A. Wechsler

APPROVED FOR PUBLIC RELEASE; DISTRIBUTION UNLIMITED.

ROME AIR DEVELOPMENT CENTER  
Air Force Systems Command  
Griffiss Air Force Base, NY 13441-5700

DTIC  
ELECTE  
NOV 24 1989  
S B D  
CO

89 11 11 153

This report has been reviewed by the RADC Public Affairs Division (PA) and is releasable to the National Technical Information Service (NTIS). At NTIS it will be releasable to the general public, including foreign nations.

RADC-TR-88-199 has been reviewed and is approved for publication.

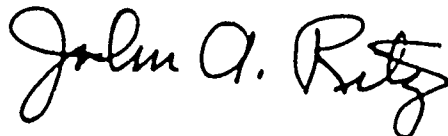
APPROVED: 

CHARLES L. WOODS  
Project Engineer

APPROVED: 

HAROLD ROTH  
Director of Solid State Sciences

FOR THE COMMANDER:



JOHN A. RITZ  
Directorate of Plans & Programs

If your address has changed or if you wish to be removed from the RADC mailing list, or if the addressee is no longer employed by your organization, please notify RADC (ESOP) Hanscom AFB MA 01731-5000. This will assist us in maintaining a current mailing list.

Do not return copies of this report unless contractual obligations or notice on a specific document requires that it be returned.

UNCLASSIFIED  
SECURITY CLASSIFICATION OF THIS PAGE

REPORT DOCUMENTATION PAGE				Form Approved OMB No 0704-0188	
1a REPORT SECURITY CLASSIFICATION UNCLASSIFIED			1b RESTRICTIVE MARKINGS N/A		
2a SECURITY CLASSIFICATION AUTHORITY N/A			3 DISTRIBUTION/AVAILABILITY OF REPORT Approved for public release; distribution unlimited.		
2b DECLASSIFICATION/DOWNGRADING SCHEDULE N/A					
4. PERFORMING ORGANIZATION REPORT NUMBER(S) N/A			5. MONITORING ORGANIZATION REPORT NUMBER(S) RADC-TR-36-199		
6a. NAME OF PERFORMING ORGANIZATION Hughes Research Laboratories		6b OFFICE SYMBOL (if applicable)	7a NAME OF MONITORING ORGANIZATION Rome Air Development Center (ESOP)		
6c ADDRESS (City, State, and ZIP Code) 3011 Malibu Canyon Road Malibu CA 90265			7b ADDRESS (City, State, and ZIP Code) Hanscom AFB MA 01731-5000		
8a NAME OF FUNDING/SPONSORING ORGANIZATION Rome Air Development Center		8b OFFICE SYMBOL (if applicable) ESOP	9 PROCUREMENT INSTRUMENT IDENTIFICATION NUMBER F19628-84-C-0069		
8c ADDRESS (City, State, and ZIP Code) Hanscom AFB MA 01731-5000			10 SOURCE OF FUNDING NUMBERS		
			PROGRAM ELEMENT NO 61101E	PROJECT NO D800	TASK NO AR
			WORK UNIT ACCESSION NO 20		
11 TITLE (Include Security Classification) REA . ATMOSPHERE PROCESSING OF BaTiO <sub>3</sub> AND ORIGINS OF ITS PHOTOREFRACTIVE EFFECT					
12. PERSONAL AUTHOR(S) M. B. Klein and B. A. Wechsler					
13a. TYPE OF REPORT Final		13b. TIME COVERED FROM Dec 83 to Jul 85		14. DATE OF REPORT (Year, Month, Day) April 1989	
				15. PAGE COUNT 114	
16. SUPPLEMENTARY NOTATION N/A					
17 COSATI CODES			18 SUBJECT TERMS (Continue on reverse if necessary and identify by block number)		
FIELD	GROUP	SUB-GROUP			
17	02		Photorefractive;		
20	06		Barium Titanate (B-T. 2);		
			Phase Diagram;		
19 ABSTRACT (Continue on reverse if necessary and identify by block number)					
<p>Photorefractive materials offer great promise for applications in optical data processing and phase conjugation using degenerate four-wave mixing. BaTiO<sub>3</sub> is a particularly promising material, primarily because the very large value of the electro-optic tensor component r<sub>42</sub> yields correspondingly large values of grating efficiency, beam coupling gain, and four-wave mixing reflectivity. Unfortunately, the commercial availability of BaTiO<sub>3</sub> crystals is limited, and samples which are available are relatively small and impure and have not been characterized or optimized for photorefractive applications. In the program reviewed here, we have addressed two of the most important problems in the development and use of photorefractive BaTiO<sub>3</sub>: stabilization of the cubic phase in order to permit more rapid crystal growth than is now possible, and determination and characterization of the photorefractive species in commercial BaTiO<sub>3</sub>.</p> <p>The development of a rapid crystal growth technique hinges on the elimination of the</p>					
20 DISTRIBUTION/AVAILABILITY OF ABSTRACT <input checked="" type="checkbox"/> UNCLASSIFIED/UNLIMITED <input type="checkbox"/> SAME AS RPT <input type="checkbox"/> DTIC USERS			21 ABSTRACT SECURITY CLASSIFICATION UNCLASSIFIED		
22a NAME OF RESPONSIBLE INDIVIDUAL Charles L. Woods			22b. TELEPHONE (Include Area Code) (617) 377-4922		22c OFFICE SYMBOL RADC (ESOP)

UNCLASSIFIED

high-temperature hexagonal phase of  $\text{BaTiO}_3$ . It has been our belief that this is an impurity-stabilized phase and could be eliminated by proper treatment of the starting materials. Reactive atmosphere processing (RAP) was used to treat a variety of  $\text{BaTiO}_3$  powders, and the effect of such treatment was monitored by quenching these powders from temperatures near the melting point. In several experiments, the cubic phase was obtained in powders created in an  $\text{O}_2/\text{CO}_2/\text{Br}_2$  atmosphere. However, such results were not always reproducible and may have been significantly affected by kinetic factors. Although such an approach to stabilizing the cubic phase remains unproven, the development of compatible RAP formulas should prove useful for control of impurities during crystal growth.

The second major effort of this program was the identification and characterization of the photorefractive species in  $\text{BaTiO}_3$ . Using the results of a number of experiments, we have concluded that iron (in the forms  $\text{Fe}^{2+}$  and  $\text{Fe}^{3+}$ ) is the dominant photorefractive species in commercial  $\text{BaTiO}_3$ . We have been able to measure the densities of  $\text{Fe}^{2+}$  and  $\text{Fe}^{3+}$ , along with the sign of the photocarriers, the effective electro-optic coefficient, and a lumped parameter taking into account the transport properties of holes and electrons. On the basis of our results, we have made recommendations for optimizing the doping and heat treatment of  $\text{BaTiO}_3$  for photorefractive applications.

(x.7) —

Item 17. COSATI CODES (Continued).

<u>Field</u>	<u>Group</u>
20	12

Accession For	
NTIS GRA&I	<input checked="checked" type="checkbox"/>
DTIC TAB	<input type="checkbox"/>
Unannounced	<input type="checkbox"/>
Justification	
By	
Distribution/	
Availability Codes	
Dist	Avail and/or Special
A-1	

UNCLASSIFIED

## TABLE OF CONTENTS

SECTION	PAGE
1 INTRODUCTION.....	1-1
2 REACTIVE ATMOSPHERE PROCESSING OF BARIUM TITANATE POWDERS.....	2-1
A. Introduction.....	2-1
B. Experimental Procedures.....	2-9
C. Results.....	2-20
REFERENCES (SECTION 2).....	2-42
3 ORIGINS OF THE PHOTOREFRACTIVE EFFECT.....	3-1
A. Introduction.....	3-1
B. Experimental.....	3-1
C. General Background and Models.....	3-4
D. Experimental Results.....	3-15
E. Interpretation of Data.....	3-32
F. Conclusions.....	3-41
REFERENCES (SECTION 3).....	3-47
4 CONCLUSIONS AND RECOMMENDATIONS FOR FUTURE WORK.....	4-1
A. Crystal Growth.....	4-1
B. Identification and Characterization of the Photorefractive Species.....	4-2
APPENDICES.....	A-1

## LIST OF ILLUSTRATIONS

FIGURE		PAGE
2-1	Phase diagram of a portion of the system system BaO-TiO <sub>2</sub> (after D.E. Rase and R. Roy, J. Am. Ceram. Soc. <u>38</u> , 102, 1955).....	2-3
2-2	Infrared transmission of a Sanders BaTiO <sub>3</sub> crystal grown by the top-seeded solution growth method.....	2-7
2-3	Experimental setup used for reactive atmosphere processing.....	2-15
2-4	Experimental setup used for RAP quenching experiments.....	2-18
2-5	Comparison of cubic-hexagonal transition temperatures for two BaTiO <sub>3</sub> powders in air.....	2-29
3-1	Energy level model for the photorefractive effect.....	3-5
3-2	Gratings in a photorefractive material.....	3-7
3-3	Relative contribution of electrons and holes to the photoconductivity in LiNbO <sub>3</sub> (from Reference 10).....	3-10
3-4	Spectral variation of the absorption coefficient in the visible for four BaTiO <sub>3</sub> samples.....	3-19
3-5	EPR spectrum observed with the DC magnetic field directed along the [010] axis ( $\vec{B} \parallel \vec{c}$ and in the (100) plane).....	3-25
3-6	Expanded EPR spectrum about the $g \approx 2$ spectral region at the same magnetic field orientation as in Figure 3-5.....	3-26
3-7	Angular dependence of the EPR transitions for Fe <sup>3+</sup> (o) and Cr <sup>3+</sup> ( $\Delta$ ) when $\vec{B}$ is rotated in the (100) plane.....	3-30
3-8	Absorption coefficient, concentration of empty traps and Fe <sup>3+</sup> concentration versus total iron concentration for four samples of BaTiO <sub>3</sub> .....	3-34

FIGURE		PAGE
3-9	Relative contribution of electrons and holes to the photoconductivity in $\text{BaTiO}_3$ , assuming $R=\mu_e/\mu_h=2500$ .....	3-37
3-10	Schematic representation of the energy levels of $M^{n+}O_6^{12-n-}$ clusters in $\text{BaTiO}_3$ : (a) $\text{TiO}_6^{8-}$ , (b) $\text{FeO}_6^{10-}$ ( $\text{Fe}^{2+}$ ), and (c) $\text{FeO}_6^{9-}$ ( $\text{Fe}^{3+}$ ).....	3-39

# LIST OF TABLES

TABLE		PAGE
2-1	Manufacturer's Analysis of JMC BaTiO <sub>3</sub> Powder, Lot No. S93020B.....	2-11
2-2	Manufacturer's Analysis of Ferro-1 BaTiO <sub>3</sub> Powder, Lot No. 79088.....	2-11
2-3	Manufacturer's Analysis of Ferro-2 BaTiO <sub>3</sub> Powder, Lot No. MI-968.....	2-12
2-4	Emission Spectrographic Analyses of "As-Received" Ferro-1 and JMC BaTiO <sub>3</sub> Powders (Burgess Analytical Laboratory).....	2-12
2-5	Elements Sought by Burgess Analytical Laboratory.....	2-21
2-6	Impurities >1 ppm Detected by SIMS Analysis of "As-Received" and RAP-Treated JMC BaTiO <sub>3</sub> Powders, ppm atomic.....	2-24
2-7	Emission Spectrographic Analyses of RAP-Treated BaTiO <sub>3</sub> Powders, Weight % (Burgess Analytical Laboratory).....	2-26
2-8	Emission Spectrographic Analyses of RAP-Treated BaTiO <sub>3</sub> Powders, Weight % (Pacific Spectrochemical Laboratory).....	2-27
2-A1	Reactive Atmosphere Processing Experiments.....	2-35
2-A2	RAP Quenching Experiments.....	2-38
3-1	Beam coupling data for 7 samples of BaTiO <sub>3</sub> .....	3-17
3-2	Absorption coefficient at 4416 Å for $\frac{E}{c}$ .....	3-20
3-3	Transition metal impurities in BaTiO <sub>3</sub> , measured by spark source emission spectroscopy.....	3-22
3-4	Electronic properties of first-row transition metals. For each element, we have indicated the most stable valence state.....	3-23
3-5	Fe <sup>3+</sup> concentration measured by EPR.....	3-28



## SECTION 1

### INTRODUCTION

Photorefractive materials offer great promise for applications in optical data processing and phase conjugation using degenerate four-wave mixing (DFWM).  $\text{BaTiO}_3$  is a particularly promising material, primarily because the very large value of the electro-optic tensor component  $r_{42}$  yields correspondingly large values of grating efficiency, beam coupling gain, and four-wave mixing reflectivity. This allows the realization of a variety of new applications, such as real-time convolution and correlation, edge enhancement, image transmission through fibers, self-pumped phase conjugate mirrors, and phase conjugate resonators.

In spite of the intense interest in the applications of  $\text{BaTiO}_3$ , the commercial availability of samples is limited, samples which are available are relatively small and impure, and have not been characterized or optimized for photorefractive applications. If the photorefractive species can be identified, we can then hope to optimize the performance of this material through proper doping and heat treatment.

In the program reviewed here, we have approached two of the most important problems in the development and use of photorefractive  $\text{BaTiO}_3$ : stabilization of the cubic phase in order to make possible a rapid crystal growth technique, and the determination and characterization of the photorefractive species in commercial  $\text{BaTiO}_3$ .

The technique commonly used at present for the growth of  $\text{BaTiO}_3$  is top-seeded solution growth (TSSG). The main feature of this technique is that excess  $\text{TiO}_2$  is added to the melt in order to lower the growth temperature below the stability range of the high temperature hexagonal phase. The disadvantage of the TSSG technique is that it is incongruent, leading to a slow growth rate, and possible inhomogeneities in the crystal. Our belief has been that the high temperature hexagonal phase is impurity-

stabilized, very probably by  $\text{OH}^-$ , and could be eliminated by proper treatment of the starting materials. This would allow congruent growth from a stoichiometric melt and would lead to significantly increased growth rates. In addition, one could expect to achieve higher yields from such a technique and, because crystal growth would proceed isothermally, the homogeneity should also be improved.

Adopting the approach of reactive atmosphere processing (RAP) to remove impurities, we have evaluated the effects of  $\text{CO}/\text{CO}_2$  and halogen treatments of several  $\text{BaTiO}_3$  powders on the stability relations at high temperature. Some experimental results were suggestive of increased stability of the cubic phase as a result of RAP treatment. However, these results were not always reproducible, and we believe that kinetic effects may have played a significant role in producing the observed behavior. While additional effort could be directed toward resolving the remaining uncertainties, we feel it would be more worthwhile to evaluate other approaches to the growth of optimized crystals. In Section 4, we suggest an approach that has been demonstrated to achieve stabilization of the cubic phase and which is suitable for relatively rapid crystal growth.

The second major effort of our DARPA program was the identification and characterization of the photorefractive species in  $\text{BaTiO}_3$ . Using the results of a number of experiments, we have concluded that iron (in the forms  $\text{Fe}^{2+}$  and  $\text{Fe}^{3+}$ ) is the dominant photorefractive species in commercial  $\text{BaTiO}_3$ . We have been able to measure the densities of  $\text{Fe}^{2+}$  and  $\text{Fe}^{3+}$ , along with the sign of the photocarriers, the effective electro-optic coefficient, and a lumped parameter taking into account the transport properties of holes and electrons. On the basis of our results, we have made recommendations for optimizing the doping and heat treatment of  $\text{BaTiO}_3$  for photorefractive applications.

In Section 2 we review our studies of RAP-treated  $\text{BaTiO}_3$  powders. Section 3 describes our study of the origins of the photorefractive effect in commercial samples of  $\text{BaTiO}_3$ . In

Section 4, we present our conclusions and recommendations for further work. Two papers published during the course of this contract (relating to the origins of the photorefractive effect) are included as appendices. A third paper covering our complete effort has been submitted to the Journal of The Optical Society of America. It is not reproduced here, since it is very similar to the contents of Section 3 of this report.

## SECTION 2

### REACTIVE ATMOSPHERE PROCESSING OF BARIUM TITANATE POWDERS

#### A. INTRODUCTION

##### 1. $\text{BaTiO}_3$ Structure and Phase Relations

Barium titanate occurs in five crystalline forms. With increasing temperature, the stable phases are rhombohedral, orthorhombic, tetragonal, cubic, and hexagonal. It is the tetragonal phase that is stable at room temperature and which is of primary interest for its nonlinear properties. The transformation between the cubic and hexagonal phases is reconstructive in nature, whereas all the other transitions are displacive. Consequently, hexagonal  $\text{BaTiO}_3$  cannot be converted to the cubic form without destroying the optical quality of the crystal. It is therefore necessary when designing a crystal growth technique for this material to avoid the high temperature hexagonal phase that normally crystallizes from the melt at  $\sim 1620^\circ\text{C}$ .

The cubic form of  $\text{BaTiO}_3$  has the perovskite structure. The structure can be viewed as a continuous network of corner-linked  $\text{TiO}_6$  octahedra, with  $\text{Ba}^{2+}$  occupying 12-coordinated sites in the oxide anion framework. The space group is  $\text{Pm}\bar{3}\text{m}$ , which is centrosymmetric and therefore non-polar. The tetragonal form has space group  $\text{P4mm}$ , which is polar. The transition from the cubic structure at  $\sim 130^\circ\text{C}$  involves only a slight distortion, resulting in the  $\text{Ti}^{4+}$  ion occupying an off-center position in the oxygen octahedron. The net effect of this distortion is to produce a spontaneous electric polarization, with the polarization directed along the cubic  $\langle 100 \rangle$  axes. Further transitions, to the orthorhombic phase below  $5^\circ\text{C}$  and the rhombohedral phase below  $-90^\circ\text{C}$ , similarly involve distortions directed along the cubic  $\langle 110 \rangle$  and  $\langle 111 \rangle$  axes, respectively.

The hexagonal phase, which occurs above  $\sim 1450^\circ\text{C}$ , has a significantly different structure.<sup>1</sup> The cubic-hexagonal transition involves both a rearrangement of the barium-oxygen close-packed layers and a reordering of the  $\text{TiO}_6$  octahedra. In the hexagonal structure, two-thirds of the  $\text{TiO}_6$  octahedra form face-sharing pairs, or  $\text{Ti}_2\text{O}_9$  groups. These are corner-linked to the remaining  $\text{TiO}_6$  groups. Thus, a major rearrangement occurs at the transition and it is consequently quite sluggish compared with the spontaneous distortions that characterize the lower temperature transitions. For this reason, it is possible to quench the hexagonal phase to room temperature by cooling relatively quickly from above the cubic-hexagonal transition temperature.

The phase diagram of the system  $\text{BaO-TiO}_2$  was studied by Rase and Roy<sup>2</sup> and is shown in Figure 2-1. The field of hexagonal  $\text{BaTiO}_3$  is seen to exist between 1450 and  $1618^\circ\text{C}$ . With increasing  $\text{TiO}_2$  content, the phase boundary between cubic and hexagonal  $\text{BaTiO}_3$  rises to higher temperatures. It should be noted that these relationships are based on a small number of data and are at least somewhat schematic. Later studies of this system<sup>3-5</sup> have revised the subsolidus relationships but no subsequent studies have revised the liquidus relations.

## 2. Impurity Effects on the Cubic-Hexagonal Transition

A number of previous studies have addressed the question of the effects of various impurities (primarily cationic impurities) on the temperature of the cubic-hexagonal transition. The fact that no other simple 2-4 perovskites are known to occur with the hexagonal structure<sup>6</sup> implies that solid solutions between  $\text{BaTiO}_3$  and these other phases will result in increased stability for the cubic phase. In fact, studies of solutions involving isovalent substitutions for Ba<sup>7,8</sup> show a rapid rise of the cubic-hexagonal transition temperature with doping levels on the order of 0.1 to 1 mol%. Other studies, involving for example<sup>9</sup> the system  $\text{BaTiO}_3\text{-SiO}_2$ , also indicate stabilization of the cubic phase, although

Permission has been granted by R. Roy at The Pennsylvania State University to publish Figure 2-1.

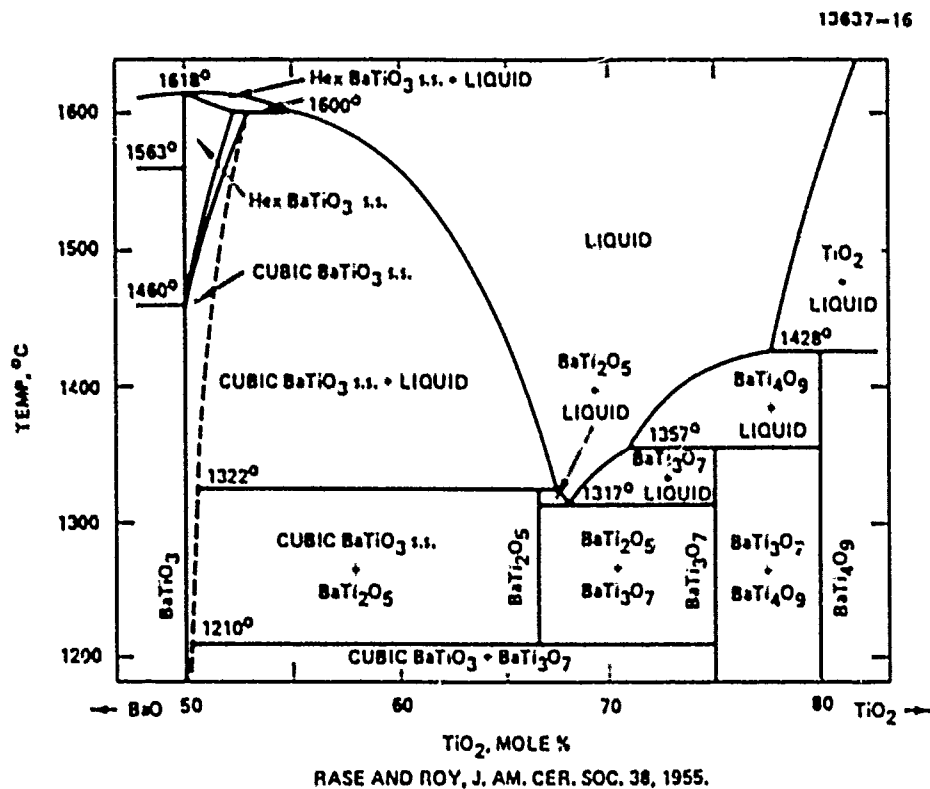


Figure 2-1. Phase diagram of a portion of the system system  $\text{BaO-TiO}_2$  (after D.E. Rase and R. Roy, J. Am. Ceram. Soc. 38, 102, 1955).

here the solution is not a simple isostructural substitution, but may involve the incorporation of some cation deficiency or oxygen excess.

On the other hand, a number of compounds have been reported with the hexagonal  $\text{BaTiO}_3$  structure. Dickinson et al.<sup>10</sup> prepared a series of compounds in which various amounts of primarily trivalent metals ( $\text{Ti}^{3+}$ , V, Cr, Mn, Fe, Co, Ru, Rh, Ir, Pt) were substituted in large amounts for  $\text{Ti}^{4+}$ . Each of these formed, within at least a certain range of metal concentration, with the hexagonal structure. These authors suggested that the hexagonal structure was favored by compounds in which metal-metal bonding occurs between octahedral cations. The face-sharing octahedral pairs found in the hexagonal structure should be an unfavorable arrangement energetically unless there is an attractive interaction between the metal ions in adjacent octahedra.

Dickinson et al. were able to prepare at  $1100^\circ\text{C}$ , from already reduced starting materials, a hexagonal powder with the approximate formula  $\text{BaTi}_{0.48}^{3+}\text{Ti}_{0.52}^{4+}\text{O}_{2.76}$ . This suggests that the presence of reduced titanium and/or oxygen deficiency may lower the cubic-hexagonal transition temperature. A similar observation was made by Arend and Kihlberg<sup>11</sup> who found that reduction of  $\text{BaTiO}_3$  with  $\text{H}_2$  at  $1325^\circ\text{C}$  brought about a transformation to the hexagonal phase with a relatively small oxygen deficiency ( $\text{BaTiO}_{2.993}$ ). No mention was made of the  $\text{Ti}^{3+}$  content in the latter study or of the possible formation of  $\text{OH}^-$  defects.

Error et al.<sup>12</sup> reported stabilization of hexagonal  $\text{BaTiO}_3$  at temperatures below  $700^\circ\text{C}$  in material prepared by a low-temperature liquid mix technique. This effect was ascribed to the very fine particle size (a few hundred Å) of the material. However, the presence of dissolved carbonate ions with this method may also have been a contributing factor. Adsorption of carbonate ions was observed on the surface of the hexagonal  $\text{BaTiO}_3$  particles. Use of an alkali carbonate flux has also been observed<sup>13</sup> to result in the growth of hexagonal  $\text{BaTiO}_3$  crystals

at temperatures below 1200°C, although the identity of the impurity stabilizing the hexagonal phase in this case is not clear.

The observations noted above suggest that the cubic-hexagonal transition temperature is sensitive to the nature of the impurities present in the material. This implies that the phase transition itself is not necessarily an intrinsic property of BaTiO<sub>3</sub> but may, in fact, depend upon the presence of certain impurities. Such behavior can be called an "impurity-conditioned" phase transition. An example of similar behavior in another system is that of the rare-earth trifluorides.<sup>14</sup> In these materials, a high temperature phase transition from hexagonal to orthorhombic was observed upon cooling below the melting point. The reported transition temperatures varied significantly among various samples. When crystals were grown in an atmosphere (HF) designed to exclude OH<sup>-</sup> from the crystal, however, it was shown that the high temperature phase transition disappeared entirely, and the low-temperature orthorhombic phase was obtained upon cooling through the melting point.

Such results indicate that it is sometimes possible to eliminate the stability field for an impurity-stabilized phase by exacting control of the impurity or impurities responsible for its stabilization. An approach that has been shown<sup>15-17</sup> to be successful for such control, particularly for the elimination of anion impurities such as OH<sup>-</sup>, is that of reactive atmosphere processing (RAP). In this approach, an atmosphere is chosen to actively displace species such as OH<sup>-</sup> from the solid and to prevent water present in the furnace environment during crystal growth from reacting with and entering the solid. At the same time, the formation of volatile molecules can help to remove cationic impurities from the solid as well.

Our approach to eliminate the hexagonal phase stability in BaTiO<sub>3</sub>, therefore, was to examine ways to treat BaTiO<sub>3</sub> powders in various atmospheres and to determine the effects of such treatments on the presence or absence of hexagonal BaTiO<sub>3</sub>. The



details of these experiments will be presented in the following sections.

### 3. Principles of Reactive Atmosphere Processing

Water is a ubiquitous impurity in materials processing, deriving from the laboratory atmosphere and/or from furnace ceramics, other process equipment, or the starting materials. As the infrared spectrum in Figure 2-2 shows, the hydroxide ion ( $\text{OH}^-$ ) is present in substantial quantities (probably on the order of 1000 ppm) in an as-grown  $\text{BaTiO}_3$  crystal purchased from Sanders Associates. In addition to its possible impact on the cubic-hexagonal transition, such impurities may impose a variety of other deleterious mechanical and physicochemical effects on crystals in which it is present. Thus, techniques to eliminate hydroxide impurities are desirable regardless of the effect on the stability of the hexagonal phase.

The reactive atmosphere process (RAP) developed at Hughes Research Laboratories has been used to achieve high levels of purification in a variety of halide and oxide systems. Control of impurities is achieved by chemical manipulation of the solid through the coexisting liquid and/or vapor phases. In the RAP technique, the sample is heated in an atmosphere containing atoms or molecules that have an affinity for reaction with impurity ions. The impurities are removed through two mechanisms:

- (1) migration of the species through the sample to the surface, where they react with the RAP molecule and are pumped away; or
- (2) migration of small molecules or atoms (formed thermally from the RAP molecule) into the sample, where they react with impurity ions to form volatile compounds, which then migrate to the surface and are pumped away. The reactive species needed to achieve such effects are easily generated by pyrolysis during heating of the sample and its surrounding atmosphere.

Water is typically incorporated into an oxide crystal by means of the following reaction:

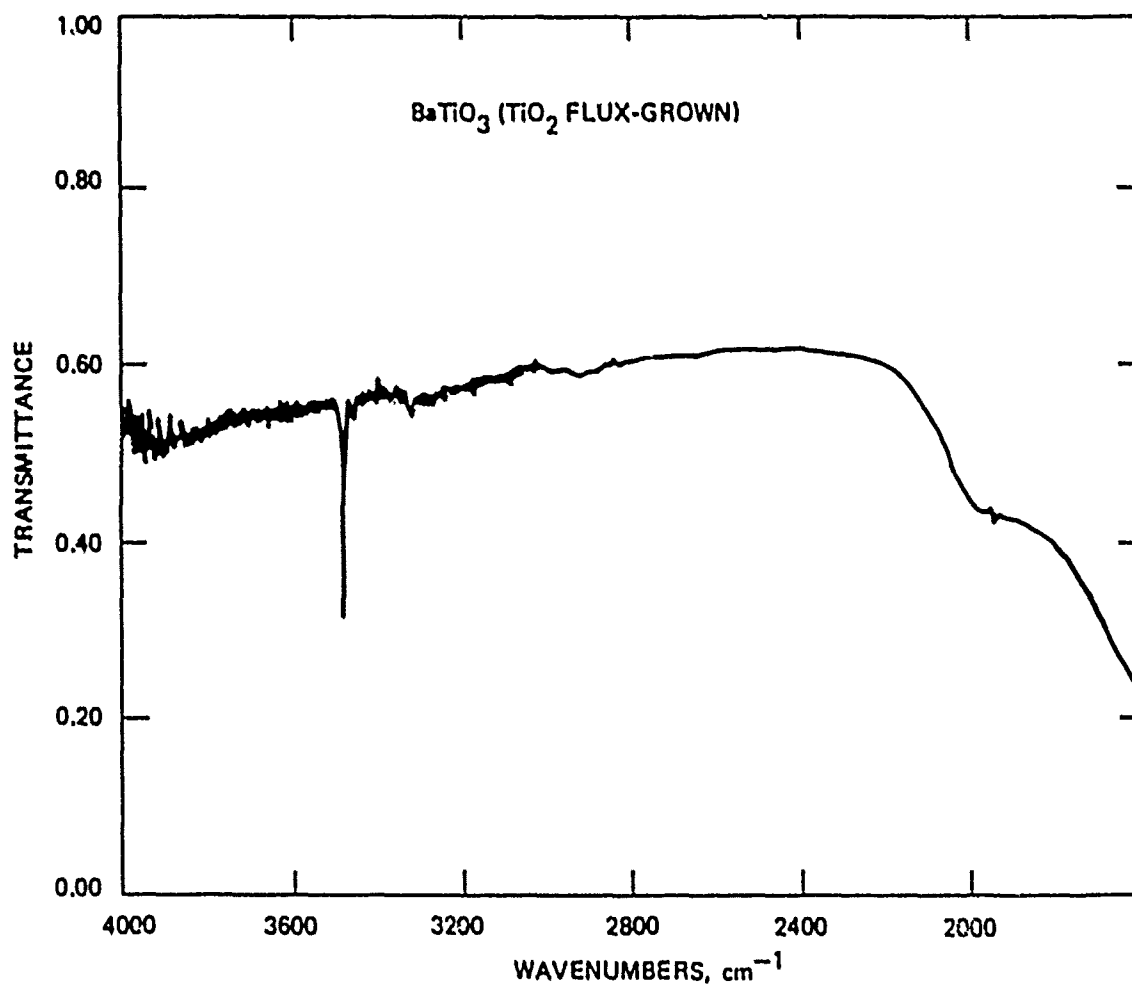
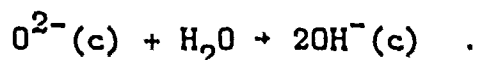
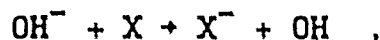


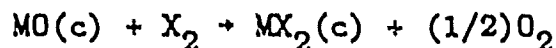
Figure 2-2. Infrared transmission of a Sanders BaTiO<sub>3</sub> crystal grown by the top-seeded solution growth method. Absorption peak at 3485 cm<sup>-1</sup> (2.869 μm) is due to O-H stretching vibration.



Because of the high proton affinity of  $O^{2-}$ , the only viable mechanism for removing  $OH^-$  must involve an electron-transfer reaction with a more electronegative species, typically a halogen:

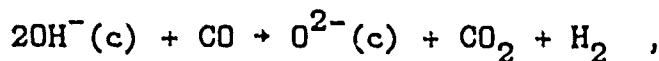


where  $X = F, Cl, Br, \text{ or } I$ . However, the objective is to remove  $OH^-$  without causing any conversion of the oxide to the halide. Thus, for the reaction

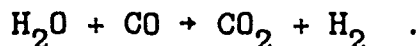


the conditions must be chosen so as to favor the left-hand side of the equation. This is achieved by providing a sufficient oxygen pressure to prevent any significant displacement of the equilibrium toward the right. The tendency for this reaction to proceed is also a strong function of the electronegativity difference between the metal and halogen species. This constrains the selection of halogens for use with any particular metal oxide and, in the case of  $BaTiO_3$ , would be expected to limit the choice to either  $Br_2$  or  $I_2$ .

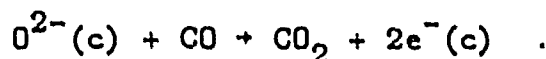
An alternative approach to the removal of  $OH^-$  from the crystalline phase involves the use of a  $CO/CO_2$  gas mixture. In this approach, carbon monoxide may scavenge hydroxide via the reaction:



and may also remove water from the process atmosphere:

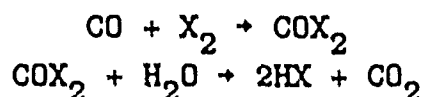


Carbon monoxide is a strongly reducing gas and, if present in sufficient concentration, will result in oxygen loss from the crystal:



In  $BaTiO_3$ , the electrons thus released may form color centers or result in the reduction of  $Ti^{4+}$  to  $Ti^{3+}$ . Since  $Ti^{3+}$  is suspected of stabilizing the hexagonal  $BaTiO_3$  structure, it is desirable to avoid such effects. Therefore, the  $CO/CO_2$  ratio must be kept low enough to ensure that the crystal is not significantly reduced.

An additional mechanism may become operative when the halogen and  $CO/CO_2$  gases are combined. The following equations:



indicate a means by which water in the process environment may be tied up and thereby prevented from entering the solid phase. Such an effect is particularly important when the halogen is restricted to  $Br_2$  or  $I_2$  because, unlike  $F_2$  or  $Cl_2$ , these species alone are not effective for gettering water through the reaction:



## B. EXPERIMENTAL PROCEDURES

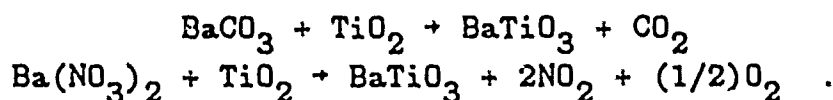
### 1. Starting Materials

Four  $BaTiO_3$  samples were obtained from three different suppliers. The highest purity material, at least in terms of cation impurities, was Johnson-Matthey (JMC) Puratronic Grade (nominally 99.995%, metals basis). Several different lots were used during the course of the study. However, all samples for which chemical analyses are presented (see below) were obtained

from lot no. S93020B. The manufacturer's analysis of this lot is presented in Table 2-1. Analyses of the other lots used indicated Si at levels of 1 to 3 ppm, with Fe, Mg, Ca, Cu, and Al at or below 1 ppm. A second sample was obtained from Alfa Products (catalogue no. 88267, lot no. 022483) and was nominally 99.9% pure (metals basis). No analysis was provided by the manufacturer. Two samples were obtained from Transelco Division of Ferro Corporation. The first, Ferro-1 (catalogue no. 219-2, lot no. 79088) was nominally 99.5% pure and the second, Ferro-2 (catalogue no. TRS-850, lot no. MI-968) was somewhat higher purity,  $\geq 99.9\%$ . The manufacturer's analyses are given in Tables 2-2 and 2-3.

Samples of the Ferro-1 and JMC powders "as received" were analyzed by semiquantitative emission spectrographic techniques (see below for details of analytical methods). The results, shown in Table 2-4, are in general qualitative agreement with the manufacturer's analyses. A SIMS analysis of JMC powder was also obtained and will be discussed below.

In addition to the commercial powders, some experiments involved synthesis of  $\text{BaTiO}_3$  from various starting materials. Three different techniques were investigated. The first two involve solid state synthesis based on the following reactions:



Johnson Matthey Puratronic Grade starting materials were used for these syntheses. Mixes of the appropriate stoichiometry were prepared and were ground manually in a diamonite mortar under acetone or methanol. After drying, the carbonate mix was loaded into a platinum crucible and reacted at 1000 to 1200°C for 24 to 48 hours. The product was then ground and reacted again at 1000 to 1500°C. X-ray powder diffraction patterns indicated complete reaction. The nitrate mix was reacted at a temperature of about 650 to 700°C. Although initial experiments using less pure

Table 2-1. Manufacturer's Analysis of JMC  
BaTiO<sub>3</sub> Powder, Lot No. S93020B

Element	Concentration (ppm by weight)
Mg	<1
Si	20
Ca	<1
Fe	<1

Table 2-2. Manufacturer's Analysis of Ferro-1  
BaTiO<sub>3</sub> Powder, Lot No. 79088

Element (as oxide)	Concentration (weight %)	Element (as oxide)	Concentration (weight %)
Al <sub>2</sub> O <sub>3</sub>	.02	Nb <sub>2</sub> O <sub>5</sub>	<.01
CaO	.07	P <sub>2</sub> O <sub>5</sub>	<.005
CuO	<.01	SiO <sub>2</sub>	.02
Fe <sub>2</sub> O <sub>3</sub>	.006	SO <sub>3</sub>	<.005
K <sub>2</sub> O	.02	SrO	.02
MnO	<.01	V <sub>2</sub> O <sub>5</sub>	<.01
Na <sub>2</sub> O	<.01	ZrO <sub>2</sub>	.01

Table 2-3. Manufacturer's Analysis of Ferro-2  
BaTiO<sub>3</sub> Powder, Lot No. MI-968

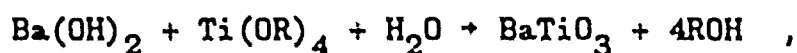
Element (as oxide)	Concentration (weight %)	Element (as oxide)	Concentration (weight %)
Na <sub>2</sub> O	.004	Fe <sub>2</sub> O <sub>3</sub>	.001
K <sub>2</sub> O	.001	Al <sub>2</sub> O <sub>3</sub>	.002
CaO	<.001	Nb <sub>2</sub> O <sub>5</sub>	<.01
MgO	<.001	SiO <sub>2</sub>	<.001
SrO	<.005	ZrO <sub>2</sub>	<.001
SO <sub>3</sub>	.01	P <sub>2</sub> O <sub>5</sub>	.005

Table 2-4. Emission Spectrographic Analyses of  
"As-Received" Ferro-1 and JMC BaTiO<sub>3</sub> Powders  
(Burgess Analytical Laboratory)

Element	Concentration (weight %)	
	Ferro-1	JMC
Si	.05-.5	.005-.05
Ca	.005-.05	.005-.05
Mn	<0.005	
Fe	<0.005	<0.005
Cu	<0.005	<0.005
Zr	.005-.05	
Blank indicates element not detected.		

starting materials were successful in producing  $\text{BaTiO}_3$ , later experiments typically produced a molten phase, presumably  $\text{Ba}(\text{NO}_3)_2$ , and the  $\text{BaTiO}_3$  formation reaction did not proceed to completion.

The third synthesis method utilized a low-temperature aqueous process for formation of  $\text{BaTiO}_3$ . Such an approach has certain potential advantages over the standard solid-state reactions with respect to the purity, stoichiometry, and atomic-scale homogeneity attainable. The starting materials were barium hydroxide and tetrabutyl titanate. These were combined with an excess of water and were then reacted at  $120^\circ\text{C}$  under 2 atm of steam in an ordinary pressure cooker. The reaction can be expressed by the following reaction:



where  $\text{R} = (\text{CH}_2)_3\text{CH}_3$ . Following neutralization with  $\text{HCl}$  and overnight dialysis, the solid residue was examined by x-ray diffraction and was confirmed to be tetragonal  $\text{BaTiO}_3$ . However, upon heating this material to  $1300^\circ\text{C}$  or above it was found that partial melting occurred. X-ray examination of the products showed the presence of phases other than  $\text{BaTiO}_3$ . Thus, it appears that this preparation actually retained an excess of  $\text{TiO}_2$ . Presumably, this was in some amorphous phase in the low-temperature product and was therefore not seen in the x-ray patterns. While this problem could be overcome by further refinements to the procedure, this method was not used for any further experiments on this program.

## 2. RAP Experiments

RAP experiments were performed in two basic configurations: (1) large volume powder samples (up to ~20 grams) were processed in a horizontal tube furnace and cooled slowly from the process temperature; and (2) small samples (~200 mg) were processed in a vertical tube furnace and were quenched rapidly from the process



temperature. Details of the latter series of experiments will be presented in the next section. However, the generation of the RAP atmospheres was essentially identical in both cases and will be described fully here.

For the horizontal processing runs, two different furnaces were used. Early experiments (up to RBT 34) were carried out in a SiC-heated furnace with a maximum temperature of 1500°C. Later experiments utilized a Kanthal wire-wound furnace with a maximum temperature of 1100°C. In both cases, the samples were processed within an alumina tube, closed on one end and with a sealed glass cap on the other end holding inlet and outlet gas tubes. The experimental setup is depicted in Figure 2-3.

Samples were held in Pt foil-lined alumina boats. The powders were loosely loaded into the foil and placed into the furnace at room temperature. Usually, two boats with different powders were placed end-to-end in the furnace tube and run simultaneously. The tube was purged with the desired process atmosphere before bringing the furnace up to temperature. Samples were generally held at temperature for 18 to 48 hours before furnace power was interrupted and the samples were allowed to cool naturally within the furnace to room temperature. The process atmosphere was maintained until the samples reached room temperature except that in the case of  $I_2$  treatments, the  $I_2$  source was shut off when furnace temperature was ~60 to 90°C in order to avoid precipitation of iodine within the furnace tube.

Iodine was added to the process atmosphere by passing the desired gas mixture through a flask containing iodine crystals. The concentration was controlled by adjusting the temperature of the iodine-containing flask. This was accomplished by use of a heat lamp in early runs, but later the temperature was controlled by means of a hot water bath in which the flask was immersed. With the temperature set at 60°C, the vapor pressure of  $I_2$  was ~5 mm of Hg, or 0.0066 atm. Tubing leading from the  $I_2$  source to the furnace and from the furnace to the trap was wrapped with heating tape to prevent clogging. Iodine was trapped out after

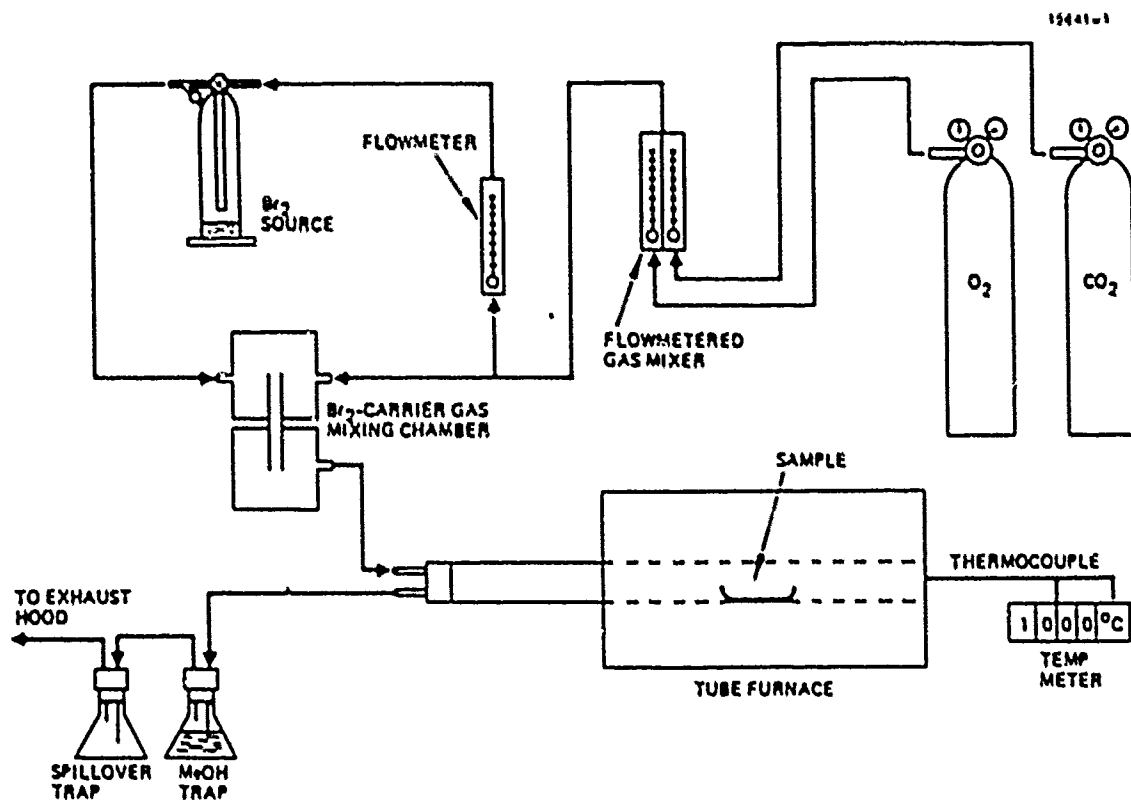


Figure 2-3. Experimental setup used for reactive atmosphere processing.

exiting the sample chamber by passing the gas through a glass cylinder at room temperature. Residual iodine which did not precipitate out in this cylinder was dissolved in a methanol trap.

The source of bromine vapor was a flask containing liquid bromine held at room temperature. A small portion of the gas mixture was passed through this flask and then entered into a gas mixer where the  $\text{Br}_2$  was further diluted with the pure gas mixture. The  $\text{Br}_2$  pressure was thereby maintained at 0.0066 atm, the same pressure as was used for iodine treatments. Bromine was removed from the exhaust gas by a methanol trap. The gas flow rate was  $\sim 1 \text{ cm}^3 \text{ sec}^{-1}$  for all experiments, at a total pressure of 1 atm.

In early experiments, carbon monoxide was generated by passing a stream of  $\text{CO}_2$  through a flask containing graphite chips at a temperature of 900 to 1000°C. However, the majority of experiments utilized a cylinder of CO as the source. The CO cylinder used had a purity greater than 99.3%, and the  $\text{CO}_2$  was at least 99.99% pure. For some experiments, nitrogen, oxygen, and argon were utilized. These were obtained from the laboratory house supply and had purities of  $\sim 99.998\%$ , 99.6%, and 99.0%, respectively. Tubing used throughout the gas system was either polyethylene or teflon.

### 3. Quenching Experiments

The determination of the phase boundary between the cubic and hexagonal forms of  $\text{BaTiO}_3$  is complicated by the kinetics of the phase transition itself. Due to the reconstructive nature of the transition, the change is relatively slow. For this reason, differential thermal analysis is not appropriate to observe the transition. On the other hand, samples cooled slowly from the hexagonal field through the phase transition may have time enough to convert back to cubic, making identification of the hexagonal phase stability difficult. The approach adopted in this study was to quench the samples rapidly from the process temperature to

a temperature low enough that no reconversion is possible. One can therefore take advantage of the slow kinetics to preserve the high temperature phase for analysis at room temperature, thereby allowing one to infer the actual high temperature stability relations.

The apparatus used for these experiments is shown schematically in Figure 2-4. A  $\text{MoSi}_2$ -heated furnace with a maximum temperature capability of  $1700^\circ\text{C}$  was fitted with a vertical  $\text{Al}_2\text{O}_3$  tube. The ends of the tube were sealed with viton gaskets to the end caps which hold gas inlet/outlet, sample holder, and sample retrieval ports. The sample ( $\sim 100$ - $200$  mg) was contained in a capsule made from thin Pt foil. The capsule was held by a  $0.004$ " Pt wire whose ends were wrapped around two heavier Pt wires that extended out of the furnace. A type B (Pt 6%Rh versus Pt 30%Rh) thermocouple was placed within  $1$  cm of the sample capsule. In most experiments, the sample was lowered into the furnace at a temperature near  $1200^\circ\text{C}$  and was then ramped to the process temperature in 2 to 5 hours. Sometimes, the sample was lowered quickly into the furnace at the desired temperature. The gas system was the same as that described above for RAP processing and the flow rate of  $1 \text{ cm}^3 \text{ sec}^{-1}$  was maintained for all experiments, with a total gas pressure of  $1$  atm.

Following the completion of the desired process, the sample was quenched in the following manner. An electrical current was passed through the Pt wire sample holder assembly. This resulted in melting of the thin Pt wire holding the sample capsule, causing the capsule to drop to the bottom of the furnace. The temperature at the bottom was near  $100^\circ\text{C}$ , and samples could be removed by unscrewing the teflon plug sealing the bottom end cap. In most cases, two different samples were run simultaneously by suspending two sample capsules next to one another. The recovered samples were analyzed by x-ray diffraction to determine the phase composition.

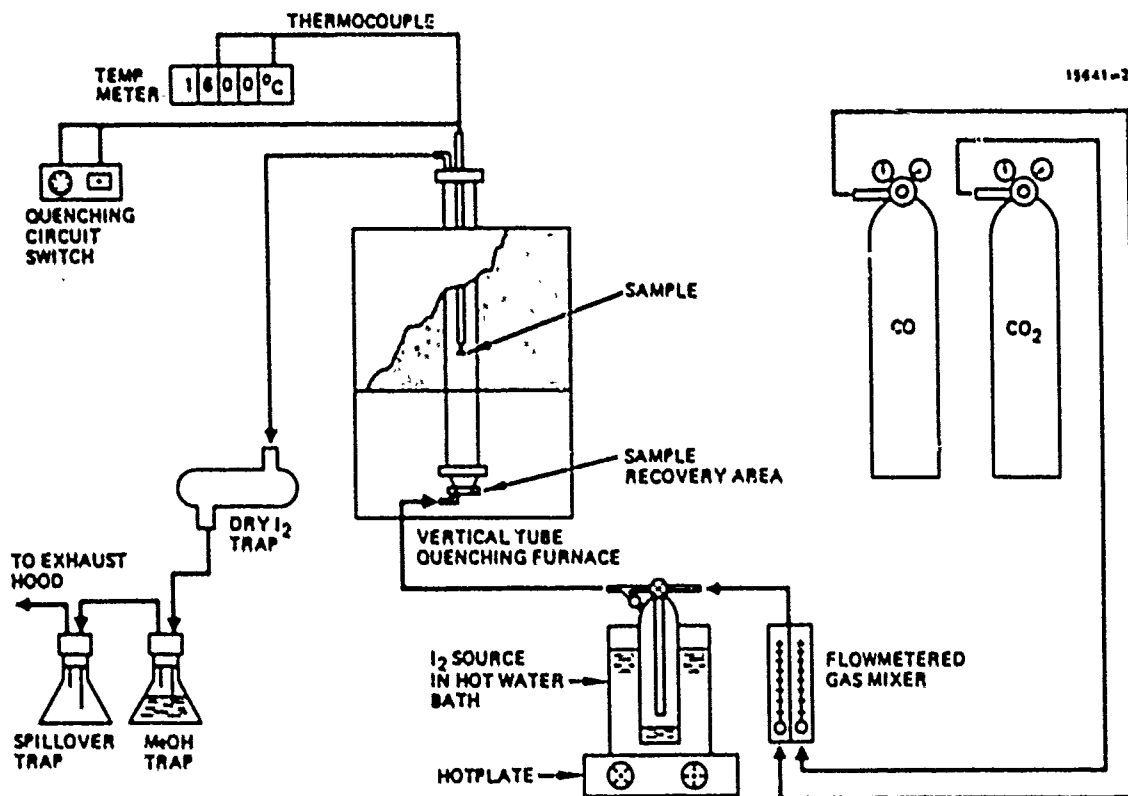


Figure 2-4. Experimental setup used for RAP quenching experiments.

#### 4. Sample Characterization Methods

All RAP-treated samples were studied by differential scanning calorimetry (DSC) to measure the temperature of the tetragonal-cubic transition. Although not directly related to the cubic-hexagonal transition, this method is nevertheless useful for characterizing the differences between various samples and for monitoring changes caused by chemical and/or annealing treatments. The instrument used was a DuPont 1090 Thermal Analyzer. Samples of ~20 to 50 mg were sealed in aluminum cups and heated from 70 to 150°C at a rate of 10° min<sup>-1</sup>. The values reported in Table 2-A1 are the peak temperatures, which are generally 3 to 4 degrees higher than the onset of the transition and were obtained by visual inspection of the charts. Precision of this method is on the order of ±1°C.

All samples were studied by powder x-ray diffraction methods to provide phase identification. X-ray patterns were obtained using an automated vertical Philips diffractometer with a Cu K $\alpha$  x-ray source. Most scans covered the range of 20 to 42° two-theta, which was sufficient to determine whether the BaTiO<sub>3</sub> was present in tetragonal or hexagonal forms (or a mixture of both). When phases other than BaTiO<sub>3</sub> were found to be present, more extensive scans were made to assist in the identification. It should be noted that, due to the spontaneous transition between the cubic and tetragonal phases of BaTiO<sub>3</sub> near 130°C, the appearance of the tetragonal phase in room-temperature x-ray patterns is indicative of the existence of the cubic phase above 130°C.

Although the tetragonal and hexagonal phases of BaTiO<sub>3</sub> have similar x-ray patterns, the differences are nevertheless sufficient to make a conclusive identification. The main features distinguishing the hexagonal phase are the presence of peaks with  $d=3.39$  and  $2.18 \text{ \AA}$  and the shift of the 110 peak from ~2.83 to  $2.86 \text{ \AA}$ . Because of the similarities between the two patterns it is probably not possible to detect mixtures of the two phases where one is present in only minute quantities.

However, in most cases the proportions of the two phases in a mixture can be estimated roughly.

Two primary methods were employed to characterize the chemical purity of the powders. These were atomic emission spectrography and secondary ion mass spectrometry (SIMS). The former analyses were performed by two separate, independent laboratories (Burgess Analytical Laboratory and Pacific Spectrochemical Laboratory), while the latter analyses were performed by Dr. Robert G. Wilson of Hughes Research Laboratories using the facilities of Charles Evans and Associates. The Burgess analyses were semi-quantitative estimates for a limited number of elements. The elements and their respective detection limits are given in Table 2-5. Pacific Spectrochemical's analyses surveyed all elements. Quoted detection limits for most elements of interest were in the range 1 to 20 ppm. The SIMS analyses were performed on disk-shaped pellets pressed from the powders. These were analyzed using both oxygen and cesium primary beams. The concentration figures quoted are semi-quantitative estimates based upon the intensities of Ba and Ti in the samples and curves of SIMS sensitivity factors versus ionization potential or electron affinity established for other materials using ion implanted calibration standards.

## C. RESULTS

### 1. RAP Processing

RAP experiments were performed with two primary objectives: (1) to establish process conditions (temperature, oxygen pressure, halogen pressure) that are compatible with  $\text{BaTiO}_3$  stability and would not cause decomposition; and (2) to characterize the physical and/or chemical changes induced by such treatments. The question of the hexagonal phase stability was addressed by means of quenching experiments (see below).

Run conditions for all RAP experiments are listed in Table 2-A1. In early experiments, the effects of a variety of

Table 2-5. Elements Sought by Burgess  
Analytical Laboratory

Element	Detection Limit (wt %)
Te	0.05
Na, P, Ta, Th, W	0.01
Ca, Cd, Co, Hg, Sr, Tl, Zn, Pt	0.005
As, Nb, Sb	0.001
Al, B, Bi, Cr, Cu, Fe, Ga, Ge, In, Mg, Mn, Mo, Ni, Pb, Si, Sn, Ti, V, Zr	0.0005
Ag, Be	0.0001



gases, including air,  $O_2$ ,  $N_2$ , and  $CO/CO_2$ , and process temperatures between 700 and 1500°C were evaluated for several  $BaTiO_3$  specimens. Experiments at 1500°C resulted in at least partial conversion to the hexagonal phase. Later experiments involved the addition of  $I_2$  or  $Br_2$  to the process atmosphere. Treatment with  $CO/CO_2/Br_2$  resulted in complete decomposition of the  $BaTiO_3$ , presumably as a result of at least partial conversion of the oxide to the halide. This problem was avoided in subsequent runs by using an  $O_2/CO_2$  mixture with  $Br_2$  rather than  $CO/CO_2$ . The final series of runs surveyed the effects of treatments at 500 and 1000°C in atmospheres of  $O_2/CO_2/Br_2$ ,  $O_2/CO_2/I_2$ , and  $CO/CO_2/I_2$  for several powders. In all cases, the final product was completely  $BaTiO_3$ , with no evidence of any decomposition.

One indication of changes induced by RAP treatments can be obtained from DSC measurements of the tetragonal-cubic transition near 130°C (Table 2-A1). The highest transition temperatures were observed for JMC powder, with Ferro-1 powder typically having a 2 to 3°C lower transition temperature. This difference is almost certainly due to the higher impurity content of the Ferro-1 powder. No significant effect on the transition temperature was evident that could be ascribed to atmosphere alone except for several cases where  $CO/CO_2/I_2$  produced a notable (~10 to 15°C) lowering of the peak temperature. Also, RBT 19 and 22A, which were synthesized from  $BaCO_3 + TiO_2 + Fe_2O_3$  (with 500 ppm Fe) had a peak temperature 5 to 7°C lower than a sample prepared identically except for the absence of Fe (RBT 21A). In general, there was found to be a significant effect of sintering on the transition, with very fine grain size apparently causing a depression and broadening of the peak. Thus, those samples treated only at lower temperatures tend to have lower transition temperatures and less well defined peaks. Since the JMC powder sintered far less easily than the Ferro and other powders, it was necessary to treat it at 1400 to 1500°C before maximum peak temperatures were obtained.

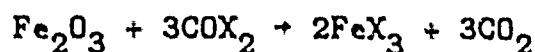
SIMS analyses were performed on the untreated JMC powder and three RAP-treated specimens of the same powder. These experiments were chosen to provide a comparison between samples treated at 500 and 1000°C and in both  $O_2/CO_2/Br_2$  and  $CO/CO_2/I_2$  atmospheres. Elements detected at levels  $\geq 1$  ppm are listed in Table 2-8. The principal impurities found in the untreated powder were P and Cl, with lesser amounts of Na, Al, Si, and  $^{90}Zr$  detectable. The Cl content was, within the resolution of these experiments, unaffected by any of the RAP treatments. However, a fluorine impurity was evidently added by the RAP treatment and was particularly enhanced in the  $CO/CO_2/I_2$  RAP. The source of this impurity is uncertain but may derive from the tubing used in the gas system. The greater level observed in the  $I_2$ -treated sample may be due to the presence of teflon stopcocks used to isolate the  $I_2$  chamber and which were warmed by the water bath and heat lamp, or because of the heating (to  $\sim 90^\circ C$ ) of the tubing to prevent  $I_2$  precipitation. However, it is probable that, whatever its source, the F would have been more easily incorporated into the  $BaTiO_3$  during the  $CO/CO_2/I_2$  RAP because of the very low oxygen partial pressure for this gas mixture.

It is also clear that significant amounts of Br were incorporated in  $O_2/CO_2/Br_2$  treatments, and minor amounts of I were incorporated by the  $I_2$  treatment. However, because the analyses were performed on powder samples, one cannot exclude the possibility that some or all of this apparent impurity was present as a surface adsorbent and may not have penetrated into the solid. There is some indication of cross-contamination of  $I_2$  and  $Br_2$ , possibly resulting from residues left in the furnace tube and/or gas inlet. The only other impurity apparently present at higher levels in the treated samples is Fe. It is difficult to determine the source of this contaminant, but several possibilities are worth considering. First, the Fe may originate as particulate contamination in the bottled gases, arising from the cylinders themselves. There were no other Fe-bearing parts used in the gas system with the exception of the

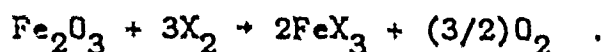
Table 2-8. Impurities >1 ppm Detected by SIMS  
 Analysis of "As-Received" and RAP-Treated  
 JMC BaTiO<sub>3</sub> Powders, ppm atomic

Element	untreated	RBT 37 500°C O <sub>2</sub> /CO <sub>2</sub> /Br <sub>2</sub>	RBT 44 1000°C O <sub>2</sub> /CO <sub>2</sub> /Br <sub>2</sub>	RBT 43 1000°C CO/CO <sub>2</sub> /I <sub>2</sub>
F	240	2100	2100	9000
Na	4	42	18	12
Al	0.3	1.4	1.0	2.8
Si	1.4	9	7	2.8
Cl	700	500	350	500
Fe	0.09	56	7	47
Br		12000	7200	720
I		8	2	160
Pt	6	7	12	20
Blank indicates element not detected.				

gas cylinder pressure regulators and the flowmeter valves. These parts were upstream from the addition of  $I_2$  or  $Br_2$  to the atmosphere and therefore could not have been corroded by the halogens. Second, it is possible that the Fe was derived from impurities in the  $Al_2O_3$  process tube and was transported to the sample as a volatile halide through reactions such as:



or



An alternative explanation is that the Fe is actually an artifact of the sample preparation technique, which involved pressing the powder samples into pellets using a steel piston and dye. Widely differing values could have been obtained if the sputtering depth was different for the various samples.

The results of emission spectrographic analyses are listed in Tables 2-7 and 2-8. The major impurities detected were Si, Ca, and Sr, with lesser amounts of Mg, Al, Mn, Fe, Ni, Cu, Zr, and Pt also sometimes present. The Ferro-1 powder was found by Pacific Spectrochemical to contain significant levels of Sr, in accord with the manufacturer's analysis (Table 2-2). The JMC and Ferro-2 powders were quite low in Sr. Burgess did not report Sr for any samples, and reported Ca only for the untreated powders (analyses of the "as received" powders were carried out separately from the remainder, which were all performed at the same time and thus were done under comparable conditions). The fact that Fe was undetected in essentially all the emission spectrographic analyses lends credence to the possibility mentioned above that the SIMS data were subject to contamination from the pellet press. The Pacific Spectrochemical analyses suggest the possibility of somewhat higher impurity levels in RBT 44 than in other RAP treatments of the same JMC powder. However, the SIMS data do not substantiate this difference. Other than this, there is no clear evidence from the emission

Table 2-7. Emission Spectrographic Analyses of  
RAP-Treated BaTiO<sub>3</sub> Powders, Weight %  
(Burgess Analytical Laboratory)

Element	RBT 37	RBT 38	RBT 39	RBT 41	RBT 42	RBT 43	RBT 44	RBT 47B	RBT 49
Mg	<0.005	<0.005	.005-.05	.005-.05	.005-.05	<0.005	<0.005	<0.005	<0.005
Al	<0.005	<0.005	.005-.05	.05-.5	.005-.05	<0.005	<0.005	.005-.05	<0.005
Si	.005-.05	<0.005	.005-.05	.005-.05	.005-.05	.005-.05	.005-.05	.005-.05	.005-.05
Mn								<0.005	
Fe		<0.005	<0.005	<0.005	<0.005		<0.005	<0.005	<0.005
Ni							.005-.05	.005-.05	
Pt	<0.005			.005-.05	.005-.05	.005-.05	<0.005	.005-.05	.005-.05
Blank indicates element not detected.									

Table 2-8. Emission Spectrographic Analyses of  
RAP-Treated BaTiO<sub>3</sub> Powders, Weight %  
(Pacific Spectrochemical Laboratory)

Element	RBT 37	RBT 38	RBT 39	RBT 41	RBT 42	RBT 43	RBT 44	RBT 47B	RBT 49
Mg	0.0002	<0.0001	0.0007	0.0007	0.0006	<0.0001	<0.0001	0.0002	<0.0001
Al							<0.0001		
Si	0.0062	<0.004	<0.004	0.0084	0.0076	0.0046	0.010	0.0077	0.0061
Ca	0.0033	0.0045	0.016	0.025	0.017	0.0025	0.011	0.0071	0.005
Mn		0.0008							
Ni							0.0013	<0.001	
Sr		<0.004	0.035	0.043	0.037				
Blank indicates element not detected.									

spectrographic analyses of any substantial differences between samples attributable to the various RAP atmospheres and temperatures.

## 2. Quenching Experiments

Run conditions and results for all quenching runs are reported in Table 2-A2. Preliminary quenching experiments were aimed at studying the cubic-hexagonal transition for two different powders heated in air. The two powders used were the Ferro-1 and JMC powders. In order to bracket the equilibrium phase boundary in these experiments, it is necessary that actual conversion from one phase to another must occur. Thus, in order to prove that an experiment is within the hexagonal stability field, one must convert an initially cubic sample to the hexagonal phase. To prove the cubic phase stability, one must convert hexagonal  $\text{BaTiO}_3$  to the cubic phase. To perform the latter type of experiment, the initially tetragonal (cubic) powders were first heated to near  $1500^\circ\text{C}$ , where they were shown to convert completely to the hexagonal phase. These were then cooled down to a temperature where they were held before quenching. Appearance of the cubic phase in such experiments indicated that the process temperature was below the cubic-hexagonal transition. In some cases, only partial conversion was achieved. This was believed to be due to kinetic factors and can be accepted as indicating stability as if complete conversion had occurred.

The results of these experiments for the Ferro-1 and JMC powders are summarized in Figure 2-5. There appear to be two significant differences between these materials. The Ferro-1 powder transition occurs between  $1440$  and  $1450^\circ\text{C}$ , while in the JMC powder it occurs at a somewhat lower temperature, between  $1400$  and  $1440^\circ\text{C}$ . The second difference is in the kinetics of the phase transition. In the JMC powder there is a much wider range of temperatures over which only partial conversion was achieved. Even  $68$  hours at  $1400^\circ\text{C}$  produced a sample that remained largely

2-29



hexagonal for the JMC powder, whereas 1 h at 1440 or below was sufficient to convert hexagonal Ferro-1 powder completely back to cubic.

For comparison, the cubic-hexagonal transition temperature reported by Rase and Roy<sup>2</sup> was 1460°C, somewhat higher than that found here. This discrepancy, and the difference in transition temperatures of our two samples, could be due to differing impurity contents. In particular, Sr is known to raise the transition temperature and is a common impurity present at differing concentrations in various samples. It is interesting to note that the higher-purity sample, the JMC powder, had the lower transition temperature, which is consistent with this interpretation. It is not clear what causes the difference in kinetics between the two powders. Because the transition is reconstructive in nature, it must be a diffusion-limited process. Diffusion is perhaps inhibited in the JMC powder due to a lower defect density in the higher-purity material.

A short series of experiments (QBT 40 to 45) was aimed at determining whether increasing the partial pressure of oxygen might cause an increase in the cubic-hexagonal transition temperature. Use of 100% O<sub>2</sub> at 1460 and 1500°C resulted in formation of the hexagonal phase in both Ferro-1 and JMC powders. Thus, if there is any significant effect of O<sub>2</sub> on the transition temperature, higher pressures would be required to observe it. Since it is unlikely that any Ti<sup>3+</sup> would exist in the presence of 1 atm of O<sub>2</sub>, it can also be concluded that Ti<sup>3+</sup> must not be the only factor responsible for stabilizing the hexagonal phase. The O<sub>2</sub> atmosphere proved to be quite corrosive to the Pt foil capsules, and further use of such an atmosphere was discontinued.

Runs QBT 46 and 47 were an attempt to determine if there is an effect of Fe doping on the cubic-hexagonal transition temperature in air. Both samples were synthesized in identical fashion from BaCO<sub>3</sub> + TiO<sub>2</sub> mixes, but the sample used in QBT 46 was prepared with a substitution of Fe<sub>2</sub>O<sub>3</sub> for 2TiO<sub>2</sub> at a level of 500 ppm by weight of Fe. This Fe-bearing sample did convert

partially to the hexagonal phase at 1440°C, whereas the sample without Fe did not convert to hexagonal. This suggests a probable lowering of the transition temperature due to Fe-doping, although this interpretation is not conclusive.

Runs QBT 48 and 49 repeated the conditions used for QBT 30 and 31 (1450°C, air) but with powders that had undergone a CO/CO<sub>2</sub>/I<sub>2</sub> RAP at 700°C. The JMC powder gave essentially the identical results both with and without RAP treatment. However, the Ferro-1 powder, which produced some hexagonal phase when heated before RAP remained completely cubic after the RAP treatment. This result is consistent with an increase of the transition temperature as a result of the RAP treatment but does not prove this contention.

In run QBT 50, a CO/CO<sub>2</sub>/I<sub>2</sub> atmosphere was introduced for the first time in high-temperature processing. It was noted that the powder had a blue color after processing, presumably indicating some loss of oxygen. In runs 51 to 61, the relative proportions of CO, CO<sub>2</sub>, and I<sub>2</sub> were varied in order to study their effect on the reduction behavior. It was found that the presence of I<sub>2</sub> was responsible for imparting a dark color to the samples. However, even in a pure CO<sub>2</sub> atmosphere with no CO or I<sub>2</sub> added, both the Ferro-1 and JMC powders were blue colored when quenched from near the melting point. Because it has previously been suggested that reduction probably favors the stability of the hexagonal phase,<sup>10,11</sup> it was decided to determine whether a gas mixture could be found that did not result in any visible coloration. Use of an O<sub>2</sub>/CO<sub>2</sub> atmosphere with a 1:1 ratio was found to produce colorless samples (QBT 62 to 63).

In runs 64 and 65, samples that had been treated with a CO/CO<sub>2</sub>/Br<sub>2</sub> atmosphere at 800°C were reheated in an O<sub>2</sub>/CO<sub>2</sub> atmosphere. Following the low-temperature treatments, both samples had decomposed (though not in identical ways) so that no BaTiO<sub>3</sub> could be detected in either one. X-ray diffraction patterns of the samples were complicated and could not be readily identified, however it seems likely that they contained various

bromates and/or bromides. It was decided to reheat them in an oxidizing atmosphere to see if they could be reconverted back to  $\text{BaTiO}_3$ . This was apparently successful. Both samples melted, and upon quenching, one consisted of a mixture of tetragonal and hexagonal  $\text{BaTiO}_3$  while the other was essentially completely hexagonal. The indication of some cubic  $\text{BaTiO}_3$  suggested a possible favorable result of the  $\text{Br}_2$  treatment. Subsequent experiments (QBT 66 to 69) were performed on JMC and Ferro-1 powders (without previous RAP treatment) in  $\text{CO}/\text{CO}_2/\text{Br}_2$  atmospheres at 1616 and 1600°C. QBT 66 resulted in a nearly completely cubic  $\text{BaTiO}_3$  with a small amount of at least one additional phase (probably  $\text{Ba}_6\text{Ti}_{17}\text{O}_{40}$ ) present. All were at least partially melted and had varying amounts of unidentified non- $\text{BaTiO}_3$  material present. The  $\text{Br}_2$  pressure for these runs was ~0.026 atm.

As pointed out earlier, the conversion of oxide to halide is a possible consequence of treatment with the halogens. However, this problem can be alleviated by maintaining a suitably high ratio of  $\text{O}_2/\text{X}_2$ . The indications of the preceding experiments were that this ratio was too low, and therefore some decomposition was occurring. Since the oxygen partial pressure of a  $\text{CO}/\text{CO}_2$  mixture is quite low ( $\sim 10^{-5}$  atm for the experiments just described), it was necessary to eliminate the carbon monoxide from the gas mixture and replace it with oxygen. At the same time, the  $\text{Br}_2$  pressure was reduced to 0.0066 atm for all subsequent experiments.

Run QBT 70 (Ferro-1 powder,  $\text{O}_2/\text{CO}_2/\text{Br}_2$ , ~1600°C) produced all cubic  $\text{BaTiO}_3$  with barely detectable traces of an unidentifiable second phase. Under the same conditions (QBT 71) the JMC powder was entirely hexagonal. The cubic phase was also obtained using the Alfa starting material (QBT 73). In QBT 74, the Ferro-1 powder was melted and recrystallized to give cubic  $\text{BaTiO}_3$  plus a second phase ( $\text{Ba}_6\text{Ti}_{17}\text{O}_{40}$ ). Melting of the JMC powder under the same conditions gave mainly hexagonal  $\text{BaTiO}_3$  plus some cubic  $\text{BaTiO}_3$  and  $\text{Ba}_6\text{Ti}_{17}\text{O}_{40}$ . In runs QBT 76 to 83, the same

experimental conditions under which cubic  $\text{BaTiO}_3$  was obtained with Ferro-1 and Alfa powders were used to treat samples of other  $\text{BaTiO}_3$  powders. Only the Ferro-2 powder yielded a cubic result; the rest were all hexagonal.

The results described above seemed to suggest that the Alfa, Ferro-1, and Ferro-2 powders, when heated in the  $\text{O}_2/\text{CO}_2/\text{Br}_2$  atmosphere, were in the cubic phase at temperatures close to the melting point. However, all of the other samples tested produced the hexagonal phase, possibly indicating some important difference between these materials. In order to test whether the  $\text{Br}_2$  RAP was indeed responsible for stabilizing the cubic phase, we next repeated the experiments using Alfa and Ferro-2 powders in  $\text{O}_2/\text{CO}_2$  without  $\text{Br}_2$ . Unexpectedly, the Ferro-2 powder was cubic at the quenching temperature, while the Alfa powder was hexagonal. These experiments were then repeated except that the samples were introduced into the furnace at the peak temperature rather than ramping the samples up to temperature in the furnace. In this case, both powders were hexagonal. These experiments suggested that the  $\text{Br}_2$  may not have been responsible for the appearance of the cubic phase, but rather that the cubic phase was sometimes preserved metastably throughout a slow ramp from  $\sim 1200$  to  $1600^\circ\text{C}$ .

The final series of experiments (QBT 88 to 97) was an attempt to reproduce the earlier results indicating possible cubic stability and to examine whether perhaps the amount of time during which the samples were exposed to  $\text{Br}_2$  was an important factor. It was found that holding the samples at  $1592^\circ\text{C}$  for four hours resulted in their melting. The solidified product was largely tetragonal  $\text{BaTiO}_3$  (with some hexagonal) plus  $\text{Ba}_6\text{Ti}_{17}\text{O}_{40}$ . This result, along with QBT 74 and 75, strongly suggests that the composition of the melt changed, probably becoming more  $\text{TiO}_2$ -rich than  $\text{BaTiO}_3$ . The probable cause of such behavior is a loss of  $\text{BaO}$ -component from the melt, presumably as a result of forming a volatile barium bromide compound. Experiments in which the sample weight was measured carefully before and after the runs

(QBT 92 to 95) suggest that there was a significantly greater weight loss in the presence of  $\text{Br}_2$  than without  $\text{Br}_2$ . There was also a dependence of weight loss upon how loosely the sample was packed into its capsule. However, none of these experiments, with either Alfa, Ferro-1, or Ferro-2 powders, was successful in reproducing the earlier observations of cubic  $\text{BaTiO}_3$  quenched from near  $1600^\circ\text{C}$ .

It can therefore be concluded that the appearance of cubic  $\text{BaTiO}_3$  in unmelted samples quenched from near  $1600^\circ\text{C}$  was probably not an equilibrium phenomenon. Although RAP-induced stabilization of the cubic phase cannot be completely ruled out, the preponderance of evidence suggests that the observed behavior is more likely indicative of the metastable persistence of the cubic phase in some experiments. Differences between the various powders studied may reflect differences in the kinetics of the phase transition in these powders. In several experiments where  $\text{BaTiO}_3$  powders were melted, the cubic phase was also sometimes obtained. The appearance of an additional phase, probably  $\text{Ba}_6\text{Ti}_{17}\text{O}_{40}$ , in the products indicates that the melts were driven off composition, probably due to reaction with  $\text{Br}_2$  in the atmosphere. Assuming the melt was depleted in BaO-component, the crystallization behavior would be governed by the composition-dependent liquidus surface in the  $\text{BaTiO}_3$ - $\text{TiO}_2$  system and, even with relatively little  $\text{TiO}_2$  enrichment, would be expected to produce cubic  $\text{BaTiO}_3$ . The fact that melting of JMC powder under these conditions was somewhat more likely to produce hexagonal  $\text{BaTiO}_3$  (plus  $\text{Ba}_6\text{Ti}_{17}\text{O}_{40}$ ) may be another indication of the sensitivity of the transition behavior to impurities. Alternatively, since the phase diagram<sup>2</sup> suggests that the hexagonal phase will crystallize for very small amounts of  $\text{TiO}_2$  excess, it is possible that the melt derived from the JMC powder became less depleted in BaO.

Table 2-A1. Reactive Atmosphere Processing Experiments

RBT Run #	Starting Material	T(°C)	Time(h)	Atmosphere	X-ray <sup>a</sup>	DSC Peak Temp(°C)
1	Ferro-1	1415	16	air	T	130
2	Ferro-1	1400	16	O <sub>2</sub>	T	130
3	Ferro-1	1400 <sup>b</sup>	18	N <sub>2</sub>	T	130
5	JMC	1400	15	air	T	131.5 <sup>c</sup>
6	Ferro-1	1400	15	CO <sub>2</sub>	T	131
7	Ferro-1	1400	18	CO	T+H	131.5
8	JMC	1400	18	CO	T+H	129
9	Alfa	1400	21	air	T	130.5
10	Ferro-1	1500	20	O <sub>2</sub>	T+(H)	130
11	#7 <sup>e</sup>	1500	20	O <sub>2</sub>	T	131
12	Ferro-1	700	21	CO	T	128.5 <sup>f</sup>
13	JMC	700	21	CO	T	126 <sup>f</sup>
14	BaTiO <sub>3</sub> <sup>g</sup>	1400	15	air	T+B	130.5
15	Ferro-1	1500	18	CO/CO <sub>2</sub>	T+H	130.5
16	JMC	1500	18	CO/CO <sub>2</sub>	T+H	133
17	#12 <sup>e</sup>	1500	20	CO <sub>2</sub>	T+(H)	130.5
18	#13 <sup>e</sup>	1500	20	CO <sub>2</sub>	T	133
19	Mix <sup>h</sup>	1200	40	air		
19A	#19 <sup>e</sup>	1400	23	air	T+(H)	123.5
20	Mix <sup>j</sup>	1200	63	air		
20A	#20 <sup>e</sup>	1400	20	air	T	130.5
21	#20A <sup>e</sup>	1500	16	air	H	k
21A	#21 <sup>e</sup>	1400	2	air	T	130.5

Table 2-A1. Continued.

RBT Run #	Starting Material	T(°C)	Time(h)	Atmosphere	X-ray <sup>a</sup>	DSC Peak Temp(°C)
22	#19A <sup>e</sup>	1500	16	air	H	k
22A	#22 <sup>e</sup>	1400	16	air	T	125
23	BaTiO <sub>3</sub> <sup>g</sup>	1500	6	CO <sub>2</sub>	T+B	
24	JMC	1500	21	O <sub>2</sub> /H <sub>2</sub> O <sup>d</sup>	H+T	132
25	Ferro-1	1500	21	O <sub>2</sub> /H <sub>2</sub> O <sup>d</sup>	T+(H)	130
26	Mix <sup>i</sup>	700	13	CO <sub>2</sub>	n	
27	Mix <sup>i</sup>	500	86	air	o	
28	BaTiO <sub>3</sub> <sup>g</sup>	1200	18	air	T+B	
29	Ferro-1	700	51	CO/I <sub>2</sub>	T	127.5 <sup>f</sup>
30	JMC	700	51	CO/I <sub>2</sub>	T	124.5 <sup>f</sup>
31	Ferro-1	1000	13	CO/I <sub>2</sub>	T	128 <sup>f</sup>
32	JMC	1000	13	CO/I <sub>2</sub>	T	126 <sup>f</sup>
33	Ferro-1	1500	14	CO/I <sub>2</sub>	H+T	121.5
34	JMC	1500	14	CO/I <sub>2</sub>	H+(T)	122.5 <sup>f</sup>
35	JMC	800	31	CO/CO <sub>2</sub> /Br <sub>2</sub>	m	
36	Ferro-1	800	31	CO/CO <sub>2</sub> /Br <sub>2</sub>	m	
37	JMC	500	30	O <sub>2</sub> /CO <sub>2</sub> /Br <sub>2</sub>	T	k
38	Ferro-2	515	51	O <sub>2</sub> /CO <sub>2</sub> /Br <sub>2</sub>	T	128 <sup>f</sup>
39	Ferro-1	519	47	O <sub>2</sub> /CO <sub>2</sub> /I <sub>2</sub>	T	128.5
40	Mix <sup>i</sup>	676	24	O <sub>2</sub> /Br <sub>2</sub>	l	
41	Ferro-1	1021	19	O <sub>2</sub> /CO <sub>2</sub> /I <sub>2</sub>	T	128
42	Ferro-1	984	18	CO/CO <sub>2</sub> /I <sub>2</sub>	T	118.5
43	JMC	1014	19	CO/CO <sub>2</sub> /I <sub>2</sub>	T	115 <sup>f</sup>
44	JMC	990	19	O <sub>2</sub> /CO <sub>2</sub> /Br <sub>2</sub>	T	k
47B	Mix <sup>j</sup>	1080	18	O <sub>2</sub> /CO <sub>2</sub> /Br <sub>2</sub>	T	129
49	JMC	500	20	CO/CO <sub>2</sub> /I <sub>2</sub>	T	k
50	JMC <sup>p</sup>	500	24	CO/CO <sub>2</sub> /I <sub>2</sub>	T	

# Notes to Table 2-A1

- a. T = tetragonal, H = hexagonal, B =  $\text{Ba}_6\text{Ti}_{17}\text{O}_{46}$ , ( ) = trace.
- b. Temp. dropped to 1270°C during run.
- c. Peak has shoulder on high temperature side.
- d.  $\text{O}_2$  bubbled through  $\text{H}_2\text{O}$  at room temperature.
- e. Starting material was the product of run # indicated.
- f. Broad peak.
- g.  $\text{BaTiO}_3$  prepared from  $\text{Ba}(\text{OH})_2$  + tetrabutyltitanate.
- h.  $\text{BaCO}_3$  +  $\text{TiO}_2$  +  $\text{Fe}_2\text{O}_3$  (500 ppm Fe).
- i.  $\text{Ba}(\text{NO}_3)_2$  +  $\text{TiO}_2$ .
- j.  $\text{BaCO}_3$  +  $\text{TiO}_2$ .
- k. Peak very weak or absent.
- l.  $\text{BaTiO}_3(\text{T})$  +  $\text{TiO}_2$  + ?
- m. Phase(s) could not be identified.
- n.  $\text{BaTiO}_3(\text{T})$  +  $\text{BaCO}_3$  +  $\text{TiO}_2$  +  $\text{BaO}$ .
- o.  $\text{BaTiO}_3(\text{T})$  +  $\text{BaCO}_3$  +  $\text{TiO}_2$  +  $\text{Ba}(\text{NO}_3)_2$ .
- p. Sample flushed with argon before removal from furnace and during packaging.



Table 2-A2. RAP Quenching Experiments

QBT Run #	Starting Material	Maximum Temp. (°C)	Quench Temp. (°C)	Time (h) <sup>b</sup>	Atmosphere	X-ray <sup>f</sup>
1	JMC	1612	1612	0.5	air	H
2	JMC	1627	1627	0.5	air	H
3	Ferro-1	1455	1455	1.5	air	T
4	JMC	1455	1455	1.5	air	T+H
5	Ferro-1	1499	1499	1.0	air	T
6	JMC	1499	1499	1.0	air	H
7	Ferro-1	1494 <sup>a</sup>	1494	1.0	air	H
8	JMC	1494 <sup>a</sup>	1494	1.0	air	H
9	Ferro-1	1496 <sup>a</sup>	1426	1.0	air	T
10	JMC	1496 <sup>a</sup>	1426	1.0	air	H
11	Ferro-1	1482 <sup>a</sup>	1482	1.0	air	H
12	JMC	1482 <sup>a</sup>	1482	1.0	air	H
13	Ferro-1	1492 <sup>a</sup>	1412	1.0	air	T
14	JMC	1492 <sup>a</sup>	1412	1.0	air	H
15	Ferro-1	1498 <sup>a</sup>	1410	1.0	air	T
16	JMC	1498 <sup>a</sup>	1410	1.0	air	H
17	Ferro-1	1498 <sup>a</sup>	1428	15.0	air	T
18	JMC	1498 <sup>a</sup>	1428	15.0	air	H
19	Ferro-1	1498 <sup>a</sup>	1400	68.0	air	T
20	JMC	1498 <sup>a</sup>	1400	68.0	air	H+T
21	Ferro-1	1604 <sup>a</sup>	1604	1.0	air	H
22	JMC	1604 <sup>a</sup>	1604	1.0	air	H
23	JMC	1600 <sup>a</sup>	1600	1.0	air	H
24	JMC	1460 <sup>a</sup>	1460	42.0	air	H
25	Ferro-1	1460 <sup>a</sup>	1460	42.0	air	H
26	JMC	1466 <sup>a</sup>	1466	23.5	air	H
27	Ferro-1	1466 <sup>a</sup>	1466	23.5	air	H
28	JMC	1477 <sup>a</sup>	1477	23.0	air	H
29	Ferro-1	1477 <sup>a</sup>	1477	23.0	air	H
30	JMC	1448 <sup>a</sup>	1448	24.0	air	T+H

Table 2-A2. Continued.

QBT Run #	Starting Material	Maximum Temp. (°C)	Quench Temp. (°C)	Time(h) <sup>b</sup>	Atmosphere	X-ray <sup>f</sup>
31	Ferro-1	1448 <sup>a</sup>	1448	24.0	air	T+H
32	JMC	1440 <sup>a</sup>	1440	23.0	air	T+(H)
33	Ferro-1	1440 <sup>a</sup>	1440	23.0	air	T
34	JMC	1500 <sup>a</sup>	1440	41.0	air	H
35	Ferro-1	1500 <sup>a</sup>	1440	21.0	air	T
36	JMC	1500 <sup>a</sup>	1430	25.5	air	H
37	Ferro-1	1500 <sup>a</sup>	1430	25.5	air	T
38	JMC	1500 <sup>a</sup>	1420	23.5	air	H
39	Ferro-1	1500 <sup>a</sup>	1420	23.5	air	T
40	JMC	1460 <sup>a</sup>	1460	21.0	O <sub>2</sub>	H
41	Ferro-1	1460 <sup>a</sup>	1460	21.0	O <sub>2</sub>	H+(T)
42	JMC	1500 <sup>a</sup>	1500	24.0	O <sub>2</sub>	H
43	Ferro-1	1500 <sup>a</sup>	1500	24.0	O <sub>2</sub>	H
44	JMC	1500	1500	24.0	O <sub>2</sub>	H
45	Ferro-1	1500	1500	24.0	O <sub>2</sub>	H
46	RBT 19	1440 <sup>a</sup>	1440	24.0	air	H+T
47	RBT 20	1440 <sup>a</sup>	1440	24.0	air	T
48	RBT 30	1450 <sup>a</sup>	1450	24.0	air	T+H
49	RBT 29	1450 <sup>a</sup>	1450	24.0	air	T
50	JMC	1635	1603	0.5	CO/CO <sub>2</sub> /I <sub>2</sub>	H
51	JMC	1640	1603	1.5	CO/CO <sub>2</sub> /I <sub>2</sub>	H
52	JMC	1623	1603	1.5	CO <sub>2</sub>	H
53	Ferro-1	1623	1603	1.5	CO <sub>2</sub>	H
54	Ferro-1	1623	1603	1.5	CO/CO <sub>2</sub>	H
55	JMC	1623	1603	1.5	CO/CO <sub>2</sub>	H
56	Ferro-1	1623	1603	1.5	CO <sub>2</sub> /I <sub>2</sub>	H
57	JMC	1623	1603	1.5	CO <sub>2</sub> /I <sub>2</sub>	H
58	Ferro-1	1623	1623	1.5	CO/CO <sub>2</sub>	H
59	JMC	1623	1623	1.5	CO/CO <sub>2</sub>	H
60	Ferro-1	1623	1623	1.5	CO <sub>2</sub>	H
61	JMC	1623	1623	1.5	CO <sub>2</sub>	H
62	Ferro-1	1623	1623	1.0	O <sub>2</sub> /CO <sub>2</sub>	H
63	JMC	1623	1623	1.0	O <sub>2</sub> /CO <sub>2</sub>	H
64	RBT 35	1623	1623	1.5	O <sub>2</sub> /CO <sub>2</sub>	H

Table 2-A2. Continued.

QBT Run #	Starting Material	Maximum Temp. (°C)	Quench Temp. (°C)	Time(h) <sup>b</sup>	Atmosphere	X-ray <sup>f</sup>
65	RBT 36	1623	1623	1.5	O <sub>2</sub> /CO <sub>2</sub>	T+H
66	Ferro-1	1616	1616	1.5	CO/CO <sub>2</sub> /Br <sub>2</sub>	T+B
67	JMC	1616	1616	1.5	CO/CO <sub>2</sub> /Br <sub>2</sub>	c
68	Ferro-1	1600	1600	1.0	CO/CO <sub>2</sub> /Br <sub>2</sub>	T+?
69	JMC	1600	1600	1.0	CO/CO <sub>2</sub> /Br <sub>2</sub>	T+?
70	Ferro-1	1603	1603	1.0	O <sub>2</sub> /CO <sub>2</sub> /Br <sub>2</sub>	T
71	JMC	1603	1603	1.0	O <sub>2</sub> /CO <sub>2</sub> /Br <sub>2</sub>	H
72	JMC	1600	1600	1.0	O <sub>2</sub> /CO <sub>2</sub> /Br <sub>2</sub>	H
73	Alfa	1600	1600	1.0	O <sub>2</sub> /CO <sub>2</sub> /Br <sub>2</sub>	T
74	Ferro-1	1630	1600	1.5	O <sub>2</sub> /CO <sub>2</sub> /Br <sub>2</sub>	T+B
75	JMC	1630	1600	1.5	O <sub>2</sub> /CO <sub>2</sub> /Br <sub>2</sub>	H+T+B
76	RBT 20	1596	1596	1.0	O <sub>2</sub> /CO <sub>2</sub> /Br <sub>2</sub>	H
77	JMC	1596	1596	1.0	O <sub>2</sub> /CO <sub>2</sub> /Br <sub>2</sub>	H
78	BaTiO <sub>3</sub> <sup>d</sup>	1597	1597	1.0	O <sub>2</sub> /CO <sub>2</sub> /Br <sub>2</sub>	H
79	JMC	1597	1597	1.0	O <sub>2</sub> /CO <sub>2</sub> /Br <sub>2</sub>	H
80	BaTiO <sub>3</sub> <sup>e</sup>	1597	1597	1.0	O <sub>2</sub> /CO <sub>2</sub> /Br <sub>2</sub>	H
81	JMC	1597	1597	1.0	O <sub>2</sub> /CO <sub>2</sub> /Br <sub>2</sub>	H
82	JMC	1593	1593	1.0	O <sub>2</sub> /CO <sub>2</sub> /Br <sub>2</sub>	H
83	Ferro-2	1593	1593	1.0	O <sub>2</sub> /CO <sub>2</sub> /Br <sub>2</sub>	T
84	Ferro-2	1595	1595	1.0	O <sub>2</sub> /CO <sub>2</sub>	T
85	Alfa	1595	1595	1.0	O <sub>2</sub> /CO <sub>2</sub>	H
86	Alfa	1594 <sup>a</sup>	1594	1.0	O <sub>2</sub> /CO <sub>2</sub>	H
87	Ferro-2	1594 <sup>a</sup>	1594	1.0	O <sub>2</sub> /CO <sub>2</sub>	H
88	Ferro-2	1594 <sup>a</sup>	1594	1.0	O <sub>2</sub> /CO <sub>2</sub> /Br <sub>2</sub>	H
89	Alfa	1594 <sup>a</sup>	1594	1.0	O <sub>2</sub> /CO <sub>2</sub> /Br <sub>2</sub>	H
90	Alfa <sup>g</sup>	1592 <sup>a</sup>	1592	4.0	O <sub>2</sub> /CO <sub>2</sub> /Br <sub>2</sub>	T+H+B
91	Ferro-2 <sup>g</sup>	1592 <sup>a</sup>	1592	4.0	O <sub>2</sub> /CO <sub>2</sub> /Br <sub>2</sub>	T+H+B
92	Alfa	1591	1591	1.5	O <sub>2</sub> /CO <sub>2</sub> /Br <sub>2</sub>	H
93	Alfa	1591	1591	1.5	O <sub>2</sub> /CO <sub>2</sub> /Br <sub>2</sub>	H
94	Alfa	1592	1592	3.0	O <sub>2</sub> /CO <sub>2</sub> /Br <sub>2</sub>	H
95	Alfa	1591	1591	3.0	O <sub>2</sub> /CO <sub>2</sub>	H
96	Ferro-1	1591	1591	1.0	O <sub>2</sub> /CO <sub>2</sub> /Br <sub>2</sub>	H
97	Alfa	1591	1591	1.0	O <sub>2</sub> /CO <sub>2</sub> /Br <sub>2</sub>	H

### Notes to Table 2-A2

- a. Sample not subjected to furnace temperature ramp. Sample entered furnace at the given temperature.
- b. Denotes time at quenching temperature only.
- c. Phase(s) could not be identified.
- d.  $\text{BaTiO}_3$  synthesized from  $\text{Ba}(\text{NO}_3)_2 + \text{TiO}_2$
- e. Fe-doped  $\text{BaTiO}_3$  (100 ppm Fe) synthesized from  $\text{BaCO}_3 + \text{TiO}_2$ .
- f. T = tetragonal, H = hexagonal, B =  $\text{Ba}_6\text{Ti}_{17}\text{O}_{46}$ , ( ) = trace.
- g. Samples melted together creating a single sample.

## REFERENCES (SECTION 2)

1. R.D. Burbank and H.T. Evans, Jr., Acta Cryst. 1, 330 (1948).
2. D.E. Rase and R. Roy, J. Am. Ceram. Soc. 38, 102 (1955).
3. T. Negas, R.S. Roth, H.S. Parker, and D. Minor, J. Solid State Chem. 9, 297 (1974).
4. H.M. O'Bryan, Jr. and J. Thomson, Jr., J. Am. Ceram. Soc. 57, 522 (1974).
5. R.K. Sharma, N.-H. Chan, and D.M. Smyth, J. Am. Ceram. Soc. 64, 448 (1981).
6. B. Jaffe, W.R. Cook, Jr., and H. Jaffe, Piezoelectric Ceramics, Academic Press, New York (1971).
7. J.A. Basmajian and R.C. DeVries, J. Am. Ceram. Soc. 40, 373 (1957).
8. R.C. DeVries and R. Roy, J. Am. Ceram. Soc. 38, 142 (1955).
9. D.E. Rase and R. Roy, J. Am. Ceram. Soc. 38, 393 (1955).
10. J.G. Dickinson, L. Katz, and R. Ward, J. Am. Chem. Soc. 83, 3026 (1961).
11. H. Arend and L. Kihlborg, J. Am. Ceram. Soc. 52, 63 (1969).
12. N.G. Eror, T.M. Loehr, and B.C. Cornilsen, Ferroelectrics 28, 321 (1980).
13. B. Matthias, Phys. Rev. 73, 808 (1948).
14. R.C. Pastor and M. Robinson, Mat. Res. Bull. 9, 569 (1974).
15. R.C. Pastor and A.C. Pastor, Mat. Res. Bull. 10, 117 (1975).
16. R.C. Pastor, L.E. Gorre, R.K. Chew, and A.C. Pastor, Proc. SPIE 297, 86 (1981).
17. R.C. Pastor and L.E. Gorre, Mat. Res. Bull. 16, 1413 (1981).

## SECTION 3

### ORIGINS OF THE PHOTOREFRACTIVE EFFECT

#### A. INTRODUCTION

In the work performed for this task, we have drawn on information in the literature and our own experiments to identify and characterize the photorefractive species in  $\text{BaTiO}_3$ . Preliminary results of our effort have been published,<sup>5,6</sup> and are included as Appendices 1 and 2. Our approach follows the spirit of the early research<sup>1-3</sup> on the origins of the photorefractive effect in  $\text{LiNbO}_3$ , as well as a subsequent study of photorefractive centers in Fe-doped  $\text{LiNbO}_3$ .<sup>4</sup> Common elements between this work and ours are the judicious use of evidence from the literature, as well as detailed electron paramagnetic resonance (EPR) and optical absorption measurements. In addition, our approach adds another diagnostic technique: photorefractive beam coupling. The preliminary results of our study are given in Appendix 1 (Reference 5).

The general arrangement of this section is as follows. In Section B the experimental methods are outlined. Section C is devoted to developing the general background and models with special emphasis on deep level defects and electrical transport. The experimental results obtained from beam coupling measurements, absorption spectra, impurity analysis, and electron paramagnetic resonance measurements are discussed in Section D. In Section E we discuss the interpretation of the data, with attention given to the study of correlations between the measured parameters, and the relationship to existing energy level calculations. A general discussion of the results and recommendation for material optimization are given in Section F.

#### B. EXPERIMENTAL

##### 1. Samples

The samples for all our experiments were purchased from Sanders Associates, Nashua, NH. The crystals as supplied had

been mechanically poled to eliminate 90° domains. We then electrically poled these samples to control 180° domains. The technique consisted of heating the crystals in oil to 120 to 130°C, applying a few kV/cm and cooling to room temperature. Without further characterization, it is difficult to determine the effectiveness of our electrical poling procedure. If 180° domains remain in a sample (and they are uniformly distributed), their effect is to reduce all second order parameters of the crystal in proportion to the number of remaining 180° domains. The parameters affected by incomplete poling include the pyroelectric, piezoelectric, electro-optic and nonlinear optic coefficients. One objective of our measurements is to determine the degree of poling in our samples.

The identity and concentration of impurities was determined by both secondary ion mass spectroscopy (SIMS) and spark source emission spectroscopy (Burgess Analytical Labs, North Adams, MA).

## 2. Beam Coupling Measurements

Steady-state beam coupling is a convenient technique for measuring several important parameters in a photorefractive crystal. Our beam coupling measurements in BaTiO<sub>3</sub> and their interpretation are described in detail in Appendix 2 (Reference 6).

We have measured the amplitude and the sign of the beam coupling gain as a function of grating period in nine BaTiO<sub>3</sub> samples. The laser source was a cw He-Cd laser operating in the fundamental transverse mode and having a coherence length of ~5 cm. The output beam from the laser was divided at a beam splitter, and the two resulting beams were recombined at the sample in such a way that the input angle and thus the grating period could be varied while the path lengths of the two beams were kept equal. In all our experiments, the grating normal was aligned parallel with the  $\hat{c}$ -axis. Both input beams were s-polarized (along a crystalline  $\hat{a}$ -axis) to exploit the refractive index change induced through the electro-optic tensor

component  $r_{13}$ . The signal beam had a power of  $\sim 10 \mu\text{W}$  and a diameter of  $\sim 2 \text{ mm}$ . The reference beam was expanded with a telescope to a diameter of  $\sim 5 \text{ mm}$  in order to maintain a uniform interaction region over the length of the crystal as the input angle was varied. The power in this beam was made sufficiently large ( $\sim 5 \text{ mW}$ ) to insure that it would remain undepleted in our experiments. At the resulting level of irradiance ( $\sim 20 \text{ mW/cm}^2$ ), the photoconductivity is approximately three orders of magnitude larger than the dark conductivity, as measured in two of our crystals.

### 3. Electron Paramagnetic Resonance Measurements

EPR spectra were recorded at X-band with a Varian E-9 spectrometer equipped with a Hewlett-Packard 5342A automatic microwave frequency counter and a Varian NMR Gaussmeter for magnetic field measurements. Single crystal spectra were made by aligning the sample (with faces normal to principal directions) on a flat surface on the shaft of a single circle goniometer. The error in the alignment of the crystal axes relative to the axes of rotation is estimated to be  $\pm 3^\circ$ , whereas the estimated error in the crystal orientation relative to the magnetic field is  $\pm 1^\circ$  and is determined by the resolution of the goniometer dial. The concentration of spins (e.g.,  $\text{Fe}^{3+}$ ) was obtained by comparison to a calibrated reference sample of powdered  $\text{Cr}_2\text{O}_3$  ( $\text{Cr}^{3+}$ ;  $g=1.9796$ ), which was contained in a capillary tube mounted next to the  $\text{BaTiO}_3$  sample. The chromium sample was calibrated against a Varian  $3.3 \times 10^{-4}\%$  pitch on KCl standard. The accuracy in the determination of the absolute number of spins (e.g.,  $\text{Fe}^{3+}$ ) in the  $\text{BaTiO}_3$  sample is  $\pm 50\%$ ; the relative accuracy is  $\pm 10\%$ .

### 4. Optical Absorption Measurements

The absorption coefficient  $\alpha$  at specific wavelengths was obtained from laser transmission measurements, with account taken for Fresnel reflections from the entrance and exit faces. For



each measurement, care was taken to avoid interference effects from multiple reflections within the sample. The crystals were measured with a beam propagating normal to the  $\hat{c}$ -axis, and with the optical electric field vector  $\vec{E}$  either parallel and perpendicular to the  $\hat{c}$ -axis. For this geometry, photorefractive coupling between the incident and reflected beams in the crystal can be neglected, since the effective electro-optic coefficient for this interaction is small. The measured values of absorption coefficient include a contribution from scattering which is thought to be at most  $0.1 \text{ cm}^{-1}$  in our crystals. Broadband transmission measurements were made using a Cary 14 spectrophotometer.

### C. GENERAL BACKGROUND AND MODELS

#### 1. Energy Level Model

The energy levels and notation we use for our ensuing discussion are shown in Figure 3-1. We assume that a single species X, which can exist in two valence states ( $X$  and  $X^+$ ), is responsible for the energy states in the  $\text{BaTiO}_3$  bandgap. In the case of iron-doped  $\text{LiNbO}_3$  ( $\text{LiNbO}_3:\text{Fe}$ ),  $X$  corresponds to  $\text{Fe}^{2+}$  and  $X^+$  corresponds to  $\text{Fe}^{3+}$ . We designate the concentration of  $X$  as  $N$ , and the concentration of  $X^+$  as  $N^+$ . Other states, which are optically inactive provide overall charge compensation within the crystal (see Section 3.D). It is important to note that electrons or holes (or both) can contribute to the charge transport in our  $\text{BaTiO}_3$  crystals. For electron transport, state  $X$  is a donor, or "filled" state, and state  $X^+$  is an ionized donor, or "empty" state. For hole transport, state  $X^+$  is an acceptor or "filled" state, and state  $X$  is an ionized acceptor, or "empty" state. We further note that the sign of the space charge field is opposite for the two charge carriers. This changes the direction of beam coupling, and allows a measurement of the dominant photocarrier.

14678~5

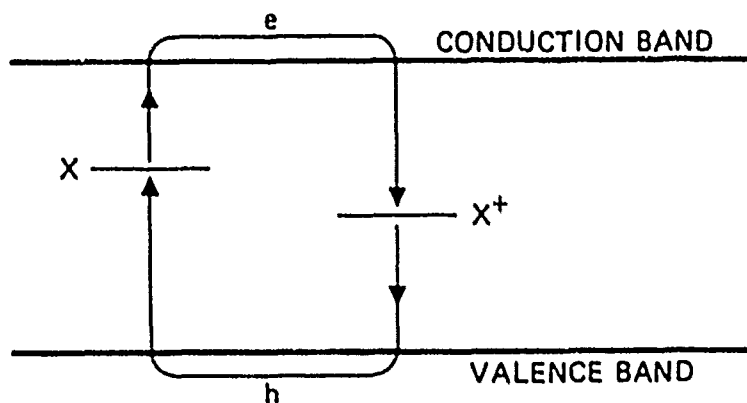


Figure 3-1. Energy level model for the photorefractive effect. Electrons are photoionized from level X and recombine at X<sup>+</sup>; holes are photoionized from X<sup>+</sup> and recombine at X.

In association with the energy level notation given above, we must also define rate coefficients for levels  $X$  and  $X^+$ , and transport coefficients for free electrons and holes. The cross section for photoionization of level  $X$  (thus creating an electron) is  $s_e$ , while the corresponding cross section for level  $X^+$  (thus creating a hole) is  $s_h$ . The mobility for electrons (or holes) is  $\mu_e$  (or  $\mu_h$ ). The recombination rate coefficient for electrons at centers  $X^+$  is  $\gamma_e$ , and the corresponding coefficient for holes at centers  $X$  is  $\gamma_h$ .

## 2. Band Transport Model For Grating Formation

The band transport model<sup>7-10</sup> is commonly used to describe grating formation in a photorefractive material. Under the influence of periodic illumination (see Figure 3-2), electrons (or holes) are optically excited from filled donor (or acceptor) sites to the conduction (or valence) band, where they migrate to dark regions in the crystal by drift or diffusion before recombining into an empty trap. The transported charges result in an ionic space charge grating that is, in general, out of phase with the incident irradiance. The periodic space charge is balanced by a periodic space charge electric field in accordance with Poisson's equation. This space charge field modulates the refractive index through the electro-optic effect. If no electric field is applied to the crystal (as is generally the case in experiments with  $\text{BaTiO}_3$ ), then diffusion alone leads to a phase shift of  $\pi/2$  between the incident irradiance and the space charge field. This shifted grating plays an important role in the beam coupling experiments described later.

A mathematical description of the grating formation process for a single charge carrier was given in its most complete form by Vinetskii, Kukhtarev and co-workers,<sup>7-9</sup> as interpreted and summarized by Valley and Klein.<sup>10</sup> For the case where both charge carriers play an important role, the early work of Staebler and Amodei<sup>11</sup> and Orlowski and Kratzig<sup>12</sup> has been developed and expanded by Klein and Valley,<sup>6,13</sup> leading to complete solutions

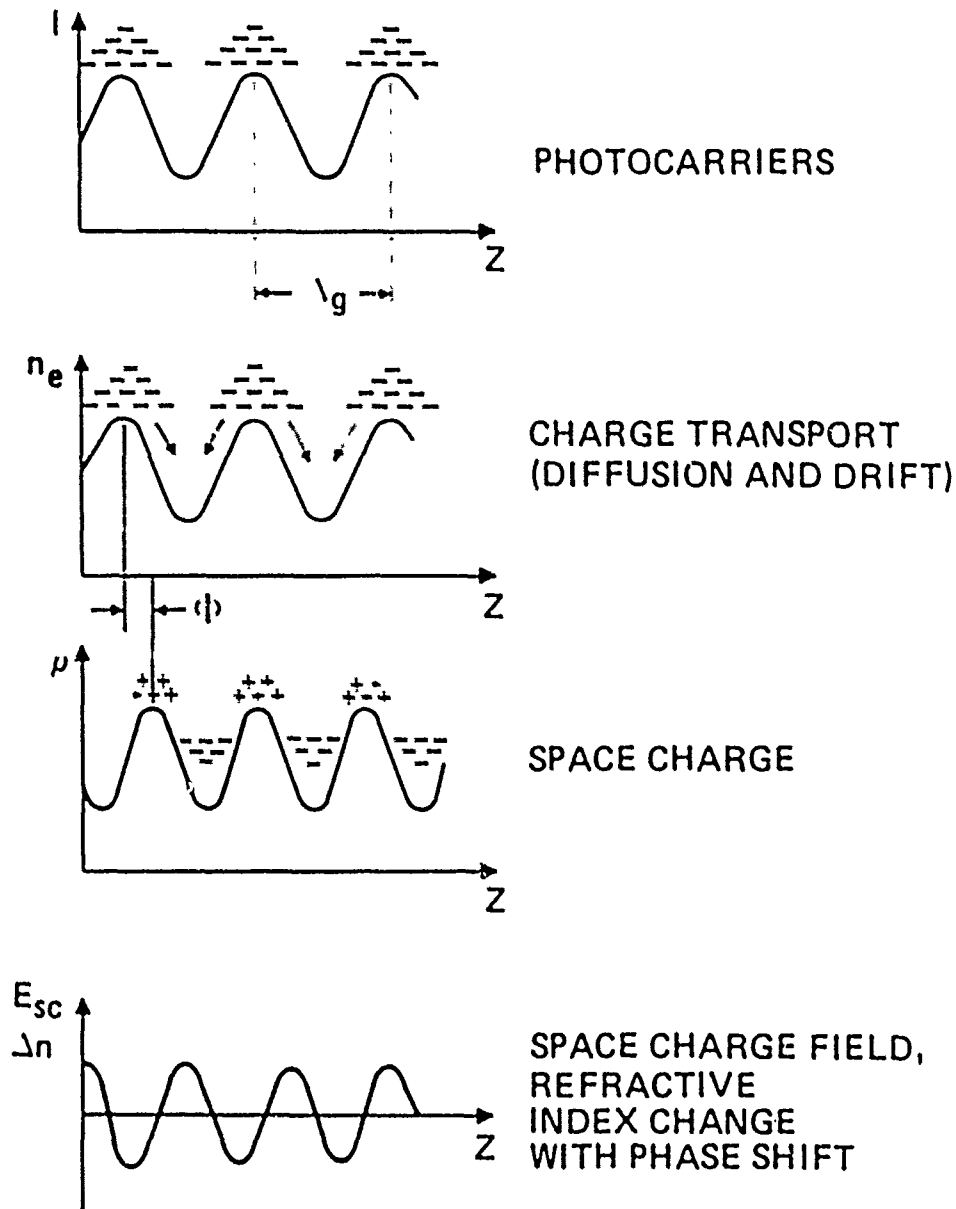


Figure 3-2. Gratings in a photorefractive material. The periodic irradiance pattern results from the interference of two waves in the material.

in the steady state<sup>6</sup> and the transient regime.<sup>13</sup> The key result of the steady-state two-carrier model is that the space charge field (with no applied field and negligible photovoltaic effect) is purely imaginary, and can be written as

$$E_{sc} = \bar{\sigma} \frac{E_d E_q}{E_d + E_q} \quad (1)$$

In Equation (1),  $\bar{\sigma}$  is the normalized differential conductivity, defined by

$$\bar{\sigma} = \frac{\mu_h p - \mu_e n}{\mu_h p + \mu_e n} \quad (2)$$

where  $p$  and  $n$  are the hole and electron concentrations,  $E_d$  is the diffusion electric field, and  $E_q$  is the limiting space charge field. The diffusion field is given by

$$E_d = \frac{kT}{e} \frac{2\pi}{\Lambda_g} \quad (3)$$

The limiting space-charge field is given by

$$E_q = \frac{2e\Lambda_g}{\epsilon} N_E \quad (4)$$

where  $\epsilon$  is the dielectric constant and  $N_E = N^+N/(N+N^+)$  is the effective number of empty traps.

The normalized differential conductivity  $\bar{\sigma}$  defined in Equation (2) accounts for the relative contribution of electrons and holes to the photoconductivity of the sample. When the photoconductivity for holes is dominant,  $\bar{\sigma}=+1$ , whereas  $\bar{\sigma}=-1$  when electron photoconductivity dominates. In a beam coupling experiment, this change in sign corresponds to a change in coupling direction. For the case where the photoconductivity values for the two carriers are equal (and in the absence of an external or photovoltaic field), the net space charge field is zero, and no beam coupling should be observed. For this case,

$$\text{or } p\mu_h = n\mu_e , \quad (5)$$

$$\frac{p}{n} = \frac{\mu_e}{\mu_h} . \quad (6)$$

The free carrier concentrations  $n$  and  $p$  can be related to the trap concentrations  $X$  and  $X^+$  by the rate equations

$$s_e IN = \gamma_e n N^+ \quad (7)$$

and

$$s_h IN^+ = \gamma_h p N . \quad (8)$$

These two equations may be combined to yield

$$\frac{N^+}{N} = \left( \frac{\gamma_h s_e p}{\gamma_e s_h n} \right)^{1/2} . \quad (9)$$

Finally, by combining with Equation (6), we find the condition at the compensation point as

$$\frac{N^+}{N} = \left( \frac{\gamma_h s_e \mu_e}{\gamma_e s_h \mu_h} \right)^{1/2} . \quad (10)$$

The relative importance of electrons and holes to the photorefractive effect in iron-doped  $\text{LiNbO}_3$  has been studied by Orlowski and Kratzig.<sup>12</sup> The beam coupling gain was measured in a variety of samples heat treated (reduced or oxidized) to vary the ratio  $N^+/N$ , or in their case,  $[\text{Fe}^{3+}]/[\text{Fe}^{2+}]$ . Their results are summarized in Figure 3-3. The actual parameters plotted are the normalized electron and hole conductivities defined by

$$\bar{\sigma}_e = \frac{\sigma_e}{\sigma_e + \sigma_h} \quad (11)$$

and

$$\bar{\sigma}_h = \frac{\sigma_h}{\sigma_e + \sigma_h} , \quad (12)$$

where  $\sigma_e = ne\mu_e$  and  $\sigma_h = pe\mu_h$ . We see from Figure 3-3 that in strongly oxidized samples ( $[\text{Fe}^{3+}] \gg [\text{Fe}^{2+}]$ ), holes dominate the photoconductivity. In reduced samples ( $[\text{Fe}^{2+}] \geq [\text{Fe}^{3+}]$ ), electrons

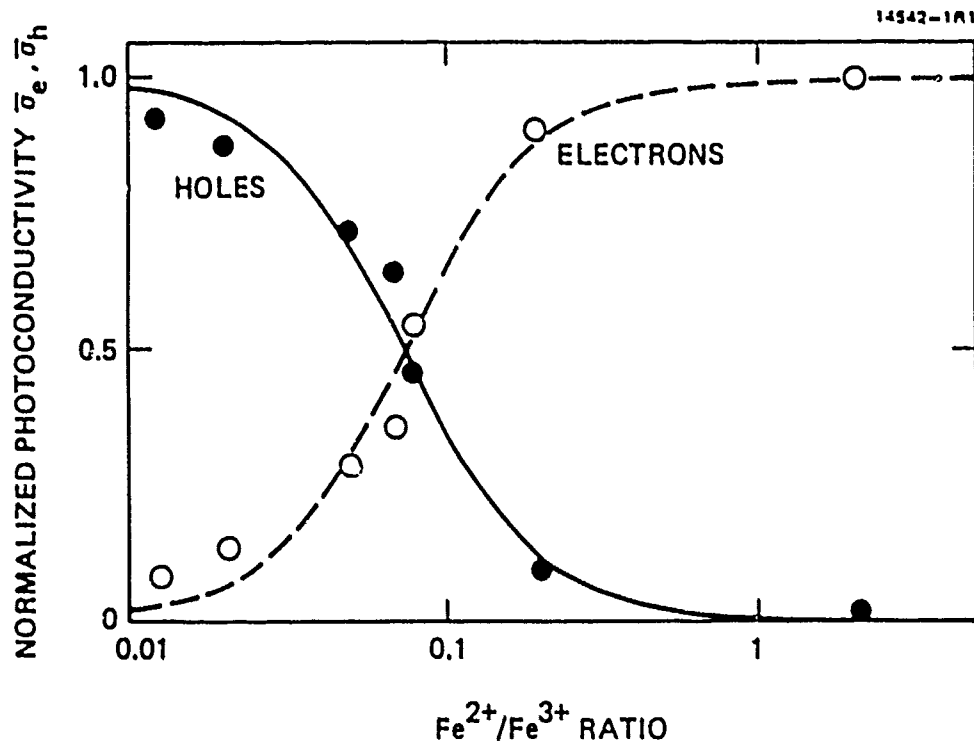


Figure 3-3. Relative contribution of electrons and holes to the photoconductivity in  $\text{LiNbO}_3$  (from Reference 10).

Note: Reference 10 - M. B. Klein is the author and principal investigator from Hughes Research Laboratories.

are the dominant photoconductor. These two limits correspond to different directions of energy exchange in the beam coupling experiments of Reference 12. Note that the crossover (or compensation) point occurs for  $[\text{Fe}^{3+}] \approx 20[\text{Fe}^{2+}]$ . This indicates that  $\gamma_h s_e \mu_e \approx 400 \gamma_e s_h \mu_h$  in  $\text{LiNbO}_3$  [see Equation (10)].

### 3. Photorefractive Centers in $\text{BaTiO}_3$

The  $\text{BaTiO}_3$  structure is based on groupings of oxygen octahedra linked at their corners. In a perfect crystal, the center of each octahedron contains a  $\text{Ti}^{4+}$  ion, while the  $\text{Ba}^{2+}$  ions lie in the regions outside the octahedra. As discussed later, most of the features of the band structure of  $\text{BaTiO}_3$  are determined by the properties of the basic  $\text{TiO}_6^{8-}$  octahedron or cluster.

There are two major types of defects in crystalline  $\text{BaTiO}_3$  which could lead to deep levels in the band gap and donor/acceptor behavior: vacancies or impurities. It is always expected that impurities will be present in the 10 to 100 ppm range, unless extraordinary precautions are taken in purifying starting materials and controlling the growth environment. Vacancies are also commonly present, if only to compensate for the charge imbalance introduced by the impurities.

Of the three elements which make up the  $\text{BaTiO}_3$  structure, the most volatile is oxygen. During crystal growth or processing at high temperatures, this species is the most likely to evaporate, thus creating oxygen vacancies, denoted as  $V_O$ . Since the oxygen ion in the  $\text{BaTiO}_3$  lattice has a charge  $\text{O}^{2-}$ , an oxygen vacancy has a charge  $V_O^{2+}$ . Thus, an oxygen vacancy can trap one or two electrons, leading to donor levels in the  $\text{BaTiO}_3$  bandgap. Such states cannot participate in the photorefractive effect for two reasons:

(i) The donor levels represented by oxygen vacancies filled with one or two electrons are relatively shallow,<sup>14,15,24</sup> and are thus likely to be thermally ionized at room temperature.

(ii) Existing evidence in the literature<sup>16,17</sup> and our own measurements indicate that the dominant photocarriers in as-grown



samples are holes, in contradiction with the donor character of the filled oxygen vacancies.

We now wish to consider the possible impurities in  $\text{BaTiO}_3$  and their relation to the photorefractive effect. Previous measurements<sup>18,19</sup> and our own studies show three major groups of impurities in  $\text{BaTiO}_3$ : (1) calcium and strontium, (2) aluminum and silicon, and (3) transition metals. Calcium and strontium are in the same family of the periodic table as barium. They almost always occur with barium in nature, and are difficult to separate from it. Since calcium and strontium are isovalent with barium and substitute for barium in the  $\text{BaTiO}_3$  lattice, they do not introduce any levels in the  $\text{BaTiO}_3$  bandgap, and thus cannot participate in the photorefractive effect.

The sources of aluminum and silicon impurities are the furnace walls and heating elements. However, aluminum and silicon possess only one stable valence state ( $\text{Al}^{3+}$  and  $\text{Si}^{4+}$ ), and thus these elements can not support the intervalence transfer  $X \rightleftharpoons X^+$  which is a key requirement of the photorefractive effect.

Transition metal impurities are ubiquitous in many oxide crystals, because of their abundance in nature, their chemical similarity to constituents of the compound in question (e.g., Ti in  $\text{BaTiO}_3$ ), and possible contamination of starting powders from handling with metal utensils. The six first row transition metals are Cr, Co, Ni, Mn, Fe and Cu, and they are all likely to be present at levels as high as 50 ppm in  $\text{BaTiO}_3$ . Fe is the most abundant of the transition metals, and could be expected at still higher concentrations. It is believed that transition metal impurity ions (as well as  $\text{Al}^{3+}$  and  $\text{Si}^{4+}$ ) substitute for  $\text{Ti}^{4+}$  in the  $\text{BaTiO}_3$  lattice, due to the close match between their ionic radius and that of  $\text{Ti}^{4+}$ . In the case of Fe impurities in  $\text{BaTiO}_3$ , this has been proven in a number of separate studies.<sup>19,20</sup> Due to the low binding energies of their 3d electrons, each of the transition metals can exist in several valence states, ranging typically between +1 and +4 (see Table 3-4).

#### 4. Charge Balance and Conductivity in BaTiO<sub>3</sub>

When an impurity ion (with valence +3 or less) substitutes for Ti<sup>4+</sup> in BaTiO<sub>3</sub>, a charge imbalance is created. In the simplest case, the compensation for this imbalance is achieved through the creation of oxygen vacancies:

$$[M^{3+}] = 2[V_O^{2+}]_I \quad , \quad (13)$$

where  $M^{3+}$  is a trivalent metal ion and  $[V_O^{2+}]_I$  is the impurity-related concentration of oxygen vacancies. Note that the charge of the metal ion is expressed in relation to the isolated metal atom; the charge in the crystal is -1. The oxygen vacancy concentration is also influenced by the growth or processing environment of the crystal. At a given temperature there may be an excess or a deficiency of oxygen, compared with the amount required to produce  $[V_O^{2+}]_I$ . In either of these limits, free carriers are produced to maintain the charge balance:

$$[M^{3+}] + n = 2[V_O^{2+}] + p \quad . \quad (14)$$

The growth environment of commercial BaTiO<sub>3</sub> (grown by the top-seeded solution growth technique)<sup>21</sup> is oxidizing (i.e., there is excess oxygen), leading to a reduction in the number of vacancies below the value  $[V_O^{2+}]_I$ , and the creation of free holes. Thus, in as-grown crystals the transition metals are generally acceptor impurities, and the samples are p-type in the dark.<sup>22-25</sup>

Conversely, samples processed at low oxygen partial pressures require the production of free electrons for charge balance, and are thus n-type in the dark.<sup>22 to 25</sup>

In considering charge balance we must also account for the fact that the transition metals (say Fe) can change valence state, while other metal impurities (say Al) can not. We may thus write

$$[Al^{3+}] + 2[Fe^{2+}] + [Fe^{3+}] + n = 2[V_O^{2+}] + p \quad . \quad (15)$$

The presence of several valence states in the transition metals allows the charge balance to be maintained over a range of oxygen partial pressures without the creation of large numbers of free carriers. In this pressure range the major impact is the variation of the relative amounts of  $\text{Fe}^{2+}$  and  $\text{Fe}^{3+}$ , due to changes in  $[\text{V}_\text{O}^{2+}]$ . In p-type samples, the free carrier concentration at room temperature is further reduced by trapping into acceptor levels, since these levels are thought to lie deep in the bandgap.<sup>22,26</sup> This leads to high resistivity values in samples grown or processed in air. By contrast, reduced samples of  $\text{BaTiO}_3$  can be semiconducting (n-type) even at room temperature,<sup>22,27,28</sup> since the induced donor levels are more shallow.<sup>22,26</sup>

The charge balance condition given in Equation (15) is sufficient to describe the dark conductivity in  $\text{BaTiO}_3$  over a wide range of oxygen partial pressures. At very high oxygen pressures, Ba vacancies become important. At very low pressures, reduction of the Ti ions from  $\text{Ti}^{4+}$  to  $\text{Ti}^{3+}$  must be considered.

In addition to isolated metal impurities and fully ionized oxygen vacancies indicated in Equation (15), we must also consider the possibility that association of ionic defects or trapping of free charges may lead to new species. Two specific cases must be considered. First, at high temperatures during crystal growth or processing, oxygen vacancies can associate with metal ions, due to coulomb attraction. Assuming that this association occurs among nearest neighbors, the resulting structure in  $\text{BaTiO}_3$  would be a  $(\text{M}^{n+}\text{O}_5)^{n-10}$  cluster. This complex is called a  $\text{M}^{n+}\text{-V}_\text{O}$  center. Such centers are known to exist in perovskites, but no consensus exists as to their importance. The concentration of these centers in our samples can be determined by EPR. According to our EPR measurements of  $\text{Fe}^{3+}$  (to be described later), the population of  $\text{Fe}^{3+}\text{-V}_\text{O}$  centers is much less than that of isolated  $\text{Fe}^{3+}$ .

A second possible form of association is the trapping of one or two free electrons at oxygen vacancies. As indicated earlier,

the resultant states are thought to be quite shallow,<sup>14,15</sup> and are thus only likely to be populated significantly at low temperatures.

#### D. EXPERIMENTAL RESULTS

On the basis of the discussion given above, we anticipated that the six first-row transition metals would be the most likely candidates for the photorefractive species in BaTiO<sub>3</sub>. The purpose of our measurements was to identify and characterize the actual photorefractive species in our samples. Our basic approach was to measure impurity concentrations in a number of samples, and correlate these data with separate concentration measurements of the filled and empty levels participating in the photorefractive effect.

##### 1. Beam Coupling Measurements at 442 nm

Steady-state beam coupling is a convenient technique for measuring several important parameters in a photorefractive crystal. We have measured the amplitude and sign of the beam coupling gain as a function of grating period in nine samples. From the sense of the beam coupling (i.e., the sign of the gain coefficient), we can determine the sign of the dominant photocarrier.<sup>11,12,16</sup> By fitting a theoretical expression to the data of gain versus grating period, we can determine two independent parameters.<sup>5</sup> The first is the effective electro-optic coefficient

$$r_{\text{eff}} = F_p \bar{\sigma} r_{13} \quad , \quad (16)$$

where  $F_p$  is the fractional poling,  $\bar{\sigma}$  is the normalized differential conductivity [defined in Equation (2)], and  $r_{13}$  is the electro-optic tensor component for the experimental geometry, in a perfectly poled sample. The second experimental parameter is the effective number of empty traps  $N_E = NN^+ / (N + N^+)$  [see Equation (4)].

Of the nine samples we studied, the data for seven gave a very good fit to the theoretical expression for gain versus grating period.<sup>6</sup> Of the remaining two crystals, one (GB5) had an anomalously small gain which changed sign with grating period; we attribute this behavior to a nearly perfect compensation condition ( $\mu_n \approx \mu_p$ ), leading to a weaker effect of unknown origin.<sup>6</sup> In the other anomalous crystal (BW1), the magnitude of the gain was normal, but the functional variation with grating period was not in accordance with our model. We attribute this behavior to the presence of a second photorefractive species which our EPR measurements suggest is Cu.

In Table 3-1 we present our measured values of the sign of the dominant photocarrier, the effective number of empty traps ( $N_E$ ), the effective electro-optic coefficient ( $r_{eff}$ ), and  $F_p \bar{\sigma} = r_{eff}/r_{13}$  for the seven crystals which follow our model. Our measured values of  $N_E$  given in Table 3-1 are in the range  $2-9 \times 10^{16} \text{ cm}^{-3}$ , and are consistent with values for other BaTiO<sub>3</sub> crystals, as reported in the literature.<sup>16,17,29</sup> We will show later that  $N \ll N^+$  in our crystals, thus yielding  $N_E \approx N$ , the number of empty acceptor states. In our beam coupling measurements we are not able to determine separately the fractional poling  $F_p$  and the normalized differential conductivity  $\bar{\sigma}$ . However, etching experiments on several of our crystals show relatively few 180° domains in our samples,<sup>30</sup> leading us to estimate that  $F \approx 0.9$ ; thus, the dominant contribution to  $F\bar{\sigma}$  comes from  $\bar{\sigma}$ .

## 2. Optical Absorption Coefficient Measurements

The optical absorption coefficient  $\alpha$  can be written as

$$\alpha = \alpha_p + \alpha_{NP} , \quad (17)$$

where  $\alpha_p$  is the photorefractive contribution, and  $\alpha_{NP}$  is the non-photorefractive contribution (typically assumed to be proportional to  $\alpha_p$ ). In general,  $\alpha_p$  must account for the photoexcitation of both electrons and holes. Since holes are the

Table 3-1. Beam coupling data for seven samples of BaTiO<sub>3</sub>

14542-11M3

CRYSTAL	SIGN OF DOMINANT PHOTOCARRIER	EFF. NO. OF EMPTY TRAPS $N_E \text{ cm}^{-3}$	EFFECTIVE E-O COEFFICIENT $r_{\text{eff}} (\text{pm/V})$	$F\bar{\sigma} = r_{\text{eff}}/r_{13}$
G/L	$\div$	$4.4 \times 10^{16}$	7.3	0.30
R1	+	8.1	9.5	0.40
R2	-	2.8	-7.9	-0.33
G83	+	6.1	9.7	0.41
G84	+	3.0	4.2	0.18
K2	+	8.7	12.0	0.50
SC	+	4.2	8.3	0.35

dominant photoconductors in our samples, we may write  $\alpha_p = N^+ s_h$ , or  $\alpha = N^+ s_h / \phi$ , where  $\phi$  is the quantum efficiency. Thus, the measurement of  $\alpha$  in a number of crystals should provide a relative measurement of  $N^+$ , the number of filled (acceptor) states, provided that the quantum efficiency is constant.

Shown in Figure 3-4 are the measured absorption coefficients as a function of wavelength for four different BaTiO<sub>3</sub> crystals (R1, GB3, G/L, and R2). The results of the laser transmission experiments are indicated by the discrete points in Figure 3-4, whereas the solid curves through the points were obtained using the Cary 14 spectrophotometer.

Note from Figure 3-4 that the absorption coefficient is anisotropic, as expected from the uniaxial symmetry of BaTiO<sub>3</sub> at room temperature. Note also that three of the four crystals show a broad, featureless "tail" extending from the fundamental absorption edge near 3500 Å. One sample (GB3) does show a more prominent peak at 5000 Å, leading us to suspect a different impurity content than the other crystals. This is borne out by our impurity weight measurements to be described later, which show a very large bismuth concentration. Crystal R2 is also anomalous in the sense that the absorption anisotropy is reversed in sign from the other crystals. This effect may be related to the electron photoconductivity in this crystal. In Table 3-2 we present the value of  $\alpha$  at 4416 Å for eight samples (with  $\vec{E} \parallel \vec{c}$ ), in order to allow a relative determination of the density of filled traps.

### 3. Impurity Identity and Concentrations

Secondary ion mass spectroscopy (SIMS) was used to determine the impurities in two different crystalline BaTiO<sub>3</sub> samples. These measurements, while only qualitative, give a sensitive indication of all impurities. The elements observed were H, Li, Na, K, C, Al, Si, Ca, Sr, Ni, Mn, Cr and Fe. Of the elements listed, the first seven do not exist commonly in more than one valence state, and thus can not support the inter-valence transfer

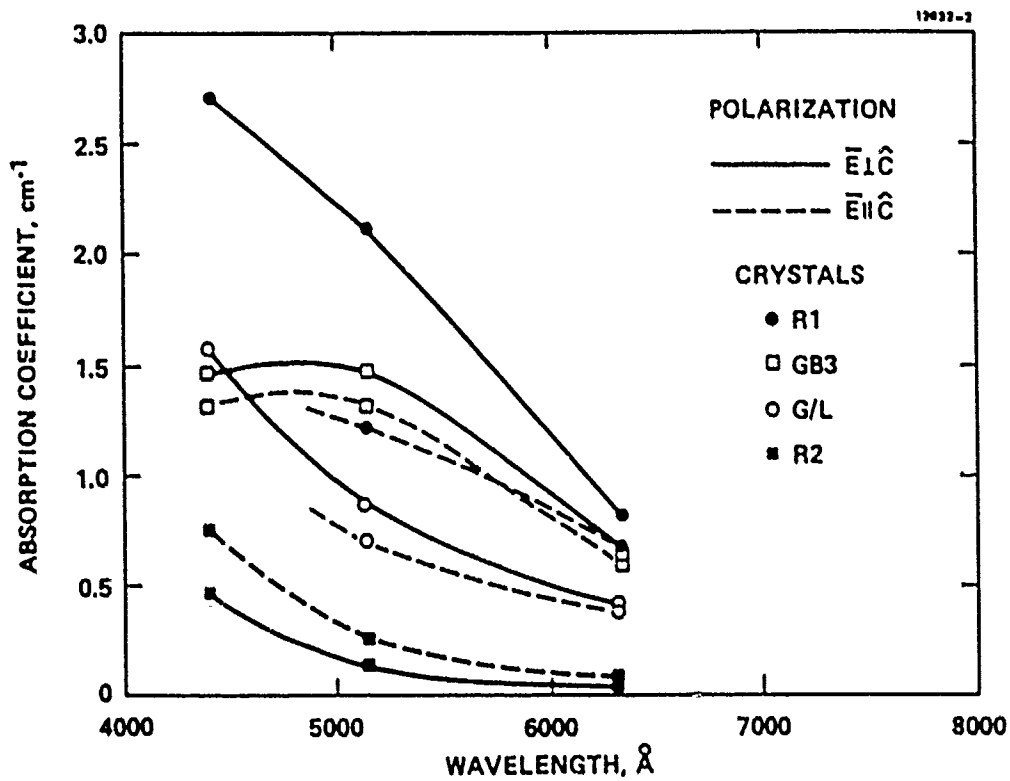


Figure 3-4. Spectral variation of the absorption coefficient in the visible for four  $\text{BaTiO}_3$  samples.



Table 3-2. Absorption coefficient at 4416 Å for  $\vec{E} \parallel \vec{c}$

15462-4

CRYSTAL	ABSORPTION COEFFICIENT $\alpha$ ( $\text{cm}^{-1}$ )
G/L	1.6
R1	2.7
R2	0.5
GB3	1.5
GB4	0.6
K2	1.8
BW1	3.5
1334	2.4

required for the photorefractive species. Ca and Sr substitute readily for Ba in the  $\text{BaTiO}_3$  structure; however they are isovalent with Ba, and thus produce no energy level in the  $\text{BaTiO}_3$  band gap. The remaining species are transition metals and must be considered as candidate photorefractive species.

On the basis of the SIMS measurements six different crystals (R1,R2,G/L,GB3,1334 and BW1) were analyzed for impurities by spark emission spectroscopy. A semiquantitative determination of all metals was carried out, along with a quantitative measurement of transition metals. All samples contained Al and Si at concentration levels in the 50 to 500 ppm range. As indicated above, these species are not expected to participate in the photorefractive effect. The concentration results for the transition metals are given in Table 3-3. We see that iron is consistently the most abundant impurity, and the only element occurring consistently at concentrations greater than 50 ppm. The predominance of Fe impurities has previously been noted in  $\text{BaTiO}_3$  (Reference 18),  $\text{SrTiO}_3$  (Reference 31), and  $\text{LiNbO}_3$ .<sup>2</sup> Note the very large bismuth content in crystal GB3; this is likely the source of the unusual absorption behavior of this sample. We will comment further on this sample in our later discussion.

#### 4. EPR Measurements in Tetragonal $\text{BaTiO}_3$

EPR spectroscopy is a powerful technique for determining the presence and concentration of a variety of paramagnetic point defects and impurities.<sup>32</sup> Furthermore, in the case of impurities, EPR can be used to identify the valence state. The disadvantage of EPR is that it is not equally sensitive to impurities in all possible valence states. This is shown clearly with reference to Table 3-4, which presents the EPR properties of the six candidate transition metals in all relevant valence states. The natural abundance of the odd isotopes of each species are presented, because these isotopes lead to hyperfine structure in their EPR spectra, which are readily identified. The parameter of particular interest is the room temperature

Table 3-3. Transition metal impurities in BaTiO<sub>3</sub>,  
measured by spark source emission  
spectroscopy

15462-5

SAMPLE	CONCENTRATION (ppm)				
	Fe	Cu	Mn	Ni	OTHER
G/L	120		< 50	< 20	Bi (0.5 - 5%)
R1	147		< 50		
R2	72		< 50	< 20	
GB3	55	< 50			
BW1	51	< 50			
1334	138		< 50	< 20	

FOR Fe, 100 ppm  $\approx 5 \times 10^{18} \text{ cm}^{-3}$

Table 3-4. Electronic properties of first-row transition metals. For each element, we have indicated the most stable valence state

11-413-1

ELEMENT	VALENCE STATE	ELECTRON CONFIGURATION	GROUND STATE FREE ION	SPIN DEGENERACY	DISTRIBUTION OF d ELECTRONS IN $t_{2g}/e_g$ ORBITALS. $2g/e_g$ OCTAHEDRAL SYMMETRY	ROOM TEMPERATURE SPIN LATTICE RELAXATION TIME
Cr (Cr <sup>53</sup> $I = 3/2$ ) 95.5%	+2	d <sup>4</sup>	<sup>5</sup> D <sub>0</sub>	2	$\begin{smallmatrix} 3 \\ t_{2g} \end{smallmatrix} \begin{smallmatrix} 1 \\ e_g \end{smallmatrix}$	Long
	$\boxed{+2}$	d <sup>3</sup>	<sup>4</sup> F <sub>3/2</sub>	3/2	$\begin{smallmatrix} 3 \\ t_{2g} \end{smallmatrix}$	Long
	+4	d <sup>2</sup>	<sup>3</sup> F <sub>2</sub>	1	$\begin{smallmatrix} 2 \\ t_{2g} \end{smallmatrix}$	Short
Mn (Mn <sup>55</sup> $I = 5/2$ ) 100%	$\boxed{+2}$	d <sup>5</sup>	<sup>6</sup> S <sub>5/2</sub>	5/2	$\begin{smallmatrix} 3 \\ t_{2g} \end{smallmatrix} \begin{smallmatrix} 2 \\ e_g \end{smallmatrix}$	Long
	+3	d <sup>4</sup>	<sup>5</sup> D <sub>0</sub>	2	$\begin{smallmatrix} 3 \\ t_{2g} \end{smallmatrix} \begin{smallmatrix} 1 \\ e_g \end{smallmatrix}$	Long
	+4	d <sup>3</sup>	<sup>4</sup> F <sub>3/2</sub>	3/2	$\begin{smallmatrix} 3 \\ t_{2g} \end{smallmatrix}$	Long
Fe (Fe <sup>57</sup> $I = 1/2$ ) 2.19%	+1	d <sup>7</sup>	<sup>4</sup> F <sub>9/2</sub>	3/2	$\begin{smallmatrix} 5 \\ t_{2g} \end{smallmatrix} \begin{smallmatrix} 2 \\ e_g \end{smallmatrix}$	Short
	+2	d <sup>6</sup>	<sup>5</sup> D <sub>4</sub>	2	$\begin{smallmatrix} 4 \\ t_{2g} \end{smallmatrix} \begin{smallmatrix} 2 \\ e_g \end{smallmatrix}$	Short
	$\boxed{+2}$	d <sup>5</sup>	<sup>6</sup> S <sub>5/2</sub>	5/2	$\begin{smallmatrix} 3 \\ t_{2g} \end{smallmatrix} \begin{smallmatrix} 2 \\ e_g \end{smallmatrix}$	Long
Co (Co <sup>59</sup> $I = 7/2$ ) 100%	+1	d <sup>8</sup>	<sup>3</sup> F <sub>4</sub>	1	$\begin{smallmatrix} 6 \\ t_{2g} \end{smallmatrix} \begin{smallmatrix} 2 \\ e_g \end{smallmatrix}$	Long
	$\boxed{+2}$	d <sup>7</sup>	<sup>4</sup> F <sub>9/2</sub>	3/2	$\begin{smallmatrix} 5 \\ t_{2g} \end{smallmatrix} \begin{smallmatrix} 2 \\ e_g \end{smallmatrix}$	Short
	+3	d <sup>6</sup>	<sup>5</sup> D <sub>4</sub>	2	$\begin{smallmatrix} 4 \\ t_{2g} \end{smallmatrix} \begin{smallmatrix} 2 \\ e_g \end{smallmatrix}$	Long
Ni (Ni <sup>61</sup> $I = 3/2$ ) 1.19%	+1	d <sup>9</sup>	<sup>2</sup> D <sub>5/2</sub>	1/2	$\begin{smallmatrix} 6 \\ t_{2g} \end{smallmatrix} \begin{smallmatrix} 3 \\ e_g \end{smallmatrix}$	Long
	$\boxed{+2}$	d <sup>8</sup>	<sup>3</sup> F <sub>4</sub>	1	$\begin{smallmatrix} 6 \\ t_{2g} \end{smallmatrix} \begin{smallmatrix} 2 \\ e_g \end{smallmatrix}$	Long
	+3	d <sup>7</sup>	<sup>4</sup> F <sub>9/2</sub>	3/2	$\begin{smallmatrix} 5 \\ t_{2g} \end{smallmatrix} \begin{smallmatrix} 2 \\ e_g \end{smallmatrix}$	Short
Cu (Cu <sup>63</sup> $I = 3/2$ ) 69.09% (Cu <sup>65</sup> $I = 3/2$ ) 30.91%	$\boxed{+1}$	d <sup>10</sup>	<sup>1</sup> S <sub>0</sub>	0	$\begin{smallmatrix} 6 \\ t_{2g} \end{smallmatrix} \begin{smallmatrix} 4 \\ e_g \end{smallmatrix}$	(NOT PARAMAGNETIC)
	+2	d <sup>9</sup>	<sup>2</sup> D <sub>5/2</sub>	1/2	$\begin{smallmatrix} 6 \\ t_{2g} \end{smallmatrix} \begin{smallmatrix} 3 \\ e_g \end{smallmatrix}$	Long
	+3	d <sup>8</sup>	<sup>3</sup> F <sub>4</sub>	1	$\begin{smallmatrix} 6 \\ t_{2g} \end{smallmatrix} \begin{smallmatrix} 2 \\ e_g \end{smallmatrix}$	Long

spin-lattice relaxation time. In our  $\text{BaTiO}_3$  experiments we are limited to measurements at room temperature, due to the tetragonal-orthorhombic phase transition at  $\sim 5^\circ\text{C}$ . Thus, only those species with long spin-lattice relaxation times (and thus negligible line broadening) can be observed. Furthermore in the case of  $\text{Cu}^{1+}$ , no EPR spectrum can be observed, since there are no unpaired spins. For each metal ion in Table 3-4, we have indicated the valence state which is most stable, and most likely to be present in our samples. Each of these species should be readily observable by EPR at room temperature, except for  $\text{Co}^{2+}$ . Note, however, that Co is the least abundant of the candidate transition metals.

We have measured EPR spectra in four different crystals of  $\text{BaTiO}_3$  in the ferroelectric tetragonal phase. Shown in Figures 3-5 and 3-6 are representative spectra from crystal R2. The spectra were taken with the dc magnetic field directed along the  $[010]$  axis  $[\vec{B} \parallel \vec{c}$  and in the  $(100)$  plane]. The spectrum shown in Figure 3-5 exhibits five intense resonances which is characteristic of a  ${}^6\text{S}_{5/2}$  magnetic ion ( $\text{Fe}^{3+}$ ) in a non-cubic electrostatic crystalline field.<sup>33</sup> One of the unique features of this spectrum as well as spectra at other angles is the sharpness of the lines. This feature not only reflects the high microscopic quality of the crystal (i.e., reduced number of structural imperfections and reduced strain) but in addition, indicates that the sample is relatively free of  $90^\circ$  domains. Shown in Figure 3-6 is an expanded spectrum about the  $g \approx 2$  spectral region at the same magnetic field orientation. Indicated in this figure are resonance transitions which we have assigned to the even isotopes ( $I=0$ ) 50, 52 and 54 and the odd isotope 53 ( $I=3/2$ , 9.55% abundance) of  $\text{Cr}^{3+}$ .

Also shown in Figure 3-6 are lines which we assign to  ${}^{55}\text{Mn}$  ( $I=5/2$ ). This assignment is based on the fact that the six-line multiplets are due to the hyperfine interaction of the 3d electrons of manganese with the  $I=5/2$   ${}^{55}\text{Mn}$  nucleus (100% abundance), with hyperfine constant  $A_{\perp} \approx 0.0080 \text{ cm}^{-1}$  ( $A_{\perp} \approx A_{||}$ ).

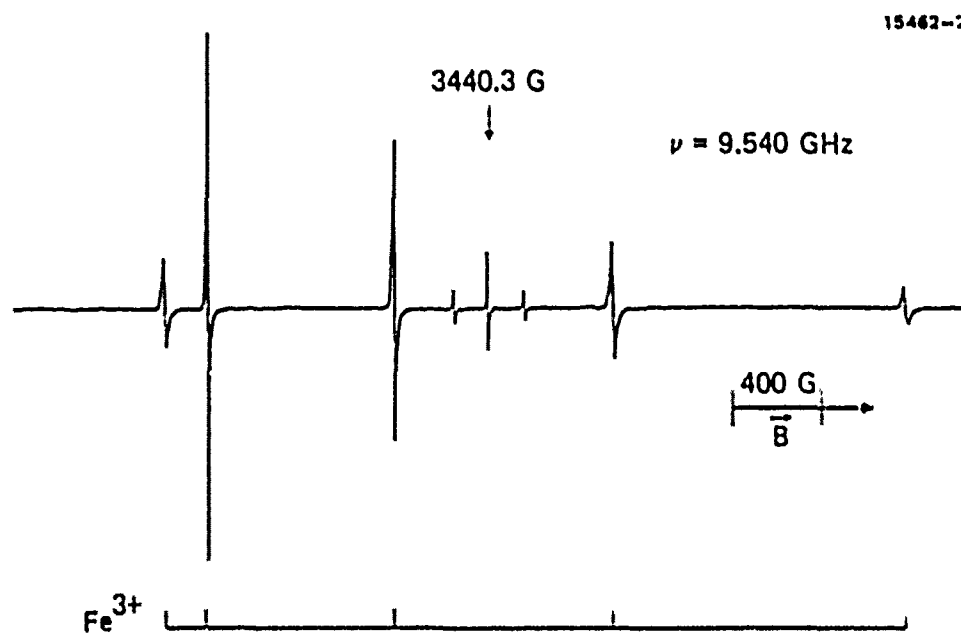


Figure 3-5. EPR spectrum observed with the DC magnetic field directed along the [010] axis ( $\vec{B} \parallel \hat{c}$  and in the (100) plane).

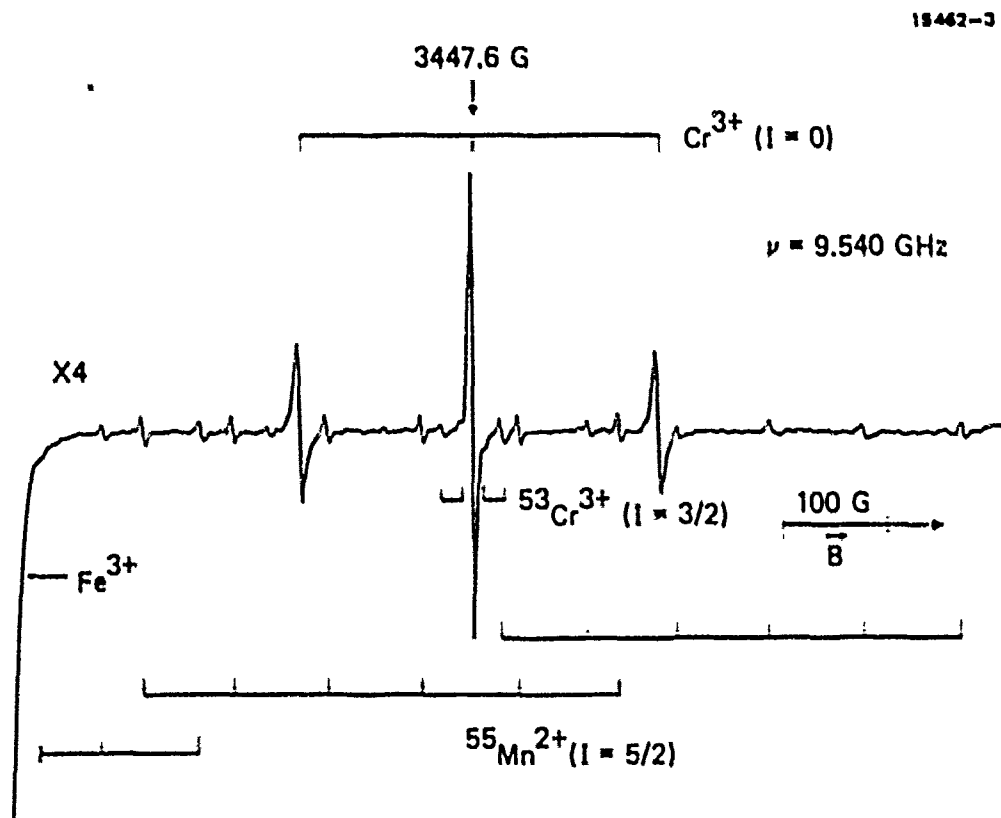


Figure 3-6. Expanded EPR spectrum about the  $g \approx 2$  spectral region at the same magnetic field orientation as in Figure 3-5.

This value for  $A_1$  is consistent with manganese in the  $2^+$  valence state as reported by other workers.<sup>34,35</sup> The possibility that the observed multiplets are due to manganese in the  $+4$  valence state may be discarded because the EPR of  $Mn^{4+}$  can not be seen at room temperature in  $BaTiO_3$ .<sup>14,36</sup>

The concentration of  $Fe^{3+}$  in several different  $BaTiO_3$  crystals was determined by EPR and the results are presented in Table 3-5. By comparison, our measurements indicate that the concentrations of  $Cr^{3+}$  and  $Mn^{2+}$  are at least two orders of magnitude lower than that of  $Fe^{3+}$ . In one crystal (BW1) we detected  $Cu^{2+}$  at a concentration level approximately 30% of the  $Fe^{3+}$  spin concentration. This is consistent with the anomalous beam coupling performance of this crystal, as described in Section D-1. No signals were observed in any of our samples from singly ionized oxygen vacancies.

We have studied in most detail the angular dependence of the EPR spectra of crystal R2. From the angular behavior in the plane perpendicular to the polar axis  $\hat{c}$  of the five major transitions of the  $Fe^{3+}$  ion and the three strong resonances of the  $Cr^{3+}$ , it was established that the sites containing the paramagnetic species have a four-fold axis of symmetry ( $C_{4v}$ ). The spin Hamiltonian which describes the energy levels of the  $^6S_{5/2} Fe^{3+}$  in a crystalline field with a four-fold axis of symmetry and an external magnetic field  $\vec{B}$  has the following form:<sup>30</sup>

$$H = \beta(\vec{S} \cdot \vec{g} \cdot \vec{B}) + B_4(O_4^0 + 5O_4^4) + B_2^0 O_2^0 + B_4^0 O_4^0. \quad (18)$$

Here the spin operators  $O_k^q$  are given by their standard expressions<sup>32</sup>

$$\begin{aligned} O_2^0 &= \{3S_z^2 - S(S+1)\} \\ O_4^0 &= \{35S_z^4 - 30S(S+1)S_z^2 + 25S_z^2 - 6S(S+1)\} \\ O_4^4 &= \left\{\frac{1}{2} (S_+^4 + S_-^4)\right\}, \end{aligned} \quad (19)$$



Table 3-5.  $\text{Fe}^{3+}$  concentration measured by EPR

15462-4

SAMPLE	$\text{Fe}^{3+}$ CONCENTRATION ( $10^{18} \text{ cm}^{-3}$ )
G/L	2.0
R2	1.9
8WI	4.7
1334	5.6

where the  $S_i$  are spin angular momentum operators and the B coefficients are related to the cubic (a,F) and zero-field (D) parameters by:

$$a = 120 B_4, D = 3B_2^0, F = 180 B_4^0.$$

For  $\text{Cr}^{3+}(^4F_{3/2})$  only the first and the third terms in the spin Hamiltonian (Equation 18) are required to describe the energy levels resulting from the splitting of the combined effect of the crystalline field and the dc magnetic field.<sup>32</sup>

Shown in Figure 3-7 are plots of the angular variation of the EPR transitions for the  $\text{Fe}^{3+}$  and  $\text{Cr}^{3+}$  when  $\vec{B}$  is varied in the (100) plane.<sup>33</sup> In the case of  $\text{Fe}^{3+}$  the broken lines through discrete points, which aid in following the angular variation, do not follow a simple  $[3(g_{||}^2/g^2)\cos^2\phi-1]$  law. This is expected since the Zeeman energy is not much larger than the electronic quadrupole energy (i.e.,  $g\beta B > D$ ). From a preliminary analysis we find that  $D \approx 0.09 \text{ cm}^{-1}$  which is in agreement with that reported by earlier workers.<sup>33</sup> The angular variation for the  $\text{Cr}^{3+}$  transitions, on the other hand, is accurately described by a simple  $[3(g_{||}^2/g^2)\cos^2\phi-1]$  dependence from which we find that

$$g_{||} = 1.9740 \pm 0.0002,$$

$$g_{\perp} = 1.9774 \pm 0.0002,$$

and

$$|D| = 0.0150 \pm 0.0001 \text{ cm}^{-1}.$$

The nature of the local site giving rise to the EPR spectrum of  $\text{Fe}^{3+}$  with  $C_{4v}$  symmetry in tetragonal  $\text{BaTiO}_3$  is assumed to be associated with a tetragonally distorted  $\text{FeO}_6$  cluster. Our reasoning is based on the fact that if the local  $C_{4v}$  paramagnetic site was due to local compensation at a nearest-neighbor oxygen site, i.e.,  $\text{FeO}_5$  cluster ( $\text{Fe}^{3+}-V_O$ ), then it is expected that the EPR spectrum would be best described by  $D \gg g\beta B$ .<sup>37</sup> In this

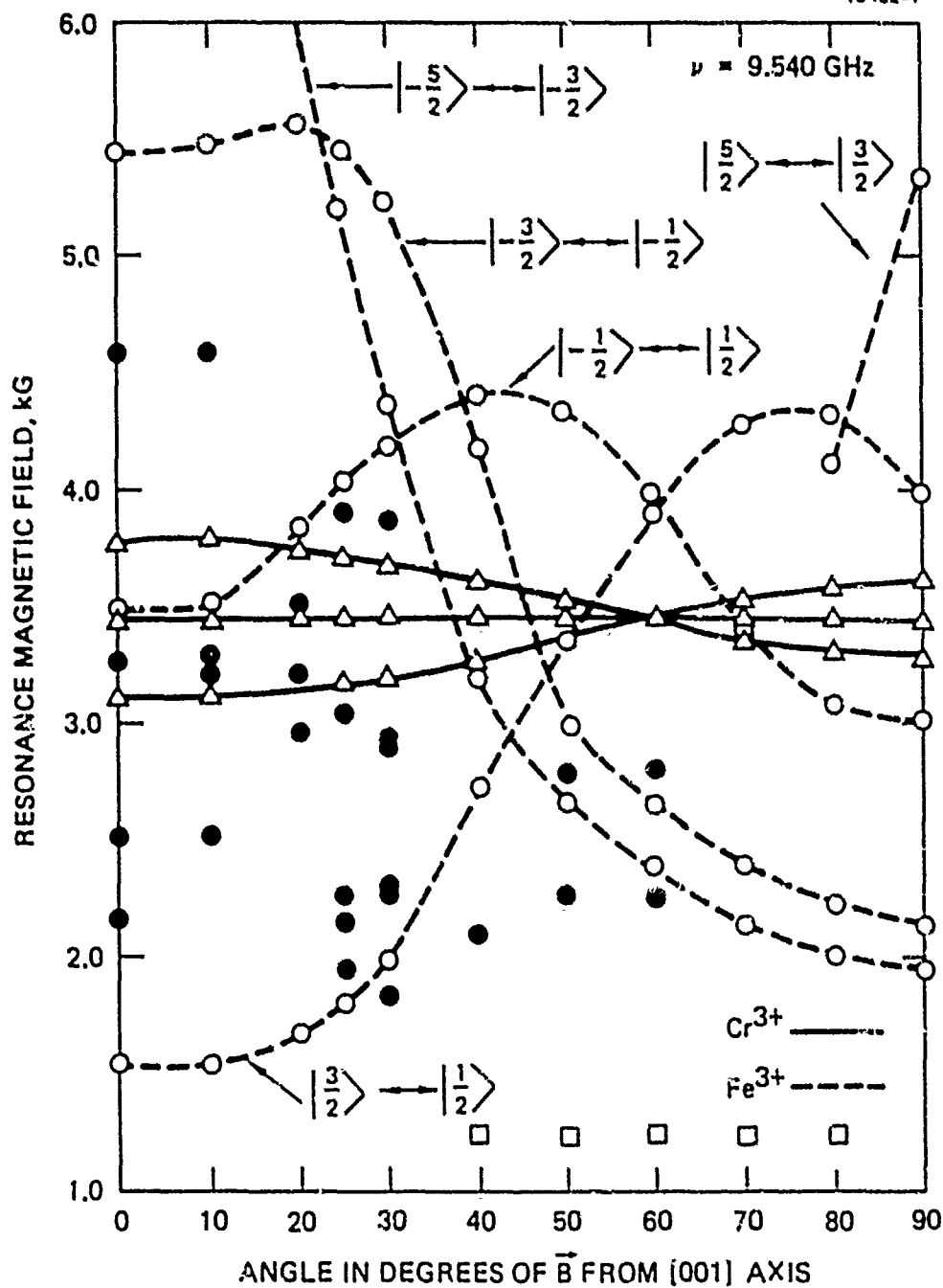


Figure 3-7. Angular dependence of the EPR transitions for  $\text{Fe}^{3+}$  (o) and  $\text{Cr}^{3+}$  ( $\Delta$ ) when  $\vec{B}$  is rotated in the (100) plane. The  $\bullet$  and  $\square$  represent unidentified transitions.

limit a strong axial EPR spectrum would be observed which is not consistent with our observations. Further, for the case of a  $\text{Fe}^{3+}\text{-V}_\text{O}$  center, it is expected that at certain orientations of the magnetic field, three sets of axial resonances should be observed, each set having a unique tetragonal axis. This arises because there are three equivalent oxygen sites in the  $\text{O}_\text{h}$   $\text{FeO}_6^{9-}$  unit from which an oxygen vacancy can be created to form the  $\text{C}_{4v}$   $\text{FeO}_5^{7-}$  cluster. Again this is not observed in our spectra, which supports our view that the iron resonances are associated with tetragonally distorted  $\text{FeO}_6^{9-}$  octahedra.

## 5. Photoluminescence Experiments

The energy depth of traps in the  $\text{BaTiO}_3$  band gap can be determined by measurements of the photoluminescence spectrum. The usefulness of this technique for the measurement of photorefractive centers rests on several factors: (1) the photoexcitation should be at wavelengths used for photorefractive applications, and not at shorter or longer wavelengths where other interactions may be involved, and (2) the intensities and energies of the spectral features should correlate with the concentration and identity of the photorefractive species.

We have taken photoluminescence spectra from three  $\text{BaTiO}_3$  crystals. In each case the excitation wavelength was 5209Å, and the pump intensity was  $50 \text{ W/cm}^2$ . Spectra were recorded using a double-monochromator and a cooled photomultiplier used in the photon-counting mode. The spectrum from each sample showed a weak line at 1.41 eV, and a still weaker feature at 1.365 eV. Although the three samples had trap densities (measured by beam coupling) and absorption coefficients differing by factors of 4 to 10, the energy location of the photoluminescence signals was unchanged, and the strengths varied by less than a factor of two. This leads us to believe that the recombination center near 1.4 eV may not be related to the photorefractive species so we have chosen not to relate this data to the measurements discussed above.

## 8. Heat Treatment Experiments

We believe that existing samples of  $\text{BaTiO}_3$  can be optimized by chemical reduction, in order to produce a predominance of  $\text{Fe}^{2+}$  ions, and a transformation from p-type to n-type conductivity. To this end we have performed preliminary experiments on two samples. Each was heated to  $800^\circ\text{C}$  in an argon atmosphere, with the intention of performing the same diagnostic measurements used for our as-grown crystals. This work was slowed, however, by difficulties encountered in poling the treated crystals. We found that an iterative procedure which includes several applications of mechanical pressure and repolishing works best, although we have not yet been able to reliably avoid cracking our samples.

The two samples which have been reduced are BW2 and G/L. We have measured the optical absorption in BW2 before and after heat treatment; we find that the absorption increases, but we were not able to separate out the possible contribution from domain scattering. We have measured the  $\text{Fe}^{3+}$  concentration in sample G/L by EPR, before and after heat treatment. We find that the  $\text{Fe}^{3+}$  concentration decreases (as expected), but not by more than a factor of two. Although these results are preliminary, they indicate that our heat treatment was not sufficient to induce a large increase in the  $\text{Fe}^{2+}/\text{Fe}^{3+}$  ratio. It is expected that more efficient reduction can be obtained through the use of a  $\text{CO}/\text{CO}_2$  atmosphere.

## E. INTERPRETATION OF DATA

### 1. Correlation of Measured Parameters

Based on our knowledge of the literature and the results of our experiments, we are now in a position to draw conclusions on the identity of the photorefractive species in  $\text{BaTiO}_3$ . We have already shown that the likely candidates are the transition metals Mn, Fe, Cu, Cr, Co and Ni. Among these elements, our EPR and impurity concentration measurements indicate that Fe is

consistently the most abundant. We thus hypothesize that Fe is the photorefractive species, and we associate level X in our energy level model with  $\text{Fe}^{2+}$ , and level  $X^+$  in our model with  $\text{Fe}^{3+}$ . Since hole photoconductivity dominates, we associate the filled traps with  $\text{Fe}^{3+}$ , and the empty traps with  $\text{Fe}^{2+}$ . On the basis of this hypothesis, we can perform one key test: to determine if a correlation exists between the total iron concentration (from emission spectroscopy), the concentration of  $\text{Fe}^{3+}$  (by EPR), the relative concentration of filled traps (from the absorption coefficient) and the concentration of empty traps (from photorefractive beam coupling). A similar correlation approach has been used in the study of photorefractive centers in  $\text{LiNbO}_3$ .<sup>4</sup> In Figure 3-8 we plot the parameters given above for each of four crystals. We see a clear correlation of the data, in the sense that all measured parameters increase monotonically with total Fe concentration. Ideally, a straight line behavior should be observed for each of the three plotted parameters, but the accuracy here is limited by experimental uncertainties, as well as possible variations in the oxidation/reduction state or quantum efficiency among our crystals. The data for two other crystals not shown in Figure 3-8 (GB3 and BW1) are poorly correlated with the remaining data for reasons given below:

GB3. This crystal contains a high concentration of bismuth, which contributes significantly to the absorption coefficient, and may also contribute to the photorefractive effect.

BW1. This crystal gave anomalous beam coupling results in that the data of gain versus grating period did not follow our model. We suspect that Cu is playing an important role in this crystal, based on the presence of  $\text{Cu}^{+2}$  in the EPR spectrum.

To summarize our conclusions, we have

$$N = [\text{Fe}^{2+}] \simeq 2-9 \times 10^{16} \text{ cm}^{-3},$$

$$N^+ = [\text{Fe}^{3+}] \simeq [\text{Fe}] \simeq 2-8 \times 10^{18} \text{ cm}^{-3},$$

and

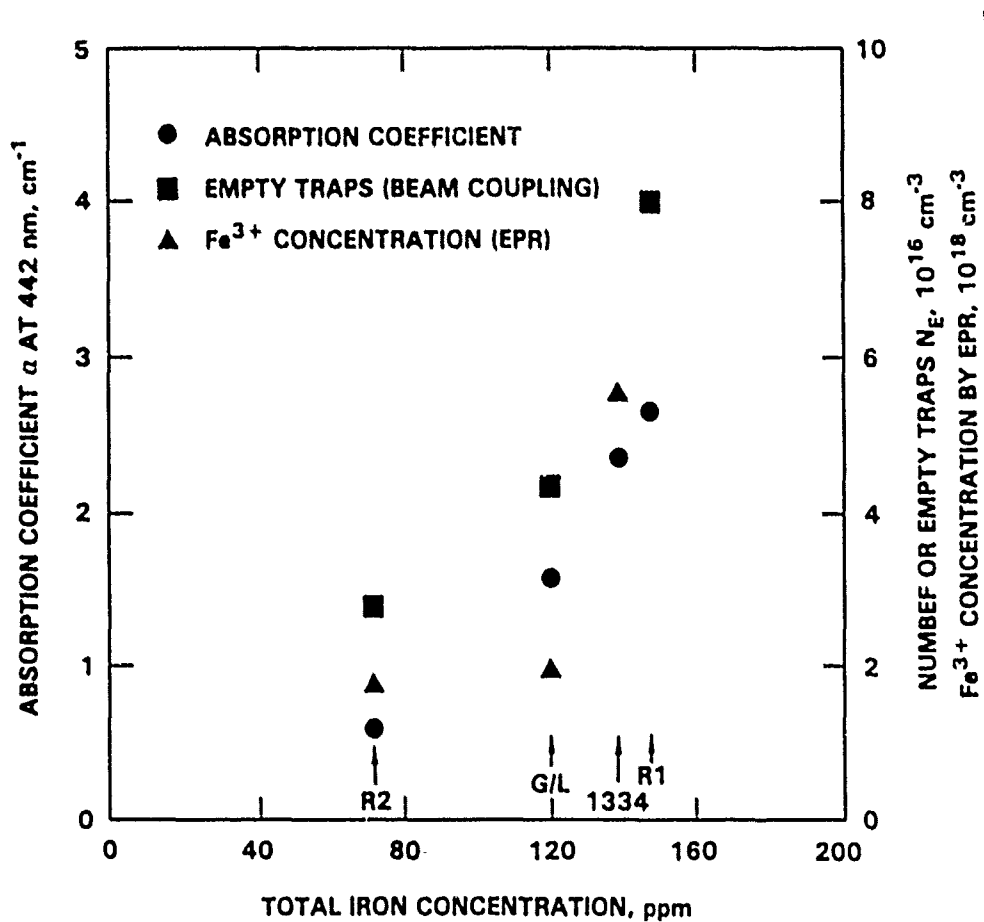


Figure 3-8. Absorption coefficient, concentration of empty traps and  $\text{Fe}^{3+}$  concentration versus total iron concentration for four samples of  $\text{BaTiO}_3$ . The samples are identified at the bottom of the plot.

$$\frac{[\text{Fe}^{3+}]}{[\text{Fe}^{2+}]} \approx 40-120 .$$

We now wish to determine if these results are consistent with observations in the literature. We note first that the large ratio of  $[\text{Fe}^{3+}]$  to  $[\text{Fe}^{2+}]$  is consistent with the oxidizing growth environment of  $\text{BaTiO}_3$  when using the top-seeded solution growth technique.<sup>21</sup> It is also consistent with data on  $\text{BaTiO}_3:\text{Fe}$  ceramics<sup>18,19</sup> processed in a similar atmosphere, for which  $\text{Fe}^{3+}$  is determined to be the dominant species. We also note that Fe is the most efficient photorefractive species in  $\text{LiNbO}_3$ ,<sup>38</sup> a similar material to  $\text{BaTiO}_3$ .

A plot of normalized electron and hole conductivity versus  $[\text{Fe}^{2+}]/[\text{Fe}^{3+}]$  ratio (as shown for  $\text{LiNbO}_3:\text{Fe}$  in Figure 3-3) provides a useful means for understanding the relative contribution of holes and electrons to the photorefractive effect in our samples of  $\text{BaTiO}_3$ . In order to prepare such a plot, we note first that the normalized conductivities defined in Equations (11) and (12) are related to the normalized differential conductivity [defined in Equation (2)] by

$$\bar{\sigma} = \bar{\sigma}_h - \bar{\sigma}_e . \quad (20)$$

From our previous analysis, we may write the normalized conductivities as

$$\bar{\sigma}_e = \frac{x^2 R}{1+x^2 R} \quad (21)$$

and

$$\bar{\sigma}_h = \frac{1}{1+x^2 R} , \quad (22)$$

where  $x = N/N^+ = [\text{Fe}^{2+}]/[\text{Fe}^{3+}]$ , and

$$R = \frac{\gamma_h s_e \mu_e}{\gamma_e s_h \mu_h} . \quad (23)$$



We can thus make a plot similar to Figure 3-3 for  $\text{BaTiO}_3$  if we know the value of the ratio  $R$  for our samples.

For  $\text{BaTiO}_3$ , little information is available regarding the values of recombination rate coefficient and photoionization cross section for electrons and holes. Estimates and measurements of the electron and hole mobilities for  $\text{BaTiO}_3$  differ widely. This is especially true for the hole mobility, for which values ranging between  $2 \times 10^{-4} \text{ cm}^2/\text{Vs}$  (Reference 39) and  $0.3 \text{ cm}^2/\text{Vs}$  (Reference 24) have been reported. For electrons, mobility values between  $0.1 \text{ cm}^2/\text{Vs}$  and  $1.0 \text{ cm}^2/\text{Vs}$  are typical.<sup>24,28,40,41</sup> While our experiment provides no direct information regarding these parameters, we find that  $R \gg 1$  is most consistent with our data. This may be explained with reference to Figure 3-9, where we have plotted the normalized conductivity for  $\text{BaTiO}_3$  (using Equations 21 and 22), with  $R=2500$ . We have also included data points for each of our crystals, using the values of  $\bar{\sigma}$  determined from our beam coupling measurements of  $F\bar{\sigma}$  (with  $F=0.9$ ). We see that all crystals lie in the transition region between hole and electron photoconductivity. With our assumed value of ratio  $R$ , the compensation point corresponds to  $x=R^{-1/2}=[\text{Fe}^{2+}]/[\text{Fe}^{3+}]=0.02$ . If we had assumed a much larger or smaller value for the ratio  $R$ , the resulting values of  $x=[\text{Fe}^{2+}]/[\text{Fe}^{3+}]$  for our samples (as read from Figure 3-9) would be inconsistent with the values obtained using our individual measured values of  $[\text{Fe}^{2+}]$  and  $[\text{Fe}^{3+}]$ . Finally, we note that crystal R2, with dominant electron photoconductivity, is still characterized by the condition  $x \ll 1$ , thus justifying our earlier approximation that  $N_E \approx N$  in this crystal.

## 2. Relation to Calculated Energy Levels of $\text{Fe}^{n+}$ in $\text{BaTiO}_3$

The energy level model in Figure 1-1 has proven to be adequate to explain our beam coupling data, and to provide a qualitative physical description of the photorefractive species. However, a significant body of literature exists on the energy

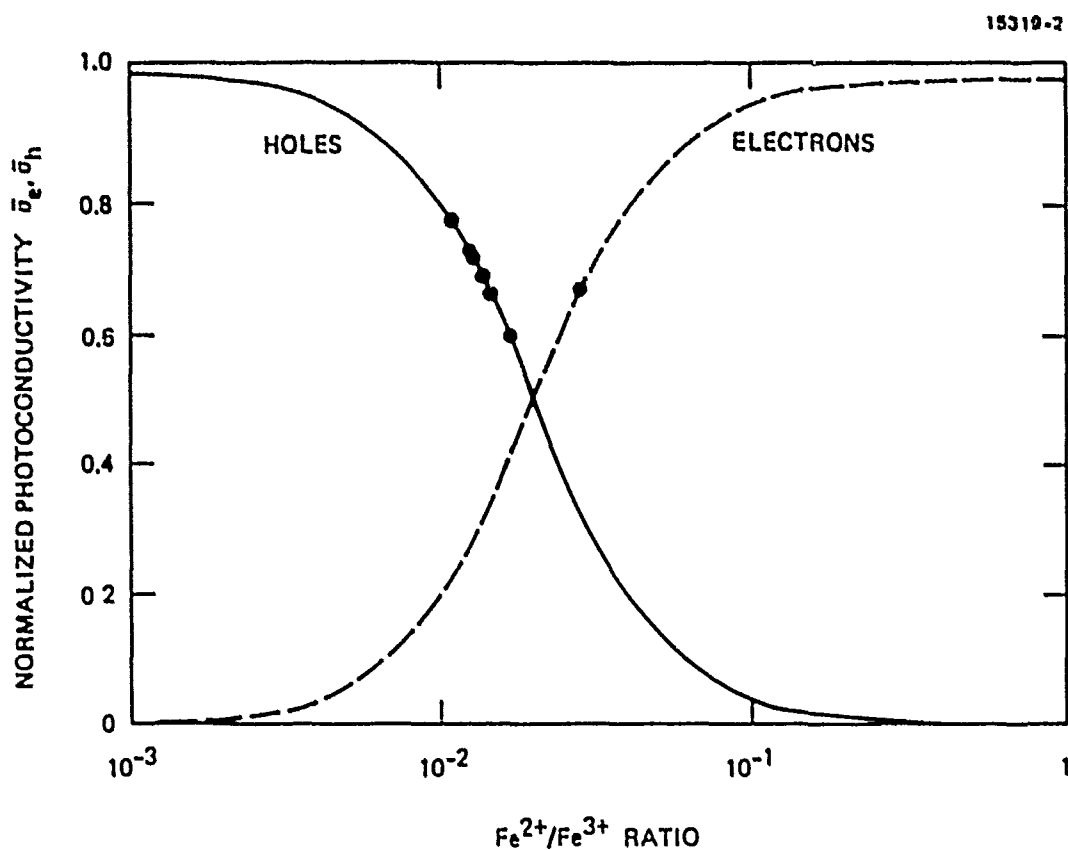


Figure 3-9. Relative contribution of electrons and holes to the photoconductivity in  $\text{BaTiO}_3$ , assuming  $R = \mu_e / \mu_h = 2500$ . The experimental points are from the beam coupling data, using  $\sigma = \sigma_h - \sigma_e$ .

levels of  $\text{Fe}^{n+}$  (and  $\text{Fe}^{n+}-V_O$ ) in  $\text{BaTiO}_3$  and  $\text{SrTiO}_3$  which indicates that the actual energy level structure in our samples may be more complicated. In the following discussion, we review the band structure of  $\text{BaTiO}_3$ , and the energy levels of  $\text{BaTiO}_3:\text{Fe}$ .

#### (i) Electronic Structure of Tetragonal $\text{BaTiO}_3$

The electronic band structure of  $\text{ABO}_3$  perovskite oxides has been extensively studied by various groups over the past few years.<sup>42-44</sup> For our purposes the work of Michel-Calendini and coworkers is most relevant since their studies also include band structure calculations of perovskite oxides doped with 3d transition metal ions.<sup>43,44</sup> This group uses the self-consistent field-multiple scattering-X $\alpha$  (SCF-MS-X $\alpha$ ) technique which appears to reproduce well the main features of the band structure of  $\text{ABO}_3$  perovskites.

On the basis of their SCF-MS-X $\alpha$  calculations carried out on  $\text{TiO}_6^{8-}$  clusters the following picture emerges of the electronic states in cubic ( $O_h$ ) and tetragonal ( $C_{4v}$ )  $\text{BaTiO}_3$ . For both symmetries the top of valence band is composed of oxygen 2p states of the barium ion, on the other hand, do not play an important role, and are not included in the calculation. In  $O_h$  symmetry the valence band edge can be decomposed into states with  $t_{1g}$  and  $t_{1u}$  symmetry and the bottom of conduction band has  $t_{2g}$  classification (see Figure 3-10a). As the symmetry is lowered from  $O_h$  to  $C_{4v}$ , the cubic levels split as well as shift. For example, in lower symmetry the levels ( $t_{1g}$ ,  $t_{1u}$ ) go over into ( $a_{1,e}$ ,  $a_{2,e}$ ) and ( $t_{2g}$ ) into ( $b_{2,e}$ ).

#### (ii) Electronic Structure of $\text{Fe}^{n+}$ in $\text{BaTiO}_3$

The electronic structure of a 3d ion embedded in  $\text{BaTiO}_3$  depends on the oxidation state, the electronic ground term (spin configuration) of the impurity, and the symmetry of the local electrostatic crystalline field. The influence of the spin configuration on the electronic levels of the impurity ion is

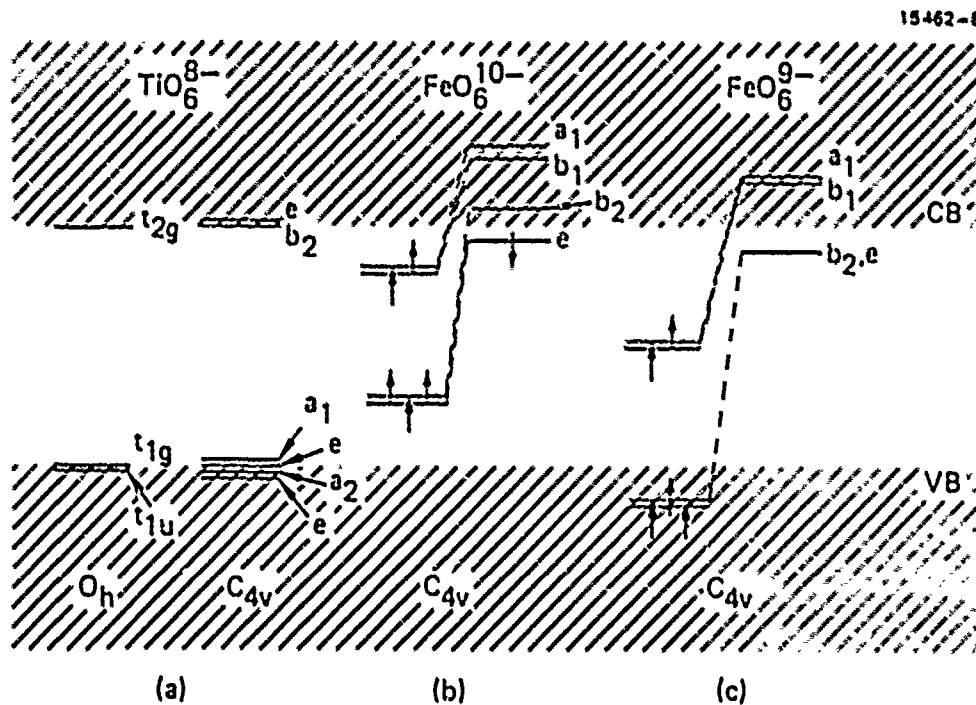


Figure 3-10. Schematic representation of the energy levels of  $M^nO_6^{12-n}$  clusters in  $BaTiO_3$ : (a)  $TiO_6^{8-}$ , (b)  $FeO_6^{10-}$  ( $Fe^{2+}$ ), and (c)  $FeO_6^{9-}$  ( $Fe^{3+}$ ). In Figure 10(b) and 10(c), the up-spin levels are located on the left side of each panel, and the down-spin levels are on the right. The levels in (a) and (c) have been calculated by the SCF-MS- $X_\alpha$  method.<sup>43-45</sup> The levels in (b) are extrapolated from those of the  $Fe^{2+}-V_O$  center.<sup>45,47</sup> The CB and VB correspond respectively to the conduction band minimum ( $t_{2g}$ , Ti 3d states) and the valence band maximum ( $t_{1g}$ , O 2p states of the  $TiO_6^{8-}$  cluster). Note the tendency of the higher valence states (e.g.,  $Fe^{3+}$ ) to lie lower in the band gap.

important when considering the electron exchange-correlation contribution to the molecular potential.

The spin-unrestricted SCF-MS-X $\alpha$  technique is ideally suited for these calculations and Michel-Calendini and co-workers<sup>45-49</sup> have used this method to obtain the molecular orbital (energy level) diagram of FeO<sub>6</sub><sup>-12+n</sup> clusters with O<sub>h</sub> and C<sub>4v</sub> symmetries. These calculations provide information on the location of the empty and occupied Fe impurity states in the TiO<sub>6</sub><sup>8-</sup> band gap. For example, in O<sub>h</sub> symmetry the Fe<sup>3+</sup> (S=5/2) t<sub>2g</sub><sup>↑</sup> level is below the valence band edge, whereas the e<sub>g</sub><sup>↑</sup> level is in the band gap. In this notation ↑ and ↓ refer to up- and down-spin electron spin states, respectively. Lowering the symmetry to C<sub>4v</sub> by either a tetragonal distortion of the FeO<sub>6</sub> octahedron or by removing an oxygen atom splits the t<sub>2g</sub> level into e and b<sub>2</sub> components with the e<sub>g</sub> level going over into states with a<sub>1</sub> and b<sub>1</sub> symmetry. The e<sup>↑</sup> and b<sub>2</sub><sup>↑</sup> levels, however, are still below the valence band edge whereas the a<sub>1</sub><sup>↑</sup> and b<sub>1</sub><sup>↑</sup> states are localized in the band gap (see Figure 3-10c). The main result is that the Fe<sup>3+</sup> center induces a reduction of the band gap due to empty spin-down b<sub>2</sub>, e states below the conduction band edge.

It is also important to consider the levels of Fe<sup>2+</sup> in BaTiO<sub>3</sub>. Unfortunately calculations of C<sub>4v</sub> Fe<sup>2+</sup> (S=2 or S=0) in tetragonal BaTiO<sub>3</sub> have not been reported; however, results in SrTiO<sub>3</sub> are available for low spin (S=0)<sup>45</sup> and high spin (S=2)<sup>46</sup> Fe<sup>2+</sup> in C<sub>4v</sub> symmetry (i.e., the C<sub>4v</sub> FeO<sub>6</sub><sup>10-</sup> complex) and for high spin Fe<sup>2+</sup>-V<sub>O</sub>.<sup>45,46</sup> Since Fe<sup>2+</sup> is observable by EPR only at low temperatures (because of its short spin-lattice relaxation time), at present we do not know its spin state in our BaTiO<sub>3</sub> samples. We assume, however, that it is high spin, since the Fe<sup>3+</sup> species is high spin, and it is unlikely that the two different valence states would not share this characteristic. Therefore, drawing on the results for Fe<sup>2+</sup>-V<sub>O</sub>, and noting that the perturbation of the 3d states of the Fe<sup>2+</sup> ion is greater in the FeO<sub>5</sub><sup>8-</sup> cluster than in the C<sub>4v</sub> FeO<sub>6</sub><sup>10-</sup> complex, we postulate that the spin configuration of the latter complex in BaTiO<sub>3</sub> is e<sup>↑2</sup>b<sub>2</sub><sup>↑</sup>a<sub>1</sub><sup>↑</sup>b<sub>1</sub><sup>↑</sup>e<sup>↓</sup> with

all levels in the band gap. By extending the analogy further we also suggest that the  $b_1^\uparrow$  and  $e^\downarrow$  levels are most likely localized below ( $\sim kT$ ) the conduction band edge (see Figure 3-10b) and therefore can be optically excited by photons with energies much smaller than the band gap.

As seen from the previous discussion,  $Fe^{2+}$  and  $Fe^{3+}$  in  $BaTiO_3$  have a complex energy level structure. However, it is clear that the  $FeO_6^{10-}$  ( $Fe^{2+}$ ) and  $FeO_6^{9-}$  ( $Fe^{3+}$ ) complexes with  $C_{4v}$  symmetry do have states localized in the band gap, such that the up-spin ( $\uparrow$ ) states (generally occupied) act as donors, whereas the down-spin ( $\downarrow$ ) states (generally empty) act as acceptors. Thus, heteronuclear intervalence transitions<sup>50,51</sup> involving O 2p+Fe 3d and Fe 3d+Ti 3d transitions with photon energies less than the bandgap are predicted. The success of the simplified energy level model of Section 3-A for most samples suggests that, at a given wavelength, the multiple level picture simplifies to an equivalent single level model, with rate coefficients which are an average of the individual coefficients.

## F. CONCLUSIONS

Our measurements have shown that Fe is the dominant photorefractive species in commercial  $BaTiO_3$  samples. This conclusion is consistent with the high iron impurity content in our samples (and other samples of  $BaTiO_3$  and  $LiNbO_3$ ), the large EPR signals from  $Fe^{3+}$ , and with the previous identification of Fe as the dominant species in  $LiNbO_3$ . The particular centers involved are  $Fe^{2+}$  and  $Fe^{3+}$  (association with oxygen vacancies does not appear to be important), and a simple two-level energy model adequately describes their participation in beam coupling experiments. At present, the only experimental inconsistency with the two-level model (shown schematically in Figure 3-1) is the observation that the response time<sup>17,60</sup> and the photoconductivity<sup>52</sup> in as-grown  $BaTiO_3$  vary sublinearly with intensity. This behavior suggests that other more shallow levels may play an intermediate role in trapping electrons or holes.<sup>53</sup>

## 1. Optimization of Response Time

On the basis of our analysis and measurements, we are in a position to recommend an approach to the optimization of the photorefractive properties of BaTiO<sub>3</sub>. The major limitations of BaTiO<sub>3</sub> for device applications are its low sensitivity and slow response time. In the case of the response time, typical values at an irradiance of 1 W/cm<sup>2</sup> are in the range 0.2-1.0 sec, depending on the grating period.<sup>16,17</sup> The response time can be written as<sup>8,10</sup>

$$\tau = \tau_{di} f(\Lambda_g, E_o) , \quad (24)$$

where  $\tau_{di}$  is the dielectric relaxation time,  $\Lambda_g$  is the grating period, and  $E_o$  is the applied electric field. The function  $f(\Lambda_g, E_o)$  accounts for the fact that the space charge is spatially modulated. For large grating periods and no applied field, it is not an important correction in BaTiO<sub>3</sub>.<sup>10</sup> The dielectric relaxation time may be written as  $\tau_{di} = \epsilon / 4\pi\sigma$ , where  $\epsilon$  is the relative dielectric constant, and  $\sigma$  is the conductivity. When the photoconductivity is much greater than the dark conductivity, it can be shown that

$$\tau_{di} \approx \epsilon / 4\pi e \alpha \phi \mu \tau_R I_o , \quad (25)$$

where the absorption coefficient  $\alpha$ , the quantum efficiency  $\phi$ , the mobility  $\mu$  and the recombination time  $\tau_R$  are appropriate for the dominant photocarrier, i.e., holes in as-grown BaTiO<sub>3</sub>. By substituting  $\alpha\phi = s_h [Fe^{3+}]$  and  $\tau_R = 1/\gamma_h [\mu_h^{2+}]$ , Equation (25) as written for an as-grown crystal becomes

$$\tau_{di}^{ag} \approx \frac{\epsilon}{4\pi e I_o} \left( \frac{\gamma_h}{s_h \mu_h} \right) x_{ag} , \quad (26)$$

where  $x_{ag} = [Fe^{2+}]/[Fe^{3+}]$  in our as-grown crystals. The promise for increasing the speed of response in BaTiO<sub>3</sub> lies in chemically

reducing samples to produce electron photoconductivity. In this case, the response time is given by

$$\tau_{di}^r \approx \frac{\epsilon}{4\pi e I_0} \left( \frac{\gamma_e}{s_e \mu_e} \right) \frac{1}{x_r}, \quad (27)$$

where  $x_r = [Fe^{2+}]/[Fe^{3+}]$  in the reduced crystal. The parameters in Equations (26) and (27) which are strongly impacted by reduction the factors in parentheses and the ratio  $x = [Fe^{2+}]/[Fe^{3+}]$ . In order to more clearly understand the impact of reduction, we can take the ratio of Equations (26) and (27), and write

$$\frac{\tau_{di}^r}{\tau_{di}^{ag}} = R^{-1} (x_{ag} x_r)^{-1}. \quad (28)$$

where  $R$  is defined in Equation (23). The particular advantage of reduction is that the ratio  $R$  is much greater than unity in our samples, leading to a corresponding reduction in  $\tau_{di}$ . However, account must also be taken of the change in concentration ratio,  $x$ . In our as-grown samples,  $x_{ag} \approx 8 \times 10^{-3} - 3 \times 10^{-2}$ . In order to obtain the full benefit of the larger mobility value, we require the populations of  $Fe^{2+}$  and  $Fe^{3+}$  to be reversed, i.e.,  $x_r \approx 40-120$ . As will be seen below, this condition is not easy to achieve.

A relationship similar to Equation (28) can be obtained using the more general form for the response time [Equation (24)]. In this case, the dependence on  $R$  and  $x$  is more complicated, but is qualitatively similar to that in Equation (28).

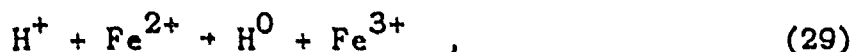
## 2. Issues In Reduced Crystals

While reduced samples of  $BaTiO_3$  with n-type conductivity are not difficult to produce,<sup>18,19,27,28,54</sup>  $Fe^{3+}$  is known to be very stable in  $BaTiO_3$ .<sup>18,19,54</sup> In particular, in References 19 and 54, negligible conversion of  $Fe^{3+}$  to  $Fe^{2+}$  was observed at oxygen

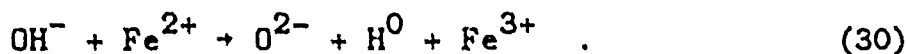


partial pressures as low as  $10^{-22}$  atm. Only in a pure  $H_2$  environment ( $10^{-26}$  atm oxygen) was conversion of ~50% achieved. However, under these heavy reduction conditions, the crystals are highly conductive and opaque.

The stability of  $Fe^{3+}$  in the above experiments is likely due to the strong oxidizing tendency of  $H^+$  or  $OH^-$ , which are expected to be present at large concentrations in samples treated with  $H_2O$  and/or  $H_2$ :

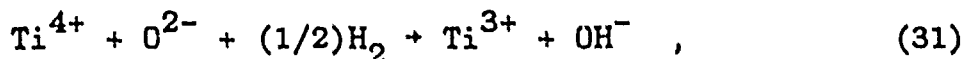


and

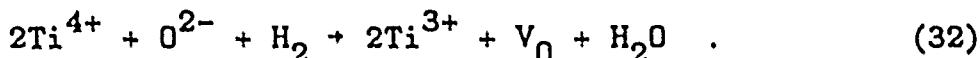


Even in as-grown crystals, these reactions could play a significant role, since we have measured  $OH^-$  concentrations as large as  $10^{19}/cm^3$  in our samples.<sup>55</sup>

The use of hydrogen for reduction has another potential adverse effect: the reduction of  $Ti^{4+}$ :



or

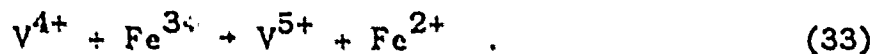


$Ti^{3+}$  has been detected in samples of  $BaTiO_3$  reduced in hydrogen,<sup>59</sup> and is likely to contribute to absorption in the visible and near infrared.

As seen above,  $H^+$  and  $OH^-$  tend to stabilize  $Fe^{3+}$ , while  $H_2$  reduces  $Ti^{4+}$ ; both of these are opposite to the desired effect. This emphasizes the importance of avoiding the introduction of hydrogen during growth, and processing with other reducing agents, such as  $CO/CO_2$ .

Another approach to enhancing the population of  $Fe^{2+}$  is to introduce a codopant with Fe into the melt which stabilizes  $Fe^{2+}$  in crystals grown in air. This has the advantage of ease in preparation, and minimization of effects from  $V_0$ ,  $Ti^{3+}$  and free

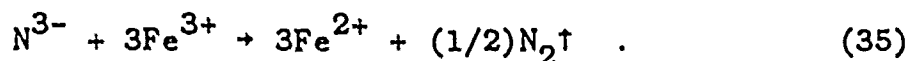
electrons, which are produced in reduced crystals. One possible codopant is vanadium in the 4+ valence state, which substitutes for  $\text{Ti}^{4+}$ . This would stabilize  $\text{Fe}^{2+}$  by



$\text{V}^{5+}$  is expected to be a deep donor in  $\text{BaTiO}_3$ , and may itself contribute to the photorefractive effect. The disadvantage of vanadium as a codopant is that the above interaction is a next-nearest-neighbor interaction. We can make use of the stronger forces among nearest neighbors by codoping with  $\text{N}^{3-}$ , substituting for  $\text{O}^{2-}$  in the lattice. The codopant could be introduced by adding TiN into the melt. The  $\text{N}^{3-}$  would add a new source of negative charge in Equation (16) (the charge balance equation). Assuming that the added charge affects only the Fe, we may write

$$[\text{N}^{3-}] + 2 \Delta[\text{Fe}^{2+}] + \Delta[\text{Fe}^{3+}] = 0 \quad (34)$$

where  $\Delta[\text{Fe}^{n+}]$  is the change in  $[\text{Fe}^{n+}]$  due to the addition of  $\text{N}^{3-}$ . Thus, for every two  $\text{N}^{3-}$  added, two  $\text{Fe}^{3+}$  are converted to one  $\text{Fe}^{2+}$ .  $\text{N}^{3-}$  also tends to reduce  $\text{Fe}^{3+}$  in the melt, by the reaction



We also note that energy levels due to filled or partially filled O vacancies could play a role in the photorefractive properties of reduced  $\text{BaTiO}_3$ . However, as indicated earlier, these energy levels are thought to be quite shallow - 0.025 eV for  $\text{V}_0$  with two trapped electrons, and 0.2 eV for  $\text{V}_0$  with one trapped electron.<sup>15</sup> The importance of these centers in reduced crystals will require further study.

Recent photorefractive experiments on samples of  $\text{BaTiO}_3$  treated at 650°C in  $\sim 10^{-5}$  atm oxygen have shown the expected conversion to electron photoconductivity, along with an improvement in beam coupling gain, and a linear dependence of

response time on intensity.<sup>56</sup> However, the response time for typical cw intensities was not significantly improved. This may be an indication that the large value of the ratio  $R$  was compensated by a less optimum value of  $x=[Fe^{2+}]/[Fe^{3+}]$  [see Equation (28)]. Note also that the linear dependence of response time on intensity suggests that reduced crystals should have an improved response time at the higher intensities which are typical of pulsed lasers.

In order to more fully characterize the photorefractive performance of  $BaTiO_3$ , it would be useful to measure the mobility, photoionization cross section, recombination rate coefficient and quantum efficiency for both electrons and holes in samples of interest by a direct photorefractive technique. Such measurements can be performed in the transient<sup>57</sup> and short pulse<sup>58</sup> regimes, and they thus compliment the density and conductivity measurements which can be performed in the steady state.

### REFERENCES (SECTION 3)

1. G.E. Peterson, A.M. Glass and T.J. Negran, Appl. Phys. Lett. 19, 130 (1971).
2. G.E. Peterson, A.M. Glass, A. Carnevale and P.M. Bridenbaugh, J. Am. Cer. Soc. 56, 278 (1973).
3. M.G. Clark, F.J. DiSalvo, A.M. Glass and G.E. Peterson, J. Chem. Phys. 59, 6209 (1973).
4. H. Kurz, E. Kratzig, W. Keune, H. Engelmann, U. Gonser, B. Dischler and A. Rauber, Appl. Phys. 12, 355 (1977).
5. M.B. Klein, "Origins of the Photorefractive Effect in BaTiO<sub>3</sub>," Proc. SPIE 519, 136 (1984).
6. M.B. Klein and G.C. Valley, J. Appl. Phys. 57, 4901 (1985).
7. V.L. Vinetskii and N.V. Kukhtarev, Sov. Phys. Sol. St., 16, 2414 (1975).
8. N.V. Kukhtarev, Sov. Tech. Phys. Lett., 2, 438 (1976).
9. N.V. Kukhtarev, V.B. Markov, S.G. Odulov, M.S. Soskin and V.L. Vinetskii, Ferroelectrics 22, 949 and 961 (1979).
10. G.C. Valley and M.B. Klein, Opt. Engin. 22, 704 (1983).
11. D.L. Staebler and J.J. Amodei, J. Appl. Phys. 43, 1042 (1972).
12. R. Orlowski and E. Kratzig, Solid St. Comm. 27, 1351 (1978).
13. G.C. Valley, to be published.
14. H.J. Hagemann, Ph.D. Thesis, RWTH Aachen (1980).
15. C.N. Berglund and H.J. Braun, Phys. Rev. 164, 790 (1967).
16. J. Feinberg, D. Heiman, A.R. Tanguay, Jr., and R.W. Hellwarth, J. Appl. Phys. 52, 1297 (1980).
17. S. Ducharme and J. Feinberg, J. Appl. Phys. 56, 839 (1984).
18. H.J. Hagemann and D. Hennings, J. Am. Cer. Soc. 64, 590 (1981).
19. H.J. Hagemann, A. Hero and U. Gonser, Phys. Stat. Sol. (a) 61, 63 (1980).
20. E. Siegel and K.A. Muller, Phys. Rev. B20, 3587 (1979).

21. V. Belrus, J. Kalinajs, A. Linz and R.C. Folweiler, Mat. Res. Bull. 6, 899 (1971).
22. S.H. Wemple, "Electrical Contact to n- and p-Type Oxides," in Ohmic Contacts to Semiconductors, B. Schwartz, Ed., (Electrochemical Society, New York, 1968).
23. N.G. Error and D.M. Smyth, J. Solid State Chem. 24, 235 (1978).
24. N.H. Chan, R.K. Sharma and D.M. Smyth, J. Am. Chem. Soc. 64, 556 (1981).
25. N.H. Chan, R.K. Sharma and D.M. Smyth, J. Am. Chem. Soc. 65, 167 (1982).
26. J. Daniels, Philips Res. Repts. 31, 505 (1976).
27. S. Ikegami and I. Ueda, J. Phys. Soc. Jpn. 19, 159 (1964).
28. C.N. Berglund and W.S. Baer, Phys. Rev. 157, 358 (1967).
29. N.V. Kukhtarev, E. Kratzig, H.C. Kulich and R.A. Rupp, Appl. Phys. B 35, 17 (1984).
30. D. Rytz, unpublished.
31. F.J. Morin and J.R. Oliver, Phys. Rev. B8, 5847 (1973).
32. A. Abragam and B. Bleaney, Electron Paramagnetic Resonance of Transition Metal Ions (Oxford Press, London, 1970).
33. A.W. Hornig, R.C. Rempel and H.E. Weaver, J. Phys. Chem. Solids 10, 1 (1959).
34. H. Ikushima and S. Hayakawa, J. Phys. Soc. Jpn 19, 1986 (1964).
35. J. Rodel and G. Tomandl, J. Mat. Sci. 19, 3515 (1984).
36. M. Nakahara and T. Murakami, J. Appl. Phys. 45, 3795 (1974).
37. E.S. Kirkpatrick, K.A. Muller and R.S. Rubins, Phys. Rev. B5, A86 (1964).
38. W. Phillips, J.J. Amodei and D.L. Staebler, RCA Review 33, 94 (1972).
39. G.A. Cox and R.H. Tredgold, Phys. Lett. 11, 22 (1964).
40. P. Gerthsen, K.H. Hardtl and A. Csillag, Phys. Stat. Solidi A13, 127 (1972).

41. A.M.J.H. Seuter, Philips Res. Repts. Suppl., No. 3 (1974).
42. L.F. Mattheis, Phys. Rev. B12, 4718 (1972).
43. P. Pertosa and F.M. Michel-Calendini, Phys. Rev. B17, 2011 (1978).
44. F.M. Michel-Calendini, H. Chermette and J. Weber, J. Phys. C:Solid St. Phys. 13, 1427 (1980).
45. F.M. Michel-Calendini, Ferroelectrics 37, 499 (1981).
46. F.M. Michel-Calendini, Solid St. Comm. 52, 167 (1984).
47. P. Moretti and F.M. Michel-Calendini, Ferroelectrics 55, 219 (1984).
48. F.M. Michel-Calendini, Ferroelectrics Lett. 3, 31 (1984).
49. F.M. Michel-Calendini, L. Hafid, G. Godefroy and H. Chermette, Solid St. Comm. 54, 951 (1985).
50. N.S. Hush, Prog. Inorg. Chem. 8, 391(1967).
51. R.G. Burns, Ann. Rev. Earth Planet. Sci. 9, 345 (1981).
52. E. Kratzig, F. Welz, R. Orłowski, V. Doorman, and M. Rosenkranz, Solid St. Comm. 34, 817 (1980).
53. A. Rose, "Concepts in photoconductivity and allied problems," (Robert Krieger Publishing Company, New York, 1978).
54. H.J. Hagemann and H. Ihrig, Phys. Rev. B20, 3871 (1979).
55. M. Minden, unpublished.
56. S. Ducharme and J. Feinberg, to be published, JOSA B special issue on Materials For Optical Processing.
57. R.A. Mullen and R.W. Hellwarth, J. Appl. Phys. 58, 40 (1985).
58. G.C. Valley, IEEE J. Quantum Elec. QE-19, 1637 (1983).
59. P. Coufova, Czech. J. Phys. B 18, 1038 (1968).
60. D. Rak, I. Ledoux and J.P. Huignard, Opt. Comm. 49, 302 (1984).

## SECTION 4

### CONCLUSIONS AND RECOMMENDATIONS FOR FUTURE WORK

In this section, we summarize our conclusions and recommendations for future work. The recommendations described below form the core of a program described in our follow-on proposal to be submitted shortly.

#### A. CRYSTAL GROWTH

Attempts to stabilize the cubic phase of  $\text{BaTiO}_3$  by reactive atmosphere processing of powders were not successful. Although some experiments pointed to the possibility of eliminating the hexagonal phase by this approach, it did not prove possible to obtain the cubic phase reproducibly, and it is unlikely that these results were indicative of true equilibrium behavior.

A considerable amount of experience was gained under this program on the effects of various RAP treatments on  $\text{BaTiO}_3$  powders. The results indicate that, of the halogens, only iodine can be used without causing any breakdown of  $\text{BaTiO}_3$ . Application of a  $\text{CO}/\text{CO}_2/\text{I}_2$  RAP would appear to be a viable approach to reduce  $\text{OH}^-$  incorporation during crystal growth. However, it will probably be necessary to follow such a treatment with a more oxidizing gas mixture, either  $\text{CO}_2/\text{I}_2$  or  $\text{O}_2/\text{I}_2$ , to reverse the tendency toward oxygen deficiency and/or replacement of oxygen by iodine. The effectiveness of such an approach can best be judged from actual crystal growth experiments.

The congruent growth of  $\text{BaTiO}_3$  remains a worthwhile pursuit in view of its potential advantages (much faster growth rate, higher yield, more homogeneous impurity distribution) over the standard top-seeded solution growth method. However, it is now apparent that other approaches to stabilizing cubic  $\text{BaTiO}_3$  may prove more fruitful than that explored during this program. One such approach that has been used successfully at Hughes Research

Laboratories for the rapid Czochralski growth of  $\text{BaTiO}_3$  is that of doping with  $\sim 2.5\%$   $\text{SrTiO}_3$ . We would therefore propose to continue the development of this material toward obtaining optimized photorefractive crystals in a future program.

It is apparent from the study of the origins of the photorefractive effect that control of the impurity contents of  $\text{BaTiO}_3$  crystals is essential to produce optimized crystals. The nature of the impurities, their valence state, and interactions between different impurities are key parameters to be controlled. In order to accomplish this, we believe that rigorous control of the chemical environment during crystal growth is required. The experience gained under this program can be directly applied to achieving this goal.

## B. IDENTIFICATION AND CHARACTERIZATION OF THE PHOTOREFRACTIVE SPECIES

Our experiments indicate that iron is the dominant photorefractive species in  $\text{BaTiO}_3$ . While our measurements have allowed us to determine the concentrations of  $\text{Fe}^{2+}$  and  $\text{Fe}^{3+}$ , we have not been able to determine separate transport parameters for electrons and holes. These parameters can be determined from response time and short pulse measurements, as described below. In order to optimize the response time in  $\text{BaTiO}_3$ , we must make use of the favorable electron transport properties of reduced crystals. It is thus important to develop a reliable technique for the reduction of  $\text{BaTiO}_3$  (i.e., conversion of  $\text{Fe}^{3+}$  to  $\text{Fe}^{2+}$ ), and to characterize these samples. Finally, the possibility of producing new centers by gamma irradiation is also deserving of further study.

### 1. Response Time Measurements.

By measuring the decay time of a photorefractive grating, we can measure the number of empty traps (thus allowing comparison to the beam coupling data), and the  $\mu\tau_R$  product ( $\mu$  is the mobility and  $\tau_R$  is the recombination time). The latter is a key



parameter in characterizing the transient properties, as well as the photoconductivity. By heat treating the samples (see below), we can measure  $\mu\tau_R$  for both electrons and holes. Using the data for the number of empty traps, we can obtain  $\mu/\gamma$  for each carrier, where  $\gamma$  is the recombination rate coefficient. Under certain conditions, the response time measurements can also determine the photorefractive absorption coefficient, or the quantum efficiency.

## 2. Short Pulse Response Measurements.

By writing a grating with pulses whose length is less than the recombination time, we can monitor the buildup of the photorefractive grating, and thus measure the recombination time. This data, combined with the data for  $\mu\tau_R$ , allows the determination of mobility. Such a measurement would be particularly useful, not only because accurate values of mobility are hard to obtain, but also because ours would be a photorefractive measurement, and thus of direct relevance to our modeling.

## 3. Optimization Through Heat Treatment.

On the basis of the results obtained thus far, we believe that chemical reduction of commercial samples of  $\text{BaTiO}_3$  should lead to an improvement in the response time by two to three orders of magnitude. We propose to develop the proper annealing atmosphere, treat several crystals, and characterize their properties (especially their time response). The availability of heat-treated crystals will also allow us to confirm the dominance of Fe as the photorefractive species, by correlating the concentration of  $\text{Fe}^{3+}$  with the number of empty traps and the absorption coefficient in the same crystal.

## 4. Photorefractive Properties of Irradiated Crystals.

It is well known that a variety of defects can be induced in oxide crystals by gamma irradiation. We propose to

systematically irradiate a variety of crystals, and characterize the induced defects using the techniques developed for this program.

#### ACKNOWLEDGMENTS

We would like to acknowledge helpful discussions with D. Rytz, G.C. Valley, R. Pastor, R.N. Schwartz, and L.G. DeShazer, and technical assistance by R. Sipman. We thank K.W. Kirby for his expertise in carrying out the reactive atmosphere processing experiments and F.V. Lee for assistance in the synthesis of powders. The EPR measurements were performed by R.N. Schwartz, through the hospitality of Professor Larry Kevan, University of Houston. The photoluminescence measurements were performed by A. Hunter.

## APPENDIX 1

### ORIGINS OF THE PHOTOREFRACTIVE EFFECT IN $\text{BaTiO}_3$

M. B. Klein  
 Hughes Research Laboratories  
 3011 Malibu Canyon Road  
 Malibu, CA 90265

#### Abstract

We have used a number of experimental techniques to identify the photorefractive species in commercial samples of  $\text{BaTiO}_3$ . We find that iron impurities (in the  $\text{Fe}^{2+}$  and  $\text{Fe}^{3+}$  states) are the most likely source of photorefractive effect, although other transition metal impurities may also contribute.

#### Introduction

Photorefractive materials offer great promise for applications in adaptive optics and optical data processing using degenerate four-wave mixing.  $\text{BaTiO}_3$  is a particularly promising material, primarily because the very large value of the electro-optic tensor component  $r_{33}$  yields correspondingly large values of grating efficiency, beam coupling gain, and four-wave mixing reflectivity. [1] As an example, four-wave mixing reflectivities as large as 20 have been observed in  $\text{BaTiO}_3$ , with no electric field applied to the crystal. Such large reflectivities are particularly desirable in phase conjugate resonator applications, where  $\text{BaTiO}_3$  is generally the material of choice.

In spite of the intense interest in the applications of  $\text{BaTiO}_3$ , little is known regarding the species responsible for the photorefractive effect in this material. If this species can be conclusively identified, we can then hope to optimize the performance of this material through doping and heat treatment.

In this study we have drawn on information in the literature and our own experiments to arrive at a tentative identification of the photorefractive species in  $\text{BaTiO}_3$ . We will first present a physical description of grating formation in a photorefractive material, using the conventional band transport model. We will then review the possible defects which could be responsible for photorefractivity in  $\text{BaTiO}_3$ . Finally, we will describe our measurements, and our tentative identification of the photorefractive species.

#### Grating formation in photorefractive materials

The mechanism of grating formation in photorefractive materials can be described with reference to Figures 1 and 2. We assume that electrons are optically excited from filled donor sites to the conduction band, where they migrate to dark areas in the crystal by drift or diffusion before recombining into an empty trap. The transported charges result in an ionic space charge grating that is, in general, out of phase with the incident irradiance. The space charge grating is balanced by a periodic space charge electric field in accordance with Poisson's equation. This space charge field modulates the refractive index through the electro-optic effect. If no electric field is applied to the crystal (and the bulk photovoltaic effect is negligible), then diffusion alone leads to a phase shift of  $\pi/2$  between the incident irradiance and the space charge field. This shifted grating plays an important role in the beam coupling experiments described later.

In Figure 1 (using  $\text{LiNbO}_3:\text{Fe}$  as an example), we have assumed that the population of  $\text{Fe}^{2+}$  exceeds the population of  $\text{Fe}^{3+}$ , and that the photoconductivity is dominated by electrons. This is generally true for  $\text{LiNbO}_3$  treated in a reducing atmosphere. However, if the sample is heated in an oxygen atmosphere, the population of  $\text{Fe}^{3+}$  can be made sufficiently large that hole photoconductivity dominates. In this case the model of charge transport described above is still valid, but the resulting space charge electric field is reversed in direction (i.e. opposite in sign).

At the crossover point between these two limits, the hole photoconductivity is equal to the electron photoconductivity, giving

$$p\nu_h = n\nu_e,$$

or

$$\frac{p}{n} = \frac{\nu_e}{\nu_h}.$$

where  $p$ ,  $n$  are the concentrations of holes and electrons, and  $\mu_h$ ,  $\mu_e$  are the hole and electron mobilities. If the photoionization cross sections and recombination rate coefficients are comparable for  $Fe^{2+}$  and  $Fe^{3+}$ , then the above condition can be written as

$$\frac{[Fe^{3+}]}{[Fe^{2+}]} = \left( \frac{\mu_e}{\mu_h} \right)^{1/2}.$$

Measurements and estimates of  $\mu_e$  and  $\mu_h$  in materials like  $LiNbO_3$  and  $BaTiO_3$  differ widely, but it is generally accepted that  $\mu_e \gg \mu_h$  at room temperature. Using a conservative estimate that  $\mu_e$  100  $\mu_h$ , we find that for equal values of electron and hole conductivity,

$$[Fe^{3+}] \approx 10[Fe^{2+}].$$

This is exactly the relationship found in Ref. 5 for  $LiNbO_3:Fe$ . Note also that it is possible for the electron photoconductivity to exceed the hole photoconductivity, even when  $[Fe^{3+}] > [Fe^{2+}]$ . For the example given here, this would be true for

$$[Fe^{2+}] < [Fe^{3+}] < 10[Fe^{2+}].$$

#### Defects in $BaTiO_3$

There are two major types of defects in the  $BaTiO_3$  lattice which could lead to deep levels in the band gap and donor/acceptor behavior: vacancies or impurities. It is always expected that impurities will be present in the 10-100 ppm range, unless extraordinary precautions are taken in purifying starting materials and controlling the growth environment. Vacancies are also commonly present, if only to compensate for the charge imbalance introduced by the impurities.

In recent years there have been extensive studies of defects in  $BaTiO_3$ , and their relation to high temperature conductivity<sup>9,10</sup>. Two results from these studies are important here. First, the dominant impurities are found to be transition metals, as expected from their large abundance in nature. Second, it was found that  $BaTiO_3$  prepared in air from typical starting materials is p-type at high temperatures, i.e. the dominant levels in the band gap are acceptors. The commonly accepted model explaining the p-type behavior can be described as follows. The dominant transition metal impurities in  $BaTiO_3$  are thought to occupy titanium sites in the lattice<sup>9,10</sup>. Most transition metals have a valence states less than or equal to that of titanium in the  $BaTiO_3$  lattice (i.e. +4). The resulting charge imbalance is compensated by oxygen vacancies and free holes.

It is important to note<sup>9,10</sup>  $BaTiO_3$  can be made n-type, but only by heat treatment in a reducing atmosphere. The effect of reducing the crystals is to increase the number of oxygen vacancies above the number required to compensate for the transition metal impurities. As a result, lower valence states of the impurities are created, along with free electrons.

If the same samples are heated in oxygen at high pressure, then the number of oxygen vacancies is reduced below the number required to compensate for transition metal impurities. This will then create higher valence states of the impurities and more free holes, thus leading to higher p-type conductivity. Further treatment will eventually produce Ba and Ti vacancies, along with a still larger concentration of free holes.

We will make use of the above observations, along with our own measurements, in seeking to determine the photorefractive species in our own samples.

#### Measurements

We have measured a number of physical and optical properties of commercially available  $BaTiO_3$  crystals (purchased from Sanders Associates), with the goal of determining the nature and the number of deep traps associated with the photorefractive effect. Our measurements fall into four categories, as described below.

##### Photorefractive beam coupling

Beam coupling is a useful technique for measuring the carrier with the larger<sup>11,12</sup> photoconductivity and the density of empty traps in a photorefractive material. In this technique, two beams are incident on the sample, thereby producing a spatially periodic irradiance pattern (see Fig. 2). If the resultant refractive index pattern (or grating) is not in phase with the irradiance pattern, then energy is transferred from one beam to another, in a direction determined by the crystal orientation and the carrier with the larger photoconductivity, but not by the relative power in the beams.

For the specific case of  $\text{BaTiO}_3$ , we consider the crystal orientation and beam notation shown in Fig 3. We assume that the crystal is oriented so the the signal beam  $I_s$  is amplified. If the intensity of the signal beam is much less than that of the reference wave, then the signal intensity at the crystal output is given by

$$I_s(L) = I_s(0)\exp(r-a)L,$$

where  $r$  is the gain coefficient and  $a$  is the absorption coefficient. In our experiment we measure the effective gain [13]  $\gamma_0$ , defined as

$$\gamma_0 = \frac{I_s(L) \text{ with reference wave}}{I_s(L) \text{ without reference wave}}$$

In the absence of an applied electric field (as is the case for all our experiments), the phase of the periodic space charge field is shifted from that of the irradiance by  $\pi/2$ . For this case, the gain  $r$  is given by

$$r = 2n^3 r_{\text{eff}} E_{\text{sc}} / \lambda \cos \theta$$

where  $\theta$  is the Bragg angle inside the crystal, and  $r_{\text{eff}}$  is the effective electro-optic coefficient. The latter parameter can be less than the appropriate electro-optic tensor component  $r_{\text{eff}}$  due to imperfect poling of the crystals. The space charge electric field is a known function of the grating period  $\Lambda_g$  and the number of empty traps,  $N_g$ .

In our experiments, we have determined the sign of the photoconductivity in each of our samples by determining the c-axis orientation which gives gain for the weak signal beam<sup>12</sup>. From the measurement of the gain as a function of grating period, we can determine the value of  $N_g$  by fitting a theoretical curve to our data. The results of our measurements are given in Table I (columns 2 and 3). We see that in all crystals but one, the sign of the photoconductivity is positive, i.e. the dominant photocarriers are holes.

#### Optical absorption

While beam coupling measurements allow the determination of the number of empty traps, optical absorption measurements allow a relative determination of the number of filled traps, provided that the absorbing species is the same for each measurement. In Figure 4, we show curves of absorption coefficient  $a$  as a function of wavelength for four different samples. The measured values of  $a$  were obtained from laser transmission measurements, with account taken for Fresnel reflection from the entrance and exit faces. The absorption coefficient includes a contribution from scattering which is thought to be at most  $0.1 \text{ cm}^{-1}$  in our crystals. The curves drawn through the measured points were obtained from broadband transmission measurements using a Cary 14 spectrophotometer.

We note from Figure 4 that three of the four crystals show a broad, featureless "tail" extending from the fundamental absorption edge at  $3500 \text{ \AA}$ . One sample does show a more prominent peak at  $5000 \text{ \AA}$ . In Table I we have included the value of  $a$  at  $5145 \text{ \AA}$  for each sample (with E[6]), in order to allow a relative determination of the density of filled traps.

#### Weight measurements of impurity concentration

As mentioned earlier, previous studies of ceramic and single crystal  $\text{BaTiO}_3$  have shown a significant concentration of transition metal impurities. As an initial measurement with high sensitivity, we surveyed all impurities in two separate samples using SIMS. The elements observed were H, Li, Na, K, C, Al, Si, Ca, Sr, Ni, Mn, Cr and Fe. Of the materials listed, Ca and Sr substitute readily for Ba in the  $\text{BaTiO}_3$  lattice and have the same valence state, thus producing no defects. The first seven elements do not exist commonly in more than one valence state, and thus can not support the intervalence transfer required for the photorefractive species. The remaining species are transition metals and must be considered as possible candidates.

In order to make quantitative measurements of transition metals in our crystals, samples from three of our crystals were sent to commercial analytical laboratories for impurity measurement by spark source emission spectroscopy. The results of these measurements are given in Table II. We note that Fe is consistently the most abundant impurity, being present in concentrations on the order of  $100 \text{ ppm}$ . Note also that the relative number of filled and empty traps are in qualitative agreement with the Fe concentration in each sample.

### Electron paramagnetic resonance (EPR) measurements

Room temperature EPR spectra at X-band ( $\sim 9.3$  GHz) have been observed in 5 different single crystals of  $\text{BaTiO}_3$ . Shown in Figure 5 is a representative spectrum. The five strong resonant absorptions are typical of the  $\text{Fe}^{3+}$  ion in a tetragonal crystalline electric field. Weaker isotropic transitions (i.e., angle independent) of unknown origin are observed at magnetic fields below  $\sim 1160$  G and in the range  $\sim 3334$ – $90$  G. From the measured spectra it is apparent that  $\text{Fe}^{3+}$  is the dominant paramagnetic center in each sample. Absolute  $\text{Fe}^{3+}$  concentration measurements have been made by comparing the intensity of the  $\text{Fe}^{3+}$  ( $-1/2 \rightarrow 1/2$ ) transition with the resonant absorption from a calibrated sample of  $\text{Cr}^{3+}$  (in  $\text{MgO}$ ) placed in the microwave cavity along with the crystal of  $\text{BaTiO}_3$ . The results of these measurements for single crystals R2 and G/L are given in Table II.

### Discussion

As indicated earlier, the defects in  $\text{BaTiO}_3$  which could lead to levels responsible for the photorefractive effect are impurities and vacancies. From the results of earlier work<sup>6,10</sup> and our own measurements, the dominant impurities are transition metals, most notably iron. For crystals grown in air, the only vacancies present in appreciable quantities are oxygen vacancies<sup>6,10</sup>. However, these vacancies are known to act as donors (f-centers), and thus can not explain the observation that the photocarriers (in most crystals) are holes.

While several transition metal impurities are present in our samples in sufficient quantities to result in photorefractive behavior, we believe that the large concentrations of iron in our samples (and its importance in  $\text{LiNbO}_3$ ) favors this species as that responsible for the photorefractive effect. Since hole photoconductivity dominates in most of our samples, the filled traps would correspond to  $\text{Fe}^{3+}$  and the empty traps would correspond to  $\text{Fe}^{2+}$ . This is also consistent with the observation [14] that the majority of the Fe ions in as-grown iron-doped  $\text{BaTiO}_3$  and  $\text{LiNbO}_3$  are in the  $\text{Fe}^{3+}$  state. Assuming a total iron concentration of  $5 \times 10^{18} \text{ cm}^{-3}$  ( $100 \text{ ppm}$ ) in our samples, and a typical  $\text{Fe}^{2+}$  concentration (from beam coupling) of  $\sim 5 \times 10^{16} \text{ cm}^{-3}$ , we find  $[\text{Fe}^{2+}]/[\text{Fe}^{3+}] \approx 100$ . If, instead, we use the EPR data for  $[\text{Fe}^{2+}]$ , we find  $[\text{Fe}^{2+}]/[\text{Fe}^{3+}] \approx 40$ .

The identification of Fe as the photorefractive species in  $\text{BaTiO}_3$  is only applicable to our samples, and must be considered as tentative until further calculations and measurements are performed. One key experiment would be to subject a given sample to heat treatments in both oxidizing and reducing atmospheres, and correlate the changes in the EPR signals and absorption coefficient with changes in the photorefractive behavior.

### Acknowledgements

I would like to acknowledge helpful discussions with D. Rytz, B. Wechsler, G.C. Valley, R.C. Pastor, and R.N. Schwartz, and technical assistance by R.H. Sipman. The EPR measurements were performed by R.N. Schwartz. This work was supported by DARPA and monitored by RADC (Solid State Sciences Div., Hanscom AFB, MA) through Contract #F19628-84C-0069.

### References

1. J. Feinberg and R.W. Hellwarth, *Opt. Lett.* **5**, 519 (1980).
2. R.K. Jain and G.J. Dunning, *Opt. Lett.* **7**, 420 (1982).
3. J.O. White, M. Cronin-Golomb, B. Fischer and A. Yariv, *Appl. Phys. Lett.* **40**, 450 (1982).
4. G.C. Valley and H.B. Klein, *Opt. Eng.* **22**, 704 (1983).
5. R. Orlowski and E. Kratzig, *Solid St. Comm.* **27**, 1351 (1978).
6. A.M.J.H. Seuter, *Philips Res. Rpts. Suppl.* **No. 3** (1974).
7. J. Daniels, *Philips Res. Rpts.* **31**, 505 (1976).
8. N.G. Eror and D.M. Smyth, *J. Solid St. Chem.* **24**, 235 (1978).
9. N.H. Chan, R.K. Sharma and D.M. Smyth, *J. Am. Ceram. Soc.* **64**, 556 (1981).
10. N.H. Chan, R.K. Sharma and D.M. Smyth, *J. Am. Ceram. Soc.* **65**, 167 (1982).
11. N.V. Kukhtarev, V.B. Markov, S.G. Odulov, M.S. Soskin, and V.L. Vinetskii, *Ferroelectrics* **22**, 949 and 961 (1979).
12. J. Feinberg, D. Heiman, A.R. Tanguay, Jr, and R.W. Hellwarth, *J. Appl. Phys.* **51**, 1297 (1980).
13. A. Marrakchi, J.P. Huignard and P. Gunter, *Appl. Phys.* **24**, 131 (1981).
14. M.G. Clark, F.J. DiSalvo, A.M. Glass and G.E. Peterson, *J. Chem Phys* **59**, 6209 (1973).
15. E. Siegel and K.A. Muller, *Phys. Rev B* **20**, 3587 (1979).
16. H.J. Hagemann, A. Hero and U. Gonser, *Phys. Stat. Sol.* **A61**, 63 (1980).
17. A.W. Hornig, R.C. Rempel and H.E. Weaver, *J. Phys. Chem. Solids* **10**, 1 (1959).

Table I. Results of Beam Coupling and Optical Absorption Measurements

CRYSTAL	SIGN OF DOMINANT PHOTOCARRIER	NUMBER OF EMPTY TRAPS $N_E$ ( $\text{cm}^{-3}$ )	ABSORPTION COEFFICIENT AT 5145 Å FOR $E_C$ ( $\text{cm}^{-1}$ )
GIL	-	$4.4 \times 10^{16}$	0.8
R1	-	8.1	2.1
R2	-	2.8	0.2
GB3	-	6.1	1.5
K2	-	8.7	1.4
SC	-	4.2	
GB4	-	2.0	0.3

Table II. Concentration Measurements in  $\text{BaTiO}_3$

SAMPLE	SPECIES	TOTAL CONCENTRATION (EMISSION SPECTROSCOPY)	NUMBER OF EMPTY TRAPS (FROM BEAM COUPLING)	RELATIVE NUMBER OF FILLED TRAPS (FROM ABSORPTION AT 5145 Å)	$F_2^{2+}$ CONCENTRATION (FROM EPR)
R2	$F_2$	17 PPM	$3.1 \times 10^{16} \text{ cm}^{-3}$	0.2	$1.2 \times 10^{18} \text{ cm}^{-3}$
	$Mn$	<50 PPM			
GIL	$F_2$	120 PPM	$4.4 \times 10^{16} \text{ cm}^{-3}$	0.8	$2.0 \times 10^{18} \text{ cm}^{-3}$
	$Mn$	<50 PPM			
	$Ni$	<20 PPM			

100 PPM =  $5 \times 10^{18} \text{ cm}^{-3}$

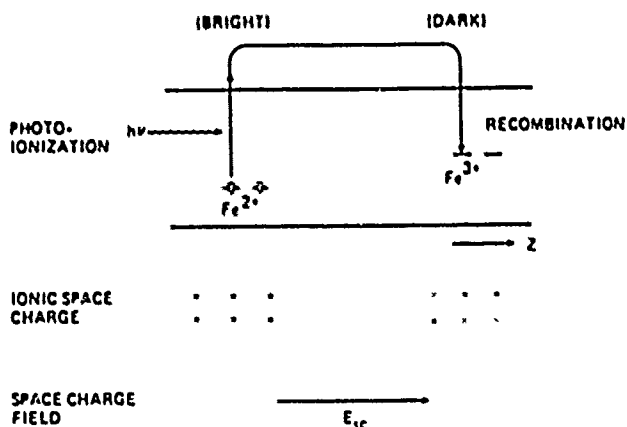


Figure 1. Schematic of the band transport model of photorefractivity, using  $\text{LiNbO}_3:\text{Fe}$  as an example

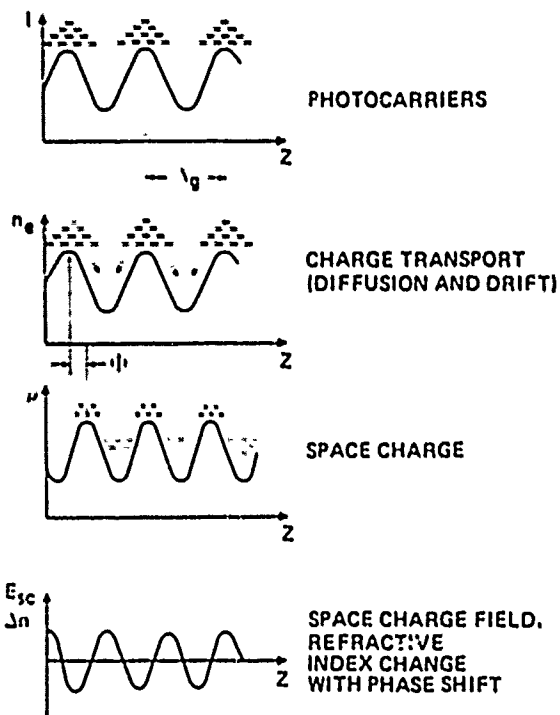


Figure 2. Gratings in a photorefractive material, assuming a periodic irradiance pattern

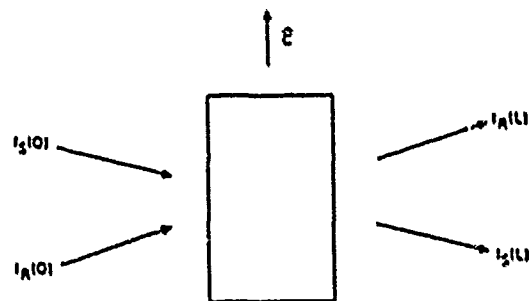


Figure 3. Crystal orientation and beam notation for beam coupling experiments.  $I_s$  is the signal wave, and  $I_R$  is the reference wave

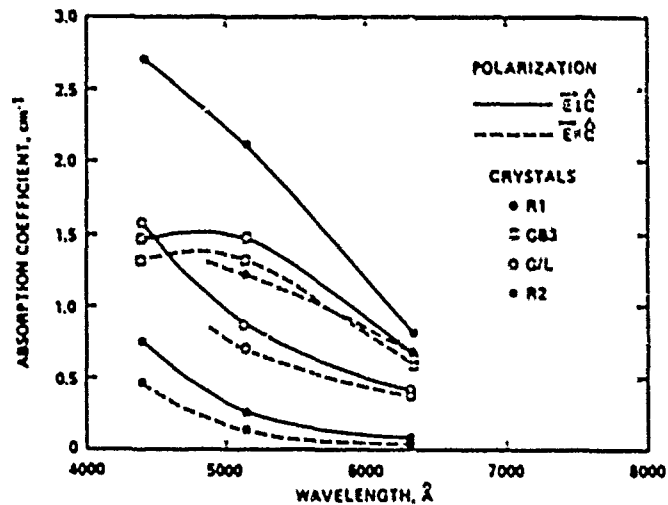


Figure 4. Optical absorption in  $\text{BaTiO}_3$

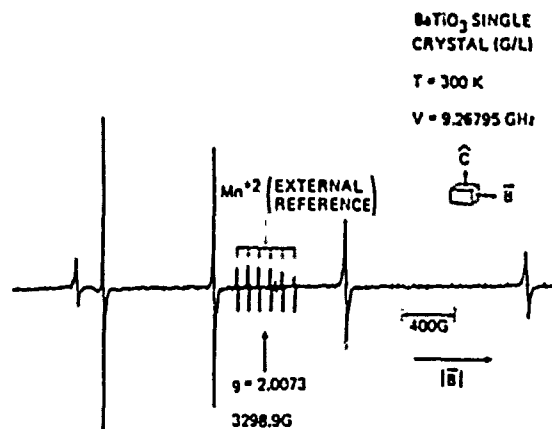


Figure 5. EPR spectrum of single crystal  $\text{BaTiO}_3$



# Beam coupling in BaTiO<sub>3</sub> at 442 nm

M. B. Klein and George C. Valley

## APPENDIX 2

Hughes Research Laboratories, 3011 Malibu Canyon Road, Malibu, California 90265

(Received 27 December 1984; accepted for publication 15 February 1985)

Steady-state beam coupling is used to measure the concentration of empty traps, the sign of the dominant photocarrier, and the effective electro-optic coefficient in seven crystals of BaTiO<sub>3</sub>. The measured value of the effective electro-optic coefficient gives the product of the fractional poling of the crystal, the relative conductivity of the crystal, and the electro-optic coefficient. Anomalous low beam coupling gain measured in an eighth crystal suggests that this crystal is nearly perfectly compensated; i.e., the photoconductivities due to electrons and holes are nearly equal.

Photorefractive materials have great promise in applications such as optical data processing and phase conjugation. Among candidate photorefractive materials, BaTiO<sub>3</sub> is particularly attractive because it has a large  $r_{33}$  component of the electro-optic tensor that leads to large values of the coupling coefficient for two- and four-wave mixing.<sup>1,2</sup> This allows the realization of self-pumped phase conjugate mirrors<sup>3</sup> and phase conjugate resonators.<sup>1,4</sup>

While the applications of BaTiO<sub>3</sub> have been under study for some time, relatively little is known regarding the species responsible for the photorefractive effect in this material. In the basic band transport model, a single species with two valence states corresponding to separate energy levels in the BaTiO<sub>3</sub> band gap is required. In order to predict performance of devices using BaTiO<sub>3</sub> it is necessary to know the number densities and rate coefficients for these states as well as the transport properties of the free carriers in the crystal. In addition, since BaTiO<sub>3</sub> is usually incompletely poled, it is necessary to know the degree of poling of a sample.

In this paper, we use steady-state beam coupling experiments on seven BaTiO<sub>3</sub> crystals obtained from a commercial supplier<sup>5</sup> to obtain data on the number density of the empty traps, the effective electro-optic coefficient, and the sign of the dominant photocarrier. In a separate publication, we will report the results of nonphotorefractive measurements that further add to our understanding of the photorefractive species in BaTiO<sub>3</sub>. Preliminary results on our beam coupling studies and nonphotorefractive measurements have recently been presented.<sup>11</sup>

In the beam coupling technique, two beams incident on the sample produce a spatially periodic irradiance pattern. If the resultant refractive index grating is not in phase with the irradiance grating, then energy is transferred from one beam to the other, in a direction determined by the crystal orientation and the carrier with the greater photoconductivity, but not by the relative power in the beams.

For the specific case of BaTiO<sub>3</sub>, we consider the crystal orientation and beam notation shown in Fig. 1. We assume that the crystal *c* axis is oriented so that the signal beam *I<sub>s</sub>* is amplified at the expense of *I<sub>r</sub>*. The transmission of the signal beam is then given by<sup>6</sup>

$$\frac{I_s(L)}{I_s(0)} = \frac{[I_s(0) + I_r(0)] \exp[(\Gamma - \alpha)L]}{I_r(0) + I_s(0) \exp(\Gamma L)} \quad (1)$$

where  $\Gamma$  is the gain coefficient,  $\alpha$  is the absorption coefficient, and *L* is the interaction length. For negligible depletion of the reference wave [ $I_s(0) \exp(\Gamma L) < I_r(0)$ ], Eq. (1) reduces to

$$I_s(L) = I_s(0) \exp[(\Gamma - \alpha)L]. \quad (2)$$

In our experiment we measure the effective gain  $\gamma_0$ ,<sup>6</sup> defined as

$$\gamma_0 = \frac{I_s(L) \text{ with reference beam}}{I_s(L) \text{ without reference beam}}. \quad (3)$$

When depletion of the reference wave can be neglected,  $\gamma_0 = \exp(\Gamma L)$ .

In the most general case, the periodic space-charge electric field is shifted in phase from that of the irradiance by a value between 0 and  $\pi/2$ .<sup>8,9</sup> The gain  $\Gamma$  is then given by<sup>7</sup>

$$\Gamma = \frac{2\pi n^3}{\lambda \cos \theta} r_{\text{eff}} F \text{Im}(E_{\text{sc}}), \quad (4)$$

where *n* is the refractive index,  $r_{\text{eff}}$  is the appropriate combination of components of the electro-optic tensor and of the angular and polarization factors for a fully poled crystal, *F* is the fractional poling,  $E_{\text{sc}}$  is the amplitude of the space-charge electric field, and  $\theta$  is the Bragg angle inside the crystal.

The energy level model and notation we use for BaTiO<sub>3</sub> are shown in Fig. 2. We assume that a single species *X*, which can exist in two valence states (*X* and *X*<sup>+</sup>), is responsible for the energy states in the BaTiO<sub>3</sub> band gap. In the case of iron-doped LiNbO<sub>3</sub>, *X* corresponds to Fe<sup>3+</sup> and *X*<sup>+</sup> corresponds to Fe<sup>3+</sup>, but the identification is currently unknown in

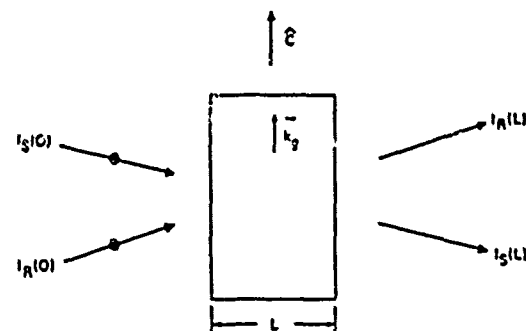


FIG. 1. Crystal orientation and beam notation for the beam coupling measurements. Both incident beams are *s* polarized, perpendicular to the plane of the paper.

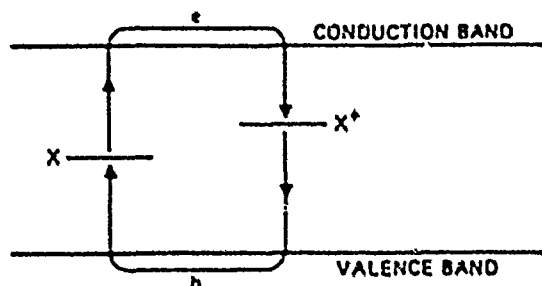


FIG. 2. Energy level model assumed for interpreting the beam coupling measurements. Electrons are photoionized from level  $X$  and recombine at  $X^+$ ; holes are photoionized from  $X^-$  and recombine at  $X^-$ .

BaTiO<sub>3</sub>. We designate the concentration of  $X$  as  $N$ , and the concentration of  $X^-$  as  $N^-$ . Other states, which are assumed to be optically inactive, provide overall charge compensation within the crystal. We note also that electrons or holes (or both) can contribute to the charge transport in our crystals, as shown in Fig. 2. For electron transport, state  $X$  is a donor, or "filled" state, and state  $X^+$  is an ionized donor, or "empty" state. For hole transport, state  $X^-$  is an acceptor or "filled" state, and state  $X^-$  is an ionized acceptor, or "empty" state. We further note that the sign of the space-charge field is opposite for the two carriers. This changes the direction of beam coupling, and allows a measurement of the dominant photocarrier.

In many cases of interest, a number of approximations can be made which lead to simplified expressions for the space-charge electric field. In our experiments, we first assume that the dark conductivity is negligible compared to the photoconductivity. We will show later that this is a safe assumption for irradiance values exceeding  $\sim 10 \mu\text{W}/\text{cm}^2$ . We also assume that the bulk photovoltaic effect is negligible in our samples and note that no applied field is used in our experiments. For these conditions, the space-charge field is purely imaginary (shifted in phase by  $\pi/2$ ), and is given by (see the Appendix)

$$E_{sc} = \left( \frac{\mu_h p - \mu_e n}{\mu_h p + \mu_e n} \right) \frac{E_d E_q}{E_d + E_q}. \quad (5)$$

In Eq. (5),  $\mu_h$  and  $\mu_e$  are the hole and electron mobilities,  $p$  and  $n$  are the hole and electron concentrations,  $E_d$  is the diffusion electric field, and  $E_q$  is the limiting space-charge electric field. The diffusion field is given by

$$E_d = \frac{k_B T 2\pi}{e \Lambda_g}, \quad (6)$$

where  $\Lambda_g$  is the grating period. The limiting space-charge electric field is given by

$$E_q = \frac{2e\Lambda_g}{\epsilon} \frac{N_+ N_-}{N_+ + N_-}, \quad (7)$$

where  $\epsilon$  is the dielectric constant.

The first factor in Eq. (5) accounts for the relative contribution of electrons and holes to the photoconductivity in the sample. Since this factor appears in the gain coefficient as a multiplicative factor with no dependence on grating period or irradiance, it can be included as a part of an effective electro-optic coefficient, defined as

$$r_{eff} = r_{33} F \bar{\sigma}, \quad (8)$$

where  $\bar{\sigma}$  is the normalized conductivity given by the first factor of Eq. (5). Note that the sign of  $\bar{\sigma}$  is not determined by the relative concentration of electrons and holes, but by the relative values of their photoconductivities. Furthermore, as indicated earlier, the sign of  $\bar{\sigma}$  determines the sign of the space-charge electric field, and thus the direction of beam coupling.

If we substitute Eqs. (6) and (7) into Eqs. (4) and (5), we obtain

$$\Gamma = \frac{2\pi n^3}{\lambda \cos \theta} r_{eff} \frac{E_{d0} E_{q0}}{E_{d0}/\Lambda_g + E_{q0}/\Lambda_g}, \quad (9)$$

where  $E_{d0} = E_d/\Lambda_g$ , and  $E_{q0} = E_q/\Lambda_g$ . Thus, if  $r_{eff}$  is independent of  $\theta$  and  $\Lambda_g$  is large enough so that  $\cos \theta \approx 1$  (the error in setting  $\cos \theta = 1$  is less than 1.5% for  $\Lambda_g > 0.5 \mu\text{m}$ ), then a plot of  $\Gamma$  vs  $\Lambda_g$  will increase linearly for small  $\Lambda_g$ , reach a maximum when  $\Lambda_{g0} = (E_{d0}/E_{q0})^{1/2}$ , and decrease as  $\Lambda_g^{-1}$  for large  $\Lambda_g$ . In Eq. (9) there are two material parameters that can be measured in a beam coupling experiment provided that  $n$  and  $\epsilon$  are known:  $r_{eff}$  and  $NN^+/(N_+ + N_-)$ . The most direct means of doing this would be to fit data to the function given by Eq. (9) with  $r_{eff}$  and  $NN^+/(N_+ + N_-)$  as variables. Alternatively, one could note that  $1/\Gamma\Lambda_g$  as a function of  $1/\Lambda_g^2$  is a straight line with slope  $2\pi n^3 r_{eff} E_{q0}/\lambda$  and intercept  $2\pi n^3 r_{eff} E_{d0}/\lambda$  and perform the fits using this function.

In our beam coupling experiments we have studied seven BaTiO<sub>3</sub> crystals obtained from Sanders Associates.<sup>9</sup> In each case the crystal as received was free of 90° domains. The 180° domains were removed by heating the crystals in oil to 129 °C, applying 2–4 kV/cm and cooling slowly to room temperature. It is difficult to determine if all 180° domains are removed by this procedure. If some domains remain (and if they are uniformly distributed through the crystal), the net effect in our experiments is to reduce the electro-optic coefficients below their value for a perfectly poled crystal. As mentioned earlier, we have accounted for this reduction by introducing a fractional poling factor  $F$  ( $F < 1$ ) which multiplies the electro-optic coefficients as given in the literature.

The laser source for our experiments was a cw He-Cd laser operating in the fundamental transverse mode and having a coherence length of  $\sim 5$  cm. The output beam from the laser was divided at a beam splitter, and the two resulting beams were recombined at the sample in such a way that the input angle could be varied while the path lengths of the two beams were kept equal. In all our experiments, the grating normal was aligned parallel with the  $c$  axis, as shown in Fig. 1. Both input beams were  $s$  polarized (along a crystalline  $a$  axis) to exploit the refractive index change induced through the electro-optic tensor component  $r_{13}$  ( $r_{33} = r_{13}$ ). We deliberately chose an orientation sensitive only to the small  $r_{13}$  component, in order to avoid complications due to beam fanning in BaTiO<sub>3</sub>.<sup>10</sup> The signal beam had a power of  $\sim 10 \mu\text{W}$  and a diameter of  $\sim 2$  mm. The reference beam was expanded with a telescope to a diameter of  $\sim 5$  mm in order to maintain a uniform interaction region over the length of the crystal as the input angle was varied. The power in this beam was made sufficiently large ( $\sim 5$  mW) to insure that it

TABLE I. Sign of the dominant photocarrier, effective trap density, effective electro-optic coefficient, and fractional poling  $F$  times the relative conductivity factor  $\bar{\sigma} = (\sigma_e - \sigma_h)/(\sigma_e + \sigma_h)$  for seven crystals of photorefractive BaTiO<sub>3</sub>.

Crystal	Sign of dominant photocarrier	$\frac{NN^+}{N+N^+}$ (cm <sup>-3</sup> )	Effective E-O coefficient $r_{eff}$ (pm/V)	$F\bar{\sigma} \approx r_{eff}/r_{13}$
G/L	+	$4.4 \times 10^{18}$	7.3	0.30
R1	+	8.1	9.5	0.40
R2	-	2.8	-7.9	-0.33
GB3	+	6.1	9.7	0.41
K2	+	8.7	12.0	0.50
SC	+	4.2	8.3	0.35
GB4	+	3.0	4.2	0.18

would remain undepleted in our experiments. At the resulting level of irradiance ( $\sim 20$  mW/cm<sup>2</sup>), the photoconductivity is approximately three orders of magnitude larger than the dark conductivity, as measured in two of our crystals.

In each of the seven crystals studied, the  $c$ -axis direction was set so that the signal beam (see Fig. 1) was amplified at the expense of the reference beam. Using the convention developed by Feinberg *et al.*,<sup>2</sup> we were then able to determine the sign of the dominant photocarrier. The results of this measurement are given in Table I. We note that holes dominate the photoconductivity in six of the seven measured crystals. This result is not surprising, since crystals grown in air or an oxidizing atmosphere are known to favor the higher valence states of impurities or defects ( $X^+$  in our model).<sup>12</sup>

Plots of the beam coupling data  $[(\Gamma/\Lambda)^{-1} \text{ vs } \Lambda^{-2}]$  for our crystals are shown in Fig. 3; the solid lines represent best fits of a straight line to the data, using  $r_{eff}$  and  $NN^+/(N+N^+)$  as variables. The quality of the fit shown for K2 is typical for all seven crystal and justifies neglect of dark conductivity and the bulk photovoltaic effect in our modelling.

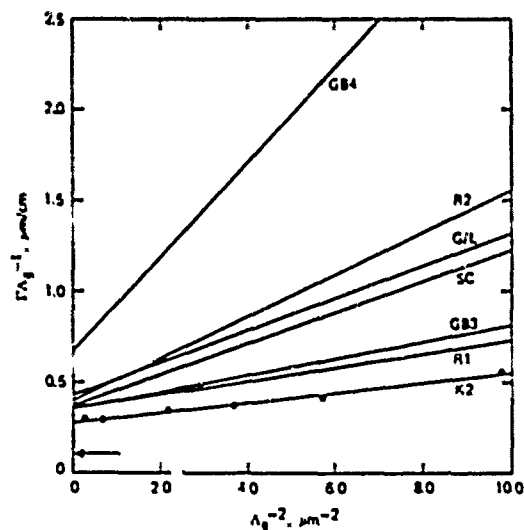


FIG. 3. Inverse of the two-wave mixing gain coefficient  $\Gamma$  times grating period  $\Lambda$ , as a function of  $1/\Lambda^2$  for seven crystals of photorefractive BaTiO<sub>3</sub>. The quality of the fits is equivalent to that shown for crystal K2. The arrow indicates the intercept for a perfectly poled crystal in which either electron or hole conductivity is completely dominant.

We see that the plots are a useful "signature" of a crystal, allowing unambiguous identification if such a need arises. The measured values of  $r_{eff}$  and  $NN^+/(N+N^+)$  for each of our crystals are given in Table I. We have assumed here that  $\epsilon = 168$  and  $n = 2.4$ .<sup>13</sup> We also plot the product  $\bar{\sigma}F = r_{eff}/r_{13}$  in Table I, using the unclamped value of  $r_{13}$  ( $r_{13} = 24$  pm/V).<sup>13</sup> The selection of the unclamped value of  $r_{13}$  is justified by the observation that the use of the smaller, clamped value of  $r_{13}$  would lead to the nonphysical result  $\bar{\sigma}F > 1$  in all but two crystals. Note that this experiment does not allow a separate determination of the fractional poling  $F$  and the normalized conductivity  $\bar{\sigma}$ , although we believe that the greater contribution comes from the normalized conductivity.

For each of the crystals in which hole conductivity dominates, we may write  $\sigma_h > \sigma_e$ , or  $\mu_h p > \mu_e n$ . If we assume that the photoionization cross sections and recombination coefficients are comparable for levels  $X$  and  $X^+$ , then the above condition can be written as  $N/N^+ < (\mu_h/\mu_e)^{1/2}$ . Measurements and estimates of  $\mu_h$  and  $\mu_e$  in BaTiO<sub>3</sub> differ widely, but many measurements suggest that  $\mu_h < \mu_e$  at room temperature.<sup>14-17</sup> We thus obtain  $N < N^+$ , so that  $NN^+/(N+N^+) \approx N$ , the number of empty acceptor states. If the species with densities  $N$  and  $N^+$  are identified as  $Fe^{2+}$  and  $Fe^{3+}$ ,<sup>11</sup> then  $N < N^+$  is consistent with observations that  $[Fe^{2+}] < [Fe^{3+}]$  in our crystals<sup>11</sup> and other observations in BaTiO<sub>3</sub>.<sup>12</sup> Even in the crystal with electron photoconductivity, it is likely that  $\sigma_e$  is not much larger than  $\sigma_h$ , so that the above approximation will still apply. Thus for all of the measured crystals the measured parameter  $NN^+/(N+N^+)$  corresponds closely to  $N$ , the concentration of donor states in the crystal. The measured values of  $N$  reported here are consistent with other values in the literature.<sup>2,18</sup>

During the course of our beam coupling measurements one sample behaved in a very different manner from the crystals described above. A plot of gain versus grating period for this crystal (GB5) is given in Fig. 4. Note that the beams were  $p$  polarized in this experiment, to exploit the larger  $r_{33}$  coefficient. Even so, the measured values of gain are at least a factor of 10 smaller than those expected for this orientation. In addition, the gain changes sign with grating period. A measurement of the electro-optic coefficient for this crystal

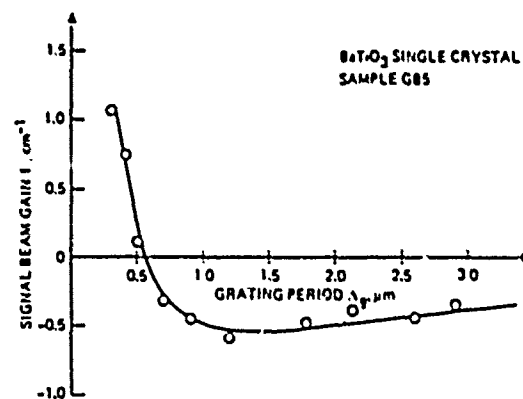


FIG. 4. Two-wave mixing as a function of grating period for the anomalous crystal GB5.

through the measurement of amplitude modulation indicated that the coefficient was comparable in value to those measured in the other crystals, suggesting that this crystal was as well poled as all the others. Our explanation for the gain behavior given in Fig. 4 is that the photoconductivity is nearly perfectly compensated in this crystal (i.e.,  $\sigma_e \approx \sigma_h$ ), leading to the appearance of a weaker effect of unknown origin.

In summary, we have used steady-state two-wave mixing as a diagnostic technique to measure two lumped parameters in seven crystals of photorefractive BaTiO<sub>3</sub>. One parameter can be interpreted as the empty trap density and ranges from 2.3 to  $5.7 \times 10^{18} \text{ cm}^{-3}$ ; the other is the effective electro-optic coefficient which ranges from 0.18 to 0.50 times the tabulated unclamped value of the electro-optic coefficient and includes a sign that indicates the sign of the dominant photocarrier. Since the clamped coefficient is 1/3 the unclamped value, this is clear evidence that the appropriate electro-optic coefficient for photorefractive studies is the unclamped value. The reason that the full unclamped value is not obtained is interpreted in terms of incomplete poling of the sample and simultaneous electron and hole transport. Further work reporting on identification of the photorefractive species in these crystals is in preparation.

#### ACKNOWLEDGMENTS

This work was supported in part by DARPA and monitored by the Solid State Sciences Division of the Rome Air Development Center, Hanscom AFB, MA under Contract F19628-84C-0069. We would like to thank R. H. Sipman for expert technical assistance.

#### APPENDIX

Consider the donors and traps as shown on the schematic energy level diagrams in Fig. 2. The levels  $N$  (nominal donors for electrons) are described by the rate equation

$$\frac{\partial N}{\partial t} = -s_e I N + \gamma_e n_e N^+, \quad (\text{A1})$$

where  $s_e$  is the photo-cross section for ionization of  $N$ ,  $I$  is the irradiance,  $\gamma_e$  is the recombination coefficient for electrons at sites  $N^+$ ,  $n_e$  is the electron number density, and  $N^+$  is the number density of  $X^+$  which act as electron traps. We further assume that holes can be photoionized from  $N^+$  as described by

$$\frac{\partial N^+}{\partial t} = -s_h I N^+ + \gamma_h n_h N, \quad (\text{A2})$$

where  $s_h$  is the photo-cross section for generating a free hole,  $\gamma_h$  is the hole recombination coefficient, and  $n_h$  is the hole number density.

A complete set of equations is obtained from Poisson's equation, continuity, a current equation, and the assumption that the sum of the number densities of  $X$  and  $X^+$  is constant<sup>20</sup>:

$$\nabla E = -\frac{4\pi e}{\epsilon} (n_e + N_A - N^+ - n_h), \quad (\text{A3})$$

$$\frac{\partial}{\partial t} (n_e - N^+ - n_h) = +\frac{1}{e} \nabla j, \quad (\text{A4})$$

$$j = + (e\mu_e n_e + e\mu_h n_h) E - k_B T \left( \mu_h \frac{\partial n_h}{\partial z} - \mu_e \frac{\partial n_e}{\partial z} \right), \quad (\text{A5})$$

$$N + N^+ = N_T \quad (\text{A6})$$

where  $E$  is the electric field;  $\epsilon$  is the static dielectric constant;  $N_A$  is the number density of negatively charged, nonphotoactive ions that compensate for the charge of  $N^+$  in the dark;  $j$  is the current density;  $\mu_e$  and  $\mu_h$  are the electron and hole mobilities (both  $> 0$ ); and  $N_T$  is the total number density of species  $X$ .

The gain coefficient for steady-state two-wave mixing can be obtained as usual by setting all of the unknowns  $Y$  equal to their mean value plus a sinusoidal grating term

$$Y = Y_0 + Y_1 e^{ikz}.$$

The mean equation can be solved to give

$$N_0^+ = N_A + n_{e0} - n_{h0} \sim N_A, \quad (\text{A7})$$

$$n_{e0} \approx \frac{s_e I_0 (N_T - N_A)}{\gamma_e N_A}, \quad (\text{A8})$$

$$n_{h0} \approx \frac{s_h I_0 N_A}{\gamma_h (N_T - N_A)}, \quad (\text{A9})$$

where the last two equations are approximations valid for  $n_e$  and  $n_h < N_A$  and  $N_T - N_A$ .

The steady-state equations for the first-order Bragg terms with no applied field can be written down by inspection of Eqs. (1)-(6) with  $I = I_0 [1 + m \exp(ikz)]$ .

$$ik_e E = -\frac{4\pi e}{\epsilon} (n_e - N^+ - n_h), \quad (\text{A10})$$

$$+ (e\mu_e n_{e0} + e\mu_h n_{h0}) E - ik_e k_B T (\mu_h n_h - \mu_e n_e) = 0, \quad (\text{A11})$$

$$s_e I_0 N^+ - s_e m I_0 (N_T - N_0^+) + \gamma_e n_{e0} N^+ + \gamma_e n_e N_0^+ = 0, \quad (\text{A12})$$

$$-s_h I_0 N^+ - s_h m I_0 N_0^+ + \gamma_h n_{h0} N^+ + \gamma_h n_h (N_T - N_0^+) = 0, \quad (\text{A13})$$

where  $j = 0$  in the steady state and the subscript sub 1 has been dropped from  $E$ ,  $n_e$ ,  $n_h$ , and  $N^+$ .

Equations (A10)-(A13) can be solved by substitution; the resulting formula for  $E$  is slightly messy. If one makes the further approximation, which should usually be applicable for cw laser intensities,

$$n_{e0} < \frac{N_A (N_T - N_A)}{N_T},$$

$$n_{h0} < \frac{N_A (N_T - N_A)}{N_T},$$

then the space-charge field simplifies to

$$E = \frac{iE_d m (\mu_h n_{h0} - \mu_e n_{e0})}{(1 + E_d/E_e) (\mu_h n_{h0} + \mu_e n_{e0})} \equiv i m E_{sc}, \quad (\text{A14})$$

where

$$E_d \equiv k_e k_B T / e$$

and

$$E_e \equiv \frac{4\pi e N_A (N_T - N_A)}{\epsilon k_e N_T} = \frac{4\pi e N_0^+ N_0}{\epsilon k_e (N_0 + N_0^+)}.$$

Note the change in sign of  $E$  when  $\mu_h n_{h0}$  is greater than  $\mu_e n_{e0}$ . This means that the direction of energy transfer in two-wave mixing is determined by the difference between

the mean electron and hole conductivities. Note also that there is no sign change with grating period. This conclusion is unaffected by the small terms omitted in deriving Eq. (A14). Finally note that  $E_g$  is given by the same expression for transport dominated by either electrons or holes.

- <sup>1</sup>J. Feinberg and R. W. Hellwarth, *Opt. Lett.* **5**, 519 (1981).
- <sup>2</sup>J. Feinberg, D. Heiman, A. R. Tanguay, Jr., and R. W. Hellwarth, *J. Appl. Phys.* **52**, 1297 (1980).
- <sup>3</sup>J. White, M. Cronin-Golomb, B. Fischer, and A. Yariv, *Appl. Phys. Lett.* **40**, 450 (1982); J. Feinberg, *Opt. Lett.* **7**, 486 (1982).
- <sup>4</sup>R. A. McFarlane and D. G. Steel, *Opt. Lett.* **8**, 208 (1983).
- <sup>5</sup>Sanders Associates, Nashua, NH 03061.
- <sup>6</sup>J. P. Huignard and A. Marrakchi, *Opt. Commun.* **38**, 249 (1981).
- <sup>7</sup>A. Marrakchi, J. P. Huignard, and F. Günter, *Appl. Phys.* **24**, 131 (1981).
- <sup>8</sup>N. V. Kukhtarev, V. D. Markov, S. G. Odulov, M. S. Soskin, and V. L.

- Vinetskii, *Ferroelectrics* **22**, 949 (1979).
- <sup>9</sup>N. V. Kukhtarev, *Sov. Tech. Phys. Lett.* **2**, 438 (1976).
- <sup>10</sup>J. Feinberg, *J. Opt. Soc. Am.* **72**, 46 (1982).
- <sup>11</sup>M. B. Klein, Proceedings of the SPIE Conference on Analog Optical Processing and Computing, Cambridge, MA, Paper 519-22 (25-26 October 1984).
- <sup>12</sup>H. J. Hagemann, A. Herz, and U. Gonser, *Phys. Status Solidi A* **61**, 63 (1980).
- <sup>13</sup>F. Günter, *Phys. Rep.* **93**, 200 (1983).
- <sup>14</sup>G. A. Cox and R. H. Tredgold, *Phys. Lett. (Netherlands)* **11**, 22 (1964).
- <sup>15</sup>K. Kawabe and Y. Inuishi, *Jpn. J. Appl. Phys.* **2**, 590 (1963).
- <sup>16</sup>P. Gerthsen, K. H. Hårdt, and A. Cullag, *Phys. Status Solidi A* **13**, 127 (1972).
- <sup>17</sup>N. H. Chan, R. K. Sharma, and D. M. Smyth, *J. Am. Ceram. Soc.* **64**, 556 (1981).
- <sup>18</sup>S. Ducharme and J. Feinberg, *J. Appl. Phys.* **56**, 539 (1984).
- <sup>19</sup>A. Rose, *Concepts in Photoconductivity and Allied Problems* (Krieger, Huntington, NY, 1978), pp. 13-18.
- <sup>20</sup>G. Valley and M. B. Klein, *Opt. Eng.* **22**, 704 (1983).